NANYANG
TECHNOLOGICAL
UNIVERSITY
SINGAPORE

LASER MICROPROCESSING OF SAPPHIRE   CELESCIA LYE SIEW MUN   2020

LASER MICROPROCESSING OF SAPPHIRE

CELESCIA LYE SIEW MUN

SCHOOL OF MECHANICAL AND AEROSPACE ENGINEERING

2020

LASER MICROPROCESSING OF SAPPHIRE

CELESCIA LYE SIEW MUN

SCHOOL OF MECHANICAL AND AEROSPACE ENGINEERING

A thesis submitted to the Nanyang Technological University in partial fulfillment of the requirement for the degree of Master of Engineering

2020

Statement of Originality

I hereby certify that the work embodied in this thesis is the result of original research, is free of plagiarised materials, and has not been submitted for a higher degree to any other University or Institution.

7 July 2020

. . . .

Date

. . . .

Celescia Lye Siew Mun

Supervisor Declaration Statement

I have reviewed the content and presentation style of this thesis and declare it is free of plagiarism and of sufficient grammatical clarity to be examined. To the best of my knowledge, the research and writing are those of the candidate except as acknowledged in the Author Attribution Statement. I confirm that the investigations were conducted in accord with the ethics policies and integrity standards of Nanyang Technological University and that the research data are presented honestly and without prejudice.

7 July 2020

Lamyc

. . . .

Date

. . . .

Prof. Lam Yee Cheong

Authorship Attribution Statement

Please select one of the following; *delete as appropriate:

*(A) This thesis **does not** contain any materials from papers published in peer-reviewed journals or from papers accepted at conferences in which I am listed as an author.

~~*(B) This thesis contains material from [x number] paper(s) published in the following peer-reviewed journal(s) / from papers accepted at conferences in which I am listed as an author.~~

7 July 2020

. . . .

Date

. . . .

Celescia Lye Siew Mun

Abstract

Sapphire is a substrate in many applications; for example, in watch covers, phone displays, integrated circuits, optoelectronics and light emitting diodes (LEDs). To be useful for these applications, sapphire boules have to be separated into wafers and chips for further processing. This thesis investigates an important processing step of sapphire, namely the laser singulation of sapphire.

Previous studies showed that the surface morphology of patterned sapphire substrates (PSS) enhanced the light emission of LEDs. However, the effects of surface morphology on the optical properties of sapphire during laser scanning have not been properly studied.

This thesis examined the interaction between the laser beam and sapphire of different surface roughness. Experiments conducted confirmed the proposed hypothesis in this investigation that a sample with a single rough surface exhibited higher levels of absorbance compared to a sample with two polished surfaces. This is predominantly a result of internal reflection at the exit surface. As such, internal reflection can be enhanced by orientating the sample such that the rough surface was facing away from the laser beam source. The presence of the rough surface encourages nonlinear absorption within the sample at lower incoming laser intensities. Significantly more nonlinear absorption could be observed in the sample with its rough surface facing away from the laser, i.e. with a bottom rough surface. As a result, ablation scribes were observed on both top and bottom surfaces of a sample after picosecond laser irradiation at 1.7 W with a focused spot diameter of 27.1 μm on the top surface of the sample. Therefore, the presence of the bottom rough surface improves the nonlinear interaction between the laser beam and the sample.

Previous studies on multiple foci laser cutting of a transparent material have been focused on transparent glass cutting. The foci spots were spread over the glass thickness employing highly specialized focusing optics. However, the investigation of the same for sapphire has been lacking. This is worth investigating, in particular if a rough sidewall profile can be produced as a roughened sidewall profile has been shown to improve the light extraction of LEDs.

A detailed study of multiple foci technology has been successfully conducted here for the singulation of 430 µm thick sapphire samples with a 1064 nm picosecond laser. Commercially available multifocal lens and focusing optics were employed for ease of adopting the multiple foci technology. This study highlighted the importance of a low pulse repetition rate (i.e. high pulse energy and high peak power) over a low scanning speed (i.e. more energy deposition) in producing a cleavable sample. Increasing the energy deposition alone was ineffective if high laser intensity was absent to induce nonlinear absorption within the sample. Cleavable samples could be produced by the picosecond laser with a 50 kHz repetition rate, scanning speeds of 1 mm/s or below and at 1.13 W laser power. The focused spot diameters depended on the effective focal length employed. The cleaved samples revealed a non-uniform roughened sidewall profile as a result of nonlinear modification at the various foci spots. Such a profile is desirable for light extraction in LEDs.

An innovative proposal for a more effective use of laser energy was explored with multizone scanning. Selected sections of the sample's thickness were scanned successively, allowing for heat dissipation between scans. For two-zone scanning of samples, two out of three sections of equal thickness were irradiated at 0.57 W for each scan. Each zone consists of 9 foci with a focused spot diameter of 2.20 μm. Diffractive order 0 (i.e. at the focal length of the focusing optic) was focused at the midpoint of each zone. At a 50 kHz pulse repetition rate and 10 mm/s scanning speed, a cleavable sample was produced when only the top two-thirds of the sample's thickness was

scanned, namely with the middle section scanned first and the upper section scanned next. Even only a portion of the thickness was scanned, the cleaved sample revealed a uniformly roughened sidewall profile, spanning across the entire sample's thickness. Therefore, two-zone scanning produced a cleavable sample with a roughened sidewall profile, simultaneously achieving more desirable results with less energy deposition.

To summarize, this study represents the first investigation on the effects of sample surface roughness interaction with a laser beam. The sample with a single rough bottom surface exhibited the highest level of absorptivity as a result of internal reflection at the exit surface. Multiple foci laser technology for sapphire singulation was first explored in this investigation. Nonlinear modification occurred at various foci spots such that cleavable samples revealed a non-uniform roughened sidewall profile. Two-zone scanning of the top two-thirds of the sample only resulted in cleavable samples with a uniformly roughened sidewall profile throughout the sample's thickness. This is a novel approach of multizone scanning of sapphire samples resulted in improvement of process efficiency and effectiveness.

Acknowledgements

I would like to acknowledge the financial support provided by Singapore Institute of Manufacturing Technology (SIMTech) of Agency for Science, Technology and Research (A*STAR).

I would like to thank Prof Lam Yee Cheong of the School of Mechanical and Aerospace Engineering at Nanyang Technological University. His insightful comments and advice on research and life lessons have helped me improve as a student, a researcher and as a person. Most of all, I am thankful to him for accepting me as his Masters student.

I would also like to extend my gratitude to Dr Wang Zhongke of Singapore Institute of Manufacturing Technology (SIMTech). His never-ending patience and guidance helped me through the completion of this thesis. He was always available whenever I encountered a problem and required advice. He was approachable and knowledgeable and I felt reassured after my consultations with him. I am grateful to him in making my research interesting and enjoyable.

I would like to thank Mr Wan Yin Chi of Singapore Institute of Manufacturing Technology (SIMTech). His assistance and guidance on the operations of the laser equipment expedited my progress.

I would like to express my gratitude to my parents for supporting me in my graduate studies - to my father for his inspiration to further my studies, and to my mother for her constant encouragement and unwavering support. I would not have made it without them.

I would also like to thank my friends for their friendship and emotional support. Life as a student would not have been as enjoyable without them.

List of figures

List of tables

List of symbols

Symbol	Unit	Description
A		Absorbance
D	m	Unfocused beam diameter
DOF	m	Depth of focus
f	m	Effective focal length
F	J/m^2	Fluence
f_D	m	Focal length of multifocal (diffractive) lens
f_m	m	Focal length of diffractive order m
$f_{m,n}$	m	Focal length of diffractive order m in material with refractive index n
f_R	m	Focal length of focusing (refractive) lens
I	W/cm^2	Power density
m		Diffractive order
M^2		Beam quality factor
n		Refractive index of material
N		Number of pulses overlap
P	W	Average power
Q	J	Pulse energy
R		Reflectance
R_p	Hz	Pulse repetition rate
Ra	m	Roughness average
Rz	m	Difference between highest peak and lowest valley for roughness
T		Transmittance
v	m/s	Scanning speed
z	m	Reference height with respect to the top surface of sapphire
z_R	m	Rayleigh length
α	Degree (°)	Plane of surface roughness with respect to reference polished surface
Δz	m	Step size for scanning height
λ	m	Wavelength of light
ω_0	m	Focused spot radius
$\omega(z)$	m	Defocused spot radius at z
Φ	Degree (°)	Divergence angle
ϕ	m	Focused spot diameter

Symbol	Unit	Description
Θ	Degree (°)	Divergence half angle
θ	Degree (°)	Angle of light with respect to normal
θ_c	Degree (°)	Critical angle
θ_i	Degree (°)	Angle of incident light
θ_r	Degree (°)	Angle of refracted light, unless otherwise stated
θ_1	Degree (°)	Angle made on entry surface, unless otherwise stated
θ_2	Degree (°)	Angle made on exit surface, unless otherwise stated

Contents

1 Introduction

1.1 Background

Sapphire is used as a substrate in many applications. Industrial sapphire is grown as single crystals. On the Mohs scale for crystal hardness, diamond is ranked the hardest crystal, with the highest value of 10 Mohs, and sapphire is ranked second with a value of 9 Mohs [1]. To quantify hardness in terms of Pascals, the sapphire has a high hardness of 22-25 GPa [2], [3], which is second to diamond with a hardness value of 80-92 GPa [4], [5]. Sapphire is chemically inert and optically transparent (for wavelengths ranging from ultraviolet to infrared) [5], [6]. These properties enable sapphire to be a substrate in the manufacturing of watch covers, phone displays, integrated circuits and optoelectronics [5], [6], [7].

More importantly, sapphire is the main substrate in the manufacturing of light emitting diodes (LEDs) as it is economically viable. Although silicon and silicon carbide have been tested as a substrate for LED manufacturing, from an economic and manufacturing quality standpoint, these materials are not deemed to be suitable for large scale production [6].

Diamond saw cutting is widely used for the cutting of sapphire boules. Diamond is employed as it is harder than sapphire. However, since a diamond saw blade has a measurable width, it dictates the kerf width and the corresponding amount of material lost. Indeed, with this cutting method, about 50% of the material is wasted [7]. Additionally, cooling is required as the cutting process produces heat due to friction between the blade and the material. The mechanical stresses from the pressure of the diamond saw on the material may produce outputs containing chips [8]. For these reasons, the yield, the efficiency of the process and the quality of the outputs are reduced.

Lasers have been introduced as an alternative tool to dice brittle sapphire wafers [9]. It is a preferred tool as lasers are considered as a contactless tool. The newer method of laser scribing modifies the top surface of the sapphire to form an indentation due to the high laser energy used. After which, a mechanical cleaving process is carried out to completely separate the sapphire. The efficiency of this method is reduced due to the two-step process of laser ablation and mechanical cleaving. Moreover, it also produces a large quantity of debris and requires further cooling of the heat zones along the ablated region. The process is not only slow but also unreliable as it can lead to breaking or cracking of the products [5], [10].

Stealth dicing minimizes the amount of top surface debris produced by focusing the laser to a location within a transparent material, such as glass and sapphire. For an optically transparent material, a high intensity ultrashort pulse laser is necessary such that it can interact nonlinearly with the material to modify the interior of the material. With this arrangement, the kerf width and debris produced can be kept to a minimum [10]. However, the existing method only utilizes one laser focal point within the material. This could result in uneven thermal and mechanical stress distributions along the material thickness. In turn, it may form cracks within the material and produces an unevenly cut sidewall. It is difficult to control the various relevant parameters to ensure a clean and complete separation of sapphire, especially for different material thickness.

Multifocal optics has been introduced to assist the stealth dicing of other transparent materials of different thickness, such as glasses and crystals. Such an approach has resulted in promising results of a smooth sidewall and material that are free of cracks and surface damage [11], [12].

Using an ultrashort pulse laser, this investigation proposes to study various commercially available multifocal optics along with stealth dicing methods to produce a clean and well-separated sapphire material. By focusing the laser energy at various focal points simultaneously within the material, the energy can be distributed within the thickness of the material. This results in a minimal temperature gradient between the laser focal area and the surrounding material, reducing the probability of crack deviations.

Although this method has been proven applicable for the separation of transparent glasses and crystals of various thickness [12], as the properties of sapphire are different, it is by no means certain that the same approach is applicable for sapphire. In addition, even if the same approach is applicable, independent experiments must be conducted to establish the various parameters, including those of multifocal optics, for a controlled separation of sapphire.

This proposed investigation also aims to improve the efficiency of the cutting process by ensuring sapphire can be separated after interacting with the laser in a single pass, instead of using multiple laser passes at the same location which increases the probability of heat damage. Even if mechanical breaking is required after laser irradiation, the heat effects on the wafer are kept to the minimum with a single pass. The ultimate goal is to result in a controlled separation of sapphire.

Understanding the effect of surface morphology, namely surface roughness, of a sapphire sample on light interaction will allow for better decision making either to exploit or avoid a particular effect for specific machining requirements. In the instance of using laser for singulation purposes, it would be beneficial for the material to absorb more light during laser irradiation. The energy absorbed can be used to modify the internal properties of sapphire for easier wafer separation.

1.2 Motivations for research

Current studies on multiple foci laser cutting have been mostly focused on transparent glass cutting with highly specialized focusing optics. Although yet to be explored, such laser cutting with multiple foci technology could well be extended to the cutting of transparent sapphire. Sapphire has different material properties as compared to glass, such as refractive index, interaction with light and absorption characteristics, to name a few. A study is required to ascertain that multiple foci laser cutting can also be applied for sapphire singulation. Therefore, this investigation aims to explore the use of commercially available multiple foci lenses to separate sapphire wafers with a short pulse laser.

Previous studies concluded that after laser irradiation, a roughened sidewall (i.e. the cleaved surface of the sample) was desirable for increasing light emission in LEDs with sapphire as a substrate [13], [14]. The roughened sidewall decreases the effect of internal reflection within the material and allows more photons to escape, which leads to an increase in light extraction efficiency. Indeed, using a multiple foci laser cutting technique could well facilitate the generation of a roughened sidewall and without the loss of efficiency associated with multiple scans.

The introduction of patterned sapphire substrates (PSS) as an improvement to the conventional sapphire substrates has been gaining attention [15], [16], [17]. For LEDs, the rough patterned surface is desirable as it boosts the LED light extraction by increasing light scattering. The PSS structure are currently etched into the individual sapphire chips before the LED layers are grown, which could be a time consuming process. It would facilitate industrial scale production if the patterns were etched onto the sapphire wafers before singulation. The PSS poses another challenge for laser singulation due to the apparent rough patterned surface.

Hitherto, a study of the change in optical properties of sapphire as a result of a change in its surface morphology has not been conducted. Although a sapphire sample might be transparent allowing stealth dicing, its “apparent” absorptivity might change due to the change of light interaction with a change in surface roughness. As such, it will be of interest to study the interaction between light and samples with different surface morphology during laser irradiation. The configuration that allowed for the most desirable absorption within the transparent medium can be determined. With the findings, such phenomenon can be either exploited or avoided depending on the purpose of machining. In the case of sapphire wafer singulation, a greater level of absorption evenly distributed would be preferable.

Experiments in this investigation will not be carried out in a vacuum environment, as the investigation of Lee et al. indicated that a vacuum environment was not necessary [18].

1.3 Objectives and scope of investigation

The scope of this thesis is confined to using a 10.3 ps laser with a wavelength of 1064 nm to irradiate 430 μm thick sapphire wafer samples in the c-plane crystal orientation. Commercially available multifocal (MF) lenses, that produce either 9 or 27 focal spots, were employed in the laser experiments involving multiple foci technology. The MF lenses were paired with commercially available focusing optics, i.e. objective lenses or conventional focusing lenses, each with a unique fixed effective focal length (EFL).

This investigation aims to examine both the linear and nonlinear interactions between the laser beam and sapphire wafers with different surface roughness. A detailed study of multiple foci technology will be conducted on the laser singulation of sapphire. An innovative proposal of multizone scanning was explored for better effectiveness of laser energy usage.

The ultimate aim is to employ multiple foci laser technology for the singulation of sapphire samples and produce a roughened sidewall after sample cleavage that enhances the light emission of LEDs. The individual objectives of the investigation may be summarized as:

1. Examine both linear and nonlinear interactions between the laser beam and sapphire samples with different surface finishes, and to deduce the optimum sample option for machining applications.
2. To examine and to hypothesize the mechanism of the effect of surface roughness on the absorptivity of laser beam energy.
3. By single pass (single zone) scanning of the sample, adapt multiple foci technology to laser singulation of sapphire, and to produce a cleavable sample with a roughened sidewall profile.
4. Explore multi-pass (two-zone) scanning of sapphire with multiple foci technology to improve the effectiveness of laser energy usage and quality of the roughened sidewalls in cleaved samples.

1.4 Organization of thesis

Chapter 1 contains an introduction of sapphire and singulation methods. This chapter also presents the motivation behind this research, the objectives and scope of investigation, and the organization of the thesis.

Chapter 2 provides a review on methods for sapphire singulation which mostly involved the use of lasers. Multiple foci laser cutting on other transparent and brittle materials was also discussed. A brief introduction on the crystalline structure of sapphire is given. The light emissions of LEDs after laser irradiation was examined, and a brief discussion on PSS was presented.

Chapter 3 hypothesizes the ways in which light interacts with sapphire wafers of various surface morphologies in the linear regime. Depending on the surface morphology and the orientation of a sample, internal reflection of light within the sample is possible.

Chapter 4 presents the sapphire wafer samples and the measuring equipment employed to characterize the surface roughness and linear optical properties of the samples. It also presents the laser machine, power sensor, laser optics and mechanical cleavage setup.

Chapter 5 investigates how and why the surface morphology and the orientation of the samples affect the linear optical properties of the sapphire wafers. This chapter quantifies the surface roughness and the optical spectrometry data of the samples. It examines how samples of different surface morphologies interact with a single focus laser with various laser powers. The nonlinear absorption threshold of sapphire and its changes with different surface morphology and orientation of the samples were studied.

Chapter 6 presents the experiments performed with multiple foci technology on sapphire samples with a single pass. The sets of operating parameters most suitable for sapphire singulation by laser irradiation with multiple foci technology were investigated.

Chapter 7 explores multizone scanning of sapphire samples with multiple foci technology. The samples were scanned on the same scanning line more than once at different scanning zones. Results obtained provide the appropriate combination of scanning zones for an effective and efficient separation of sapphire samples.

Chapter 8 concludes this research and indicates potential future work for issues yet to be resolved by this investigation.

2 Literature review

2.1 Overview

For its transparency and high hardness, sapphire can be used as optical windows, in microfluidics [19], opto-electronics and micro-mechanical applications [20]. It is also slated to be used in next generation touchscreens [21]. Indeed, sapphire is known to be a versatile substrate that is commonly found in the semiconductors industry for the manufacturing of LEDs [13], [14].

For all the applications, the singulation of sapphire wafers is a required and essential manufacturing process. There is a wide range of mechanisms developed to separate sapphire wafers. The various methods range from contact methods such as diamond wire cutting to contactless methods such as laser cutting. Diamond wire cutting is a conventional and standard method for the singulation of sapphire wafers. However, laser methods are more favorable to traditional cutting as they are faster and produces smaller kerf widths with less debris formation. Hence, less material is lost resulting in an increase in effectiveness and yield. More importantly, less heat is generated which minimizes the thermal damage on the substrate. Since the process is contactless, there will be minimal tool wear [5], [10].

More commonly known laser separation methods are through laser scribing and stealth dicing. Stealth dicing of sapphire wafers has been given more emphasis in recent years [13]. Stealth laser cutting requires the laser focal point to be placed within the transparent material. This further minimizes debris formation and kerf widths [10].

2.2 Crystal structure of sapphire

Industrial grade sapphires are scientifically known as single crystal corundum. Corundum is a type of mineral. Sapphire is also referred to as the α phase of aluminum oxide with a chemical formula of Al_2O_3 [22], also known as α-Al_2O_3 [23].

Al^{3+} cations and O^{2-} anions are bonded together in a hexagonal crystal lattice. Al^{3+} cations have a smaller ionic radius than O^{2-} anions, i.e. 0.57 Å and 1.40 Å respectively. The larger O^{2-} anions can be imagined as spheres and are closely packed together. Due to the shape of the anions, an octahedron hollow is formed between six spherical O^{2-} anions. Two-thirds of these octahedron hollows are filled with the smaller Al^{3+} cations and therefore there is no symmetry center for the cations. The Al^{3+} cations distort the crystal lattice minimally and the structure remains stable.

A schematic of the hexagonal crystal lattice of sapphire is shown in Figure 2.1. In the schematic, looking in the direction of the c-plane axis, the larger O^{2-} anions are depicted as larger white circles, the smaller Al^{3+} cations as small black circles and the octahedron hollows as smaller white circles. Only a single lower basal plane of the O^{2-} anions were shown. Hence, the octahedron hollows appeared to be only surrounded by three O^{2-} anions. The <$11\bar{2}0$> translational vectors are depicted as A_1, A_2 and A_3.

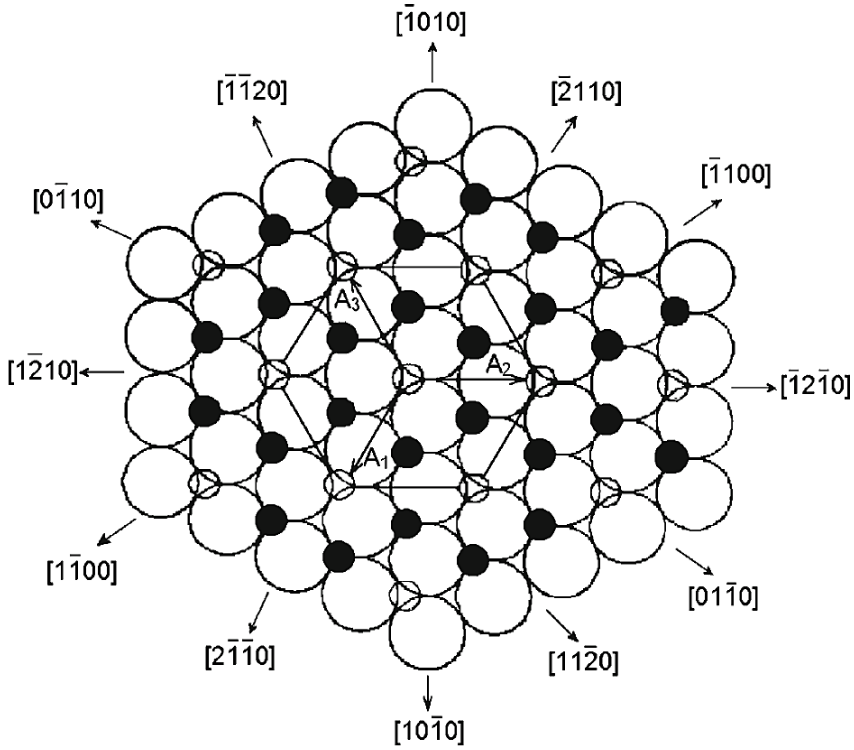

Figure 2.1 Schematic of crystal lattice of sapphire [24]

Sapphire is grown upwards in the <0001> c-plane direction as illustrated in Figure 2.2. Since the Al^{3+} cations occupy two-thirds of the octahedron hollows, the positions of the unoccupied octahedron hollow changes in each layer and the patterns are repeated every three layers. Due to the layering of the larger O^{2-} anion spheres, the entire structure with both Al^{3+} and O^{2-} ions are repeated every six layers of each ion (i.e. Layers 1 and 7 are the same) [24].

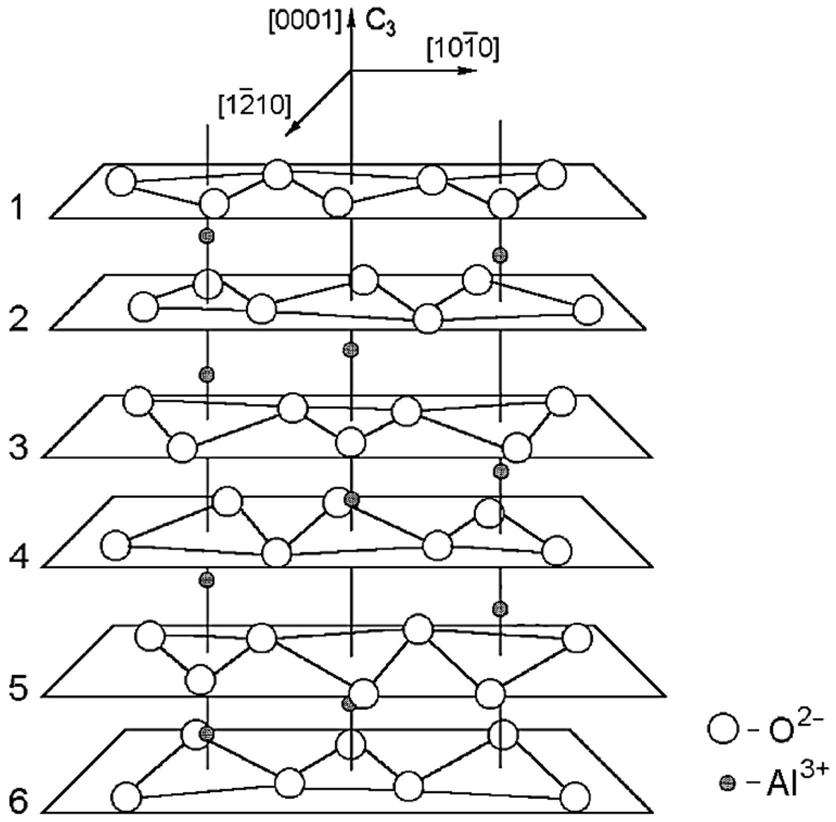

Figure 2.2 Schematic of the layering of Al^{3+} *and* O^{2-} *ions in sapphire [24]*

2.3 Cutting of sapphire wafers

The various cutting techniques and the associated mechanisms for sapphire cutting will now be introduced and discussed.

2.3.1 Diamond wire cutting

The dicing of sapphire wafers using diamond saw is the standard method and has been extensively studied. Kim et al. studied the effect of the initial deflection of a diamond wire on the variation of thickness of sapphire wafers [25]. A single diamond wire saw machine that was equipped with a core wire of 0.18 mm in diameter, with diamond abrasives of diameter 30-40 μm, was used. The sapphire ingot had a cross sectional area of 50 mm × 50 mm. The study concluded that the variation in wafer thickness was highly dependent on the cutting speed and diamond wire wear, which can be controlled by fine-tuning the initial wire deflection. A consistent thickness was favored as post processing time and production cost to remove the inconsistency could be minimized.

2.3.2 Laser scribe and break

Tamhankar et al. studied sapphire wafer singulation with the laser scribe and break technique [26]. A diode pumped solid state (DPSS) Q-switched laser with a wavelength of 355 nm was used. The laser had a pulse width of 18-28 ns and a repetition rate of 150 kHz. A 400 μm thick, single crystal, single side polished sapphire sample was used in the experiments. Laser was incident on the unpolished surface. Fluence, pulse width and repetition rate were varied in the parametric study. The cutting depth and kerf width were measured subsequently. The laser was focused within the material which resulted in deeper cuts. It was concluded that shorter pulse widths lowered the threshold for material removal, which resulted in deeper, cleaner and narrower scribes with a reduced heat affected zone (HAZ) at lower fluence levels, see Figure 2.3. Higher repetition rates allowed for faster scribing speeds with deeper scribes, see Figure 2.4. A more noteworthy conclusion in the ablation of sapphire was that for higher repetition rates, it was better to split the excess energy over the optimal value into several beams at optimal energy.

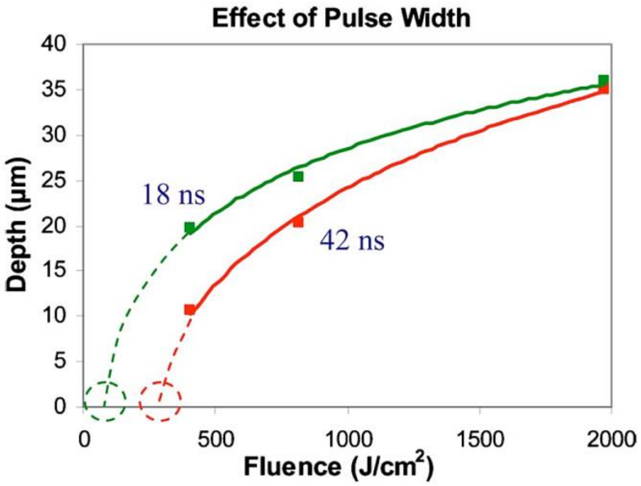

Figure 2.3 Graph of scribe depth against laser fluence on sapphire sample. A shorter pulse width resulted in deeper scribes with the same laser fluence [26]

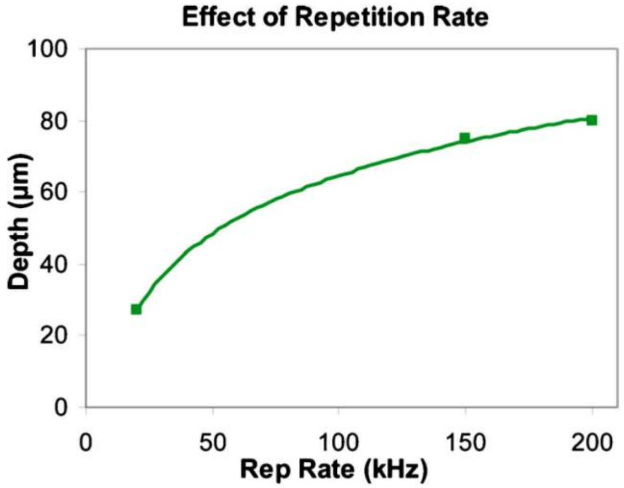

Figure 2.4 Graph of scribe depth against pulse repetition rate [26]

Although Tamhankar et al. employed a single side polished sapphire wafer with the laser incident on the unpolished surface, no reason was given for choosing this configuration. However, as surface roughness has an effect on light propagation direction, a better understanding can be gained through a study on the light-material interaction for different surface finishes, i.e. the difference between a smooth polished surface and a rough unpolished surface. With such knowledge, different mechanisms can be exploited for different machining purposes.

2.3.3 Stealth dicing

Yadav et al. studied the stealth dicing of sapphire using near infrared (NIR) femtosecond lasers [10]. The employed a 800 nm (NIR range) Ti:Sapphire with a pulse width of 140 fs and a repetition rate of 1 kHz. Microscope objectives, with 100×, 20× and 5× magnifications, were chosen as focusing optics. The single side polished sapphire wafer had a thickness of 350 μm. Even with a low absorption coefficient at a wavelength of 800 nm, it enabled stealth dicing to occur. Within the thickness of the transparent sapphire sample, a single focus spot was placed below the middle of the thickness. At high intensity levels, multiphoton absorption occurred. It was suggested that once the threshold for nonlinear absorption was surpassed, nonlinear absorption will occur at the laser focus. The damage will be localized and will not affect the other regions within the structure. The single focus within the sample will induce a line of stress points within the sapphire as a result of the moving laser beam. The sapphire can then be easily cleaved mechanically for a high quality separation even for thick sapphire samples. The results from scanning electron microscope (SEM) and atomic force microscopy (AFM) are presented in Figure 2.5. Each spot received a hundred laser pulses. Even though ripples were observed around the focal spots due to nonlinear absorption, the mechanically cleaved regions were observed to be smooth and have a low surface roughness of about 20-50 nm (Figure 2.5b-d). Additionally, chipping was observed on the top surface at the beam side (Figure 2.5a).

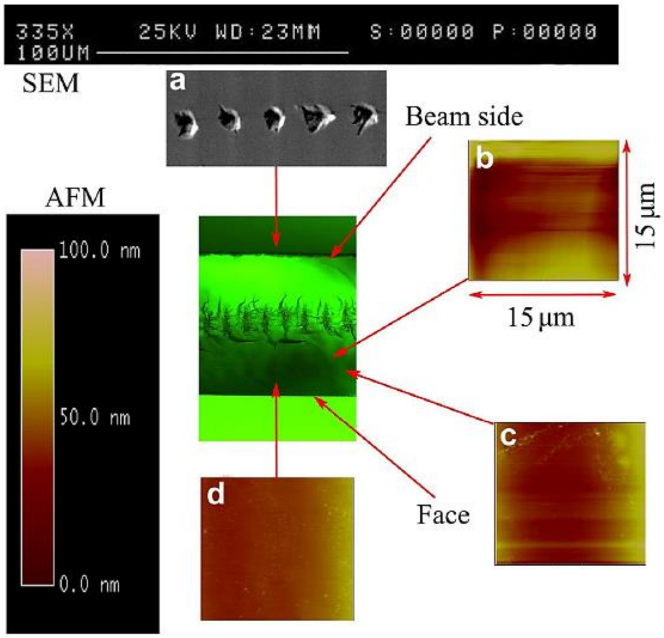

Figure 2.5 SEM and AFM results from stealth dicing of sapphire [10]

With a high pulse energy and high repetition rate, only one scan was required to weaken the internal structure. This enabled the process to be carried out quickly. Furthermore, this method was applicable for the dicing of blue or violet LEDs as the quality of the edge at the beam exit was good with reduced thermal damage and debris formation.

For stealth dicing, instead of using a single focus spot as in Yadav et al. [10], employing multiple focal spots simultaneously through the thickness of a sapphire sample could well be explored. With multiple foci, there will be more even distribution of laser energy through the thickness of a sample, with the potential of a better controlled dicing of the sample.

2.3.4 CO_2 Laser thermal cracking

Xu et al. controlled the thermal cleavage of sapphire wafers using laser irradiation [27]. A CO_2 laser with a wavelength of 10.6 μm was employed. The sapphire wafer used was 120 μm thick that housed a 5 μm thick gallium nitride film. Their study concluded that a guide groove formed by laser ablation prior to wafer cleavage would guide the crack extension without deviation. The thermal cleavage resulted in a smooth cross-sectional surface of the sample without damage, see Figure 2.6. When processing successive scans, ample time between scans must be allowed for temperature and mechanical stresses to dissipate. Otherwise, the asymmetrical thermal and mechanical stresses from adjacent scans due to heat conduction will cause the crack to deviate from the initial scribed lines.

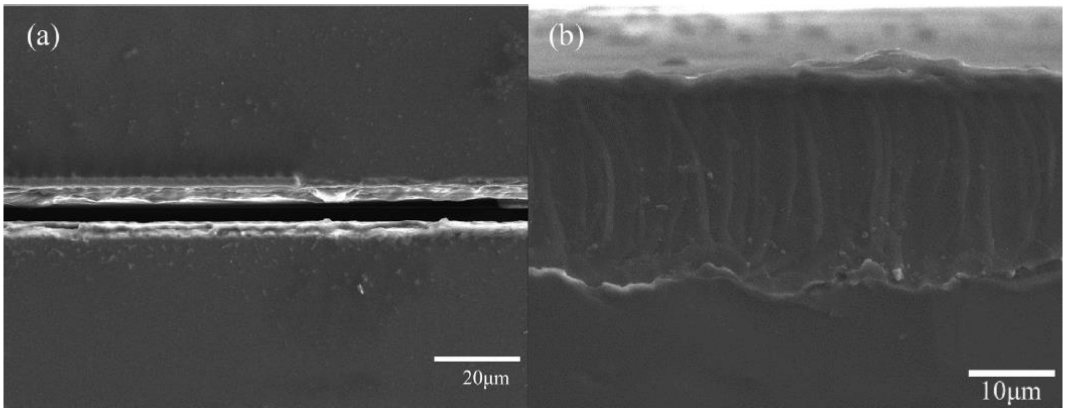

Figure 2.6 Optical images of sapphire after controllable laser thermal cleavage of (a) surface and (b) cross section [27]

The simulation setups and numerical results for structural stress analysis are presented in Figure 2.7 and Figure 2.8 respectively. For the single scan in Figure 2.7 (a), the mechanical stress distribution in sapphire was symmetrical as shown in Figure 2.8 (a). For the two scans in Figure 2.7 (b), the first scan on the left exhibited a symmetrical mechanical stress distribution, see Figure 2.8 (b). However, Figure 2.8 (b) also shows that due to insufficient time for heat dissipation, the second scan on the right displayed an asymmetrical mechanical stress distribution. Therefore, crack deviation in the sample was possible.

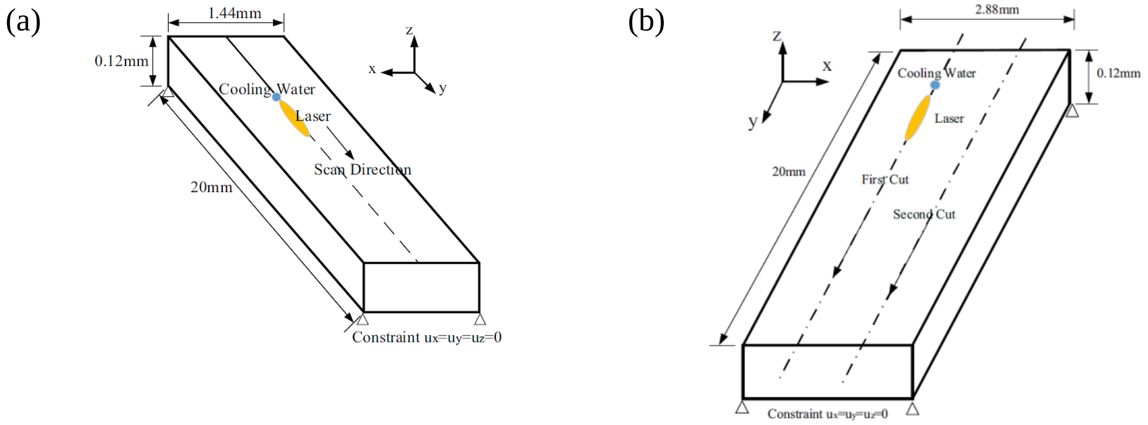

Figure 2.7 Schematics of simulation setup for an elliptical beam spot for (a) a single scan and (b) two scans [27]

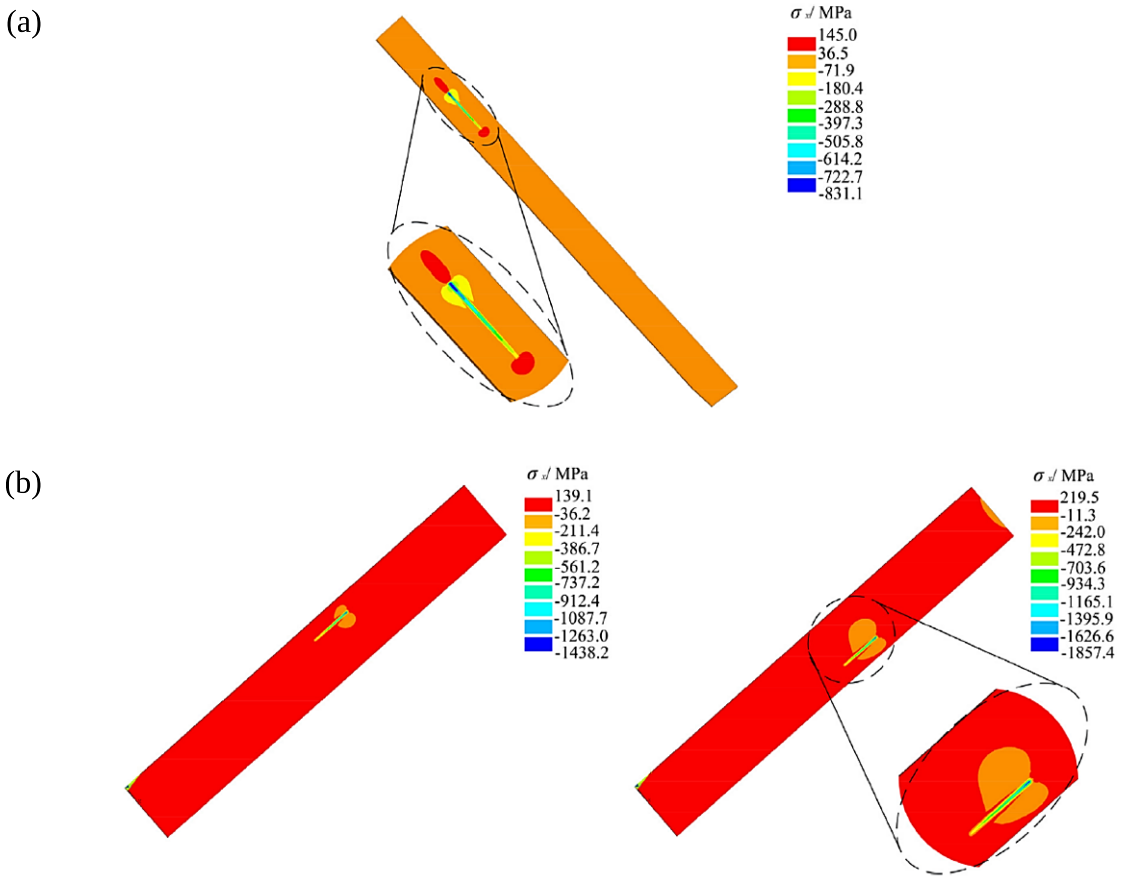

Figure 2.8 Numerical solutions for an elliptical beam spot for (a) a single scan and (b) two scans [27]

2.3.5 Laser-induced plasma assisted cutting

Lee et al. devised a method to separate blue LED wafer via the laser-induced plasma-assisted ablation (LIPAA) technique [18]. The laser used was a Nd:YAG, Q-switched laser with a wavelength of 1064 nm. It had a pulse width of 150 ns and a power of 5 W. A galvanometer equipped with a f-theta lens with a focal length of 163 mm was employed for laser scribing. The experiment was carried out at atmospheric pressure without a vacuum. In LIPAA, the transparent sapphire was placed on a metal plate. The laser was focused through the sapphire onto the metal plate. After which, the high intensity laser generated plasma from the metal plate was then used to scribe the underside of the sapphire, see Figure 2.9. It was concluded that a nickel coated steel was the best choice for plasma generation. Although no explanations or details were provided, it was observed that placing the wafer sample closer to the metal plate resulted in easier scribing, but it was more difficult to separate the wafer from the metal plate. To avoid the necessity of separating the wafer from the metal plate, the gap between the metal plate and wafer was kept at 100 μm. When the scanning speed was decreased, the depth of scribing increased. However, when the scanning speed was excessively slow, uncontrollable thermal cracks were observed.

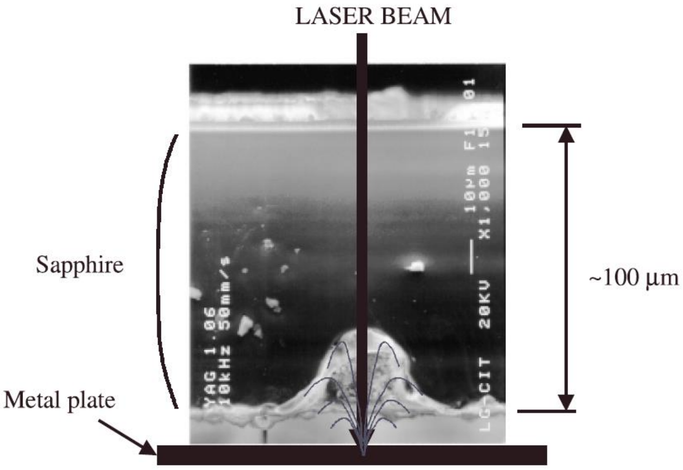

Figure 2.9 Laser irradiation through sapphire onto metal plate using the LIPAA technique [18]

2.3.6 Bessel beam cutting

Tsai et al. investigated the use of Bessel beams to separate fused silica [28]. Femtosecond Bessel beams were formed by a Ti:Sapphire laser with a wavelength of 800 nm and a regenerative laser amplifier source. The laser had a pulse width of 120 fs, a repetition rate of 1 kHz and a power of 250 mW. The Bessel beam was produced using an axicon lens with a wedge angle of 5° and a refractive index of 1.453. After the laser beam propagated through the axicon lens, the outspread laser intensity distribution of a Gaussian beam profile was transformed into a highly concentrated Bessel beam profile, see Figure 2.10.

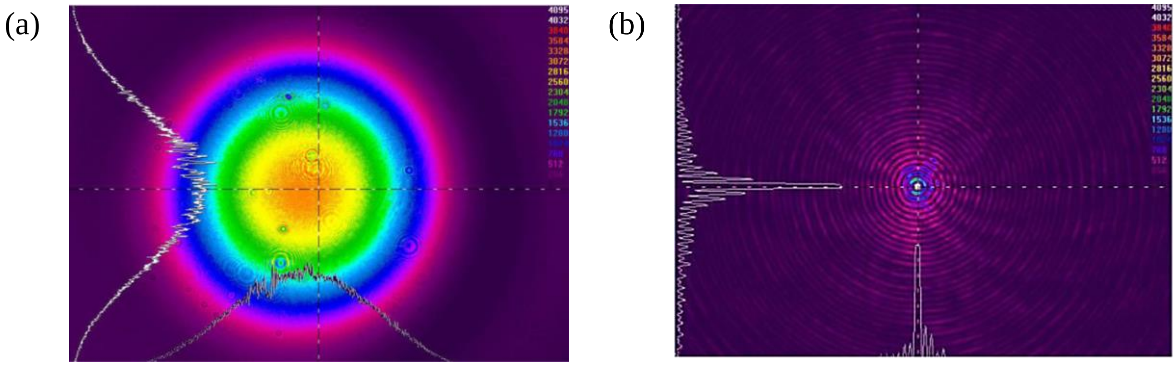

Figure 2.10 Beam profiles of (a) a Gaussian beam and (b) a Bessel beam [28]

Two thicknesses of fused silica were used. The thicker glass was 45 mm thick, while the thinner glass was a flexible glass display with a thickness of 100 μm. On the thicker glass, the pulse number was increased to a maximum of 1000 shots at a single point and only a slight change in the diameter and depth of modification was observed, see Figure 2.11. Hence, the diameter and depth modification depended more on the geometry of the beam than the number of shots. The modified zone had an average width of 6.7 μm and a depth of 3 mm, with a variation in width of less than 9%. Therefore, the upper portion of the Bessel beam was selected for thin glass cutting for a more uniform cutting width and an even distribution of lateral residual stress. A scanning speed of 1 mm/s, which translated to 1 μm/pulse, was used for laser irradiation on the thinner glass. The thin glass was well separated through internal modification and breakage, with chipping of less than 1 μm along the separation edge.

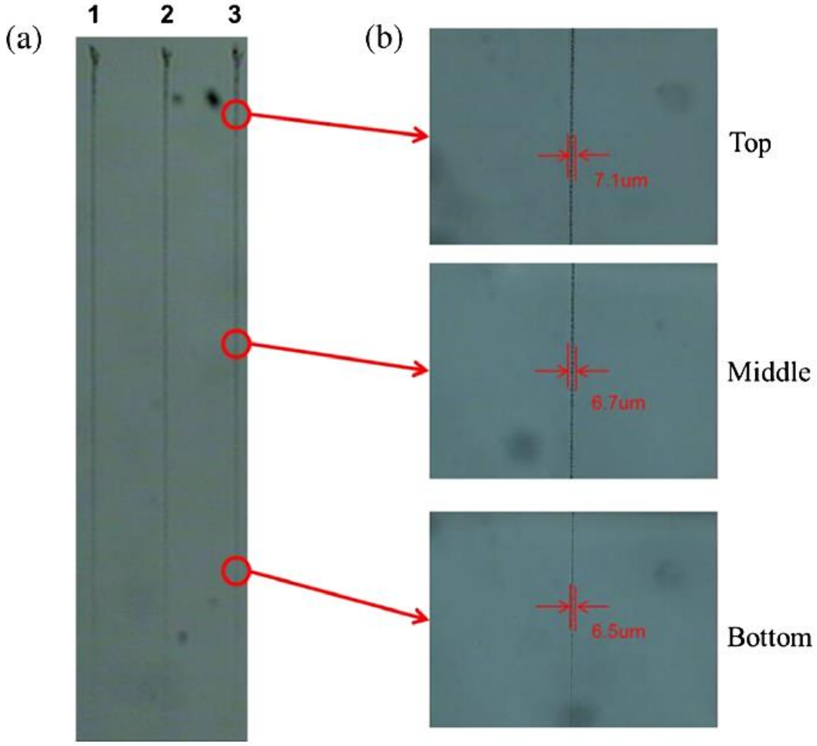

Figure 2.11 Cross sectional view of laser irradiation within sapphire using Bessel beams of 1000 pulses for (a) overall view and (b) at the top, middle and bottom regions [28]

Rapp et al. utilized picosecond and femtosecond Bessel beams for stealth dicing of sapphire wafers through controlled crack formation and propagation [21]. The nature of the Bessel beams allowed uniform damage in the longitudinal direction. With a high repetition rate and a high energy level, shots were spaced out a few micrometers away from each other. This resulted in long vertical damages in the bulk sapphire thickness. The cracks then joined and thus formed a cleavage plane with less laser pulses. The transverse morphology of the top surface was vastly different for 3 ps and 140 fs pulse durations. For the picosecond pulses, three-fold cracks were observed that corresponded to the hexagonal lattice of oxygen in Al_2O_3 (sapphire). While for the femtosecond pulses, cracks were only formed in one direction. Therefore, femtosecond pulses enabled a fast separation of sapphire without tapering or chipping.

2.3.7 Multiple foci laser cutting

Hitherto, there are no reports on laser cutting using multiple foci technology that has been implemented in the dicing of sapphire wafers. However, such technology has been studied intensively in the singulation of crystals and glasses.

Liu et al. explored using laser multi-focus separation (LMFS) technology in the separation of thick transparent potassium dihydrogen phosphate (KDP) crystals that were four times thicker than existing techniques [11]. Two lasers were employed for LMFS. Firstly, a femtosecond laser with a wavelength of 1030 nm was used to form pretreated lines within the crystal to increase the absorptivity and weaken the bonds of the material. Next, a second continuous wave fiber laser of 1070 nm wavelength was utilized to form the multiple foci within the crystal. The 50 mm thick crystal was placed between two concave reflectors, one of which housed a small pore that was sufficiently large for the laser beam to pass through while maximizing the reflection of the laser, see Figure 2.12. The laser beam was first focused by the focusing lens within the crystal. Since the transparent crystal has low absorptivity, light that was not absorbed by the crystal will be reflected by the rear concave reflector back into the crystal again at another focus. The cycle repeated until the energy was fully absorbed by the crystal through either linear or nonlinear absorption. With this setup, three foci were formed within the crystal. As a result of heating within the crystal, the temperature difference between the crystal surface and the interior induced a higher tensile stress to form at the surfaces. Thus, microcracks formed on the surfaces quickly extended to the middle of the crystal, forming a penetration crack. The resulting sidewall profile was smooth with some ripples observed near the top and bottom regions due to a tearing effect from the higher tensile stresses induced. Although the MFLS technique succeeded in producing several foci within the crystal, but the equipment employed did not appear to be adaptable for other transparent materials with different thicknesses. The number of foci formed was highly dependent on the laser power and the absorptivity of the material. For thinner materials, the secondary and tertiary foci may be entirely out of the material. If the absorptivity of the material was too high, it might be impossible to form a secondary focus with enough energy to induce the penetration crack.

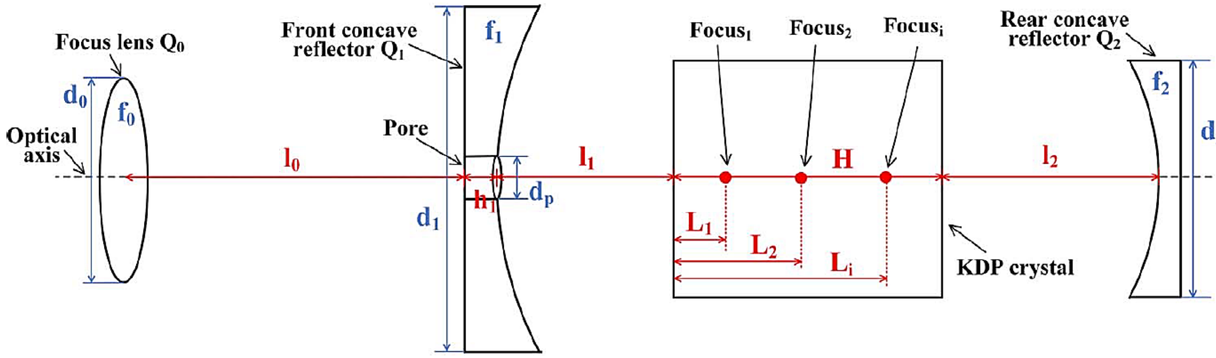

Figure 2.12 Schematic of MFLS setup with two concave reflectors [11]

Liu et al. developed the flexible multi-focus laser separation (FMFLS) technology to separate a thick glass sample that is two to four times thicker than conventional separation techniques using lasers [12]. A fiber laser with a wavelength of 1070 nm, a power of 80 W and a scanning speed of 1 mm/s was used. A soda-lime plate glass that was 20 mm thick was employed in the experiments. The optics included three coaxial focusing lenses, with each housed a hole of different diameter as seen in Figure 2.13. The outermost part of the beam would be focused by all three focusing lens and had the shortest focal length. While the center part of the beam would be focused only by the first lens and had the longest focal length. This allowed the focusing of each focus with high precision and at the same time controlling the power density of each focus. Laser power at 80 W with a scanning speed of 1000 μm/s were determined to be the optimal parameters for cutting the sample. Increasing the power level or decreasing the scanning speed away from the optimal levels resulted in the formation of slant ripples on the separated sidewall, see Figure 2.14 and Figure 2.15. When the parameters were set further away from the optimal values, deeper ripples, microcracks and even uncontrolled crack deviation were observed. This was attributed to the difference in cooling rates of the separated surface and the interior of the glass. The FMFLS technology was especially suited for cutting glass with varying thickness for aerospace, military and optics applications. To separate an even thicker glass, additional focusing lenses could be introduced, thereby increasing the number of foci, and generating a uniform thermal stress distribution, which was an important factor in the separation of a thick glass.

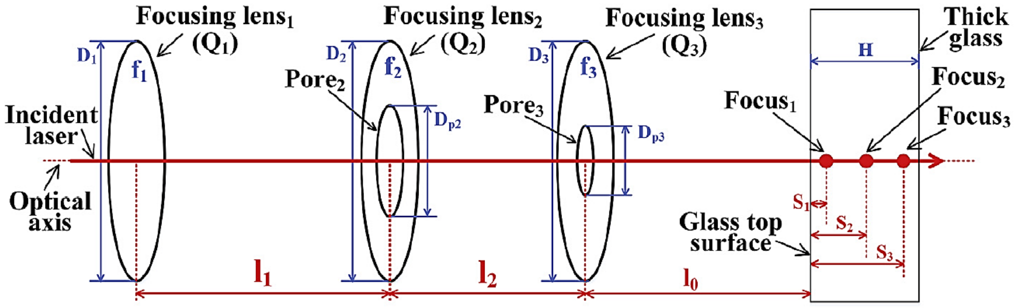

Figure 2.13 Schematic of FMFLS setup of three coaxial focusing lenses [12]

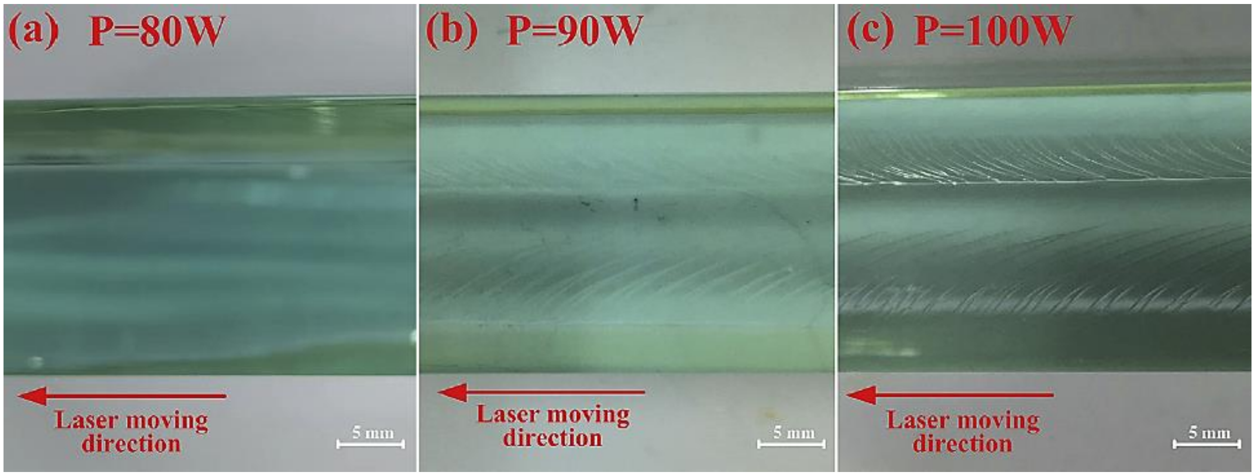

Figure 2.14 Sidewall profile after FMFLS at a scanning speed of 1000 µm/s with different powers of (a) 80 W, (b) 90 W and (c) 100 W [12]

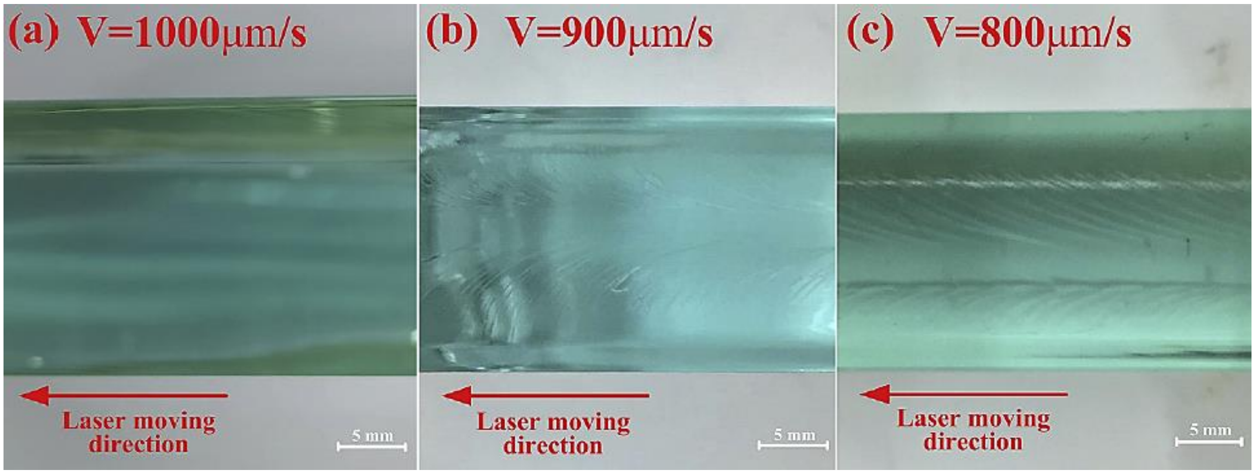

Figure 2.15 Sidewall profile after FMFLS at a power of 80 W with different scanning speeds of (a) 1000 µm/s, (b) 900 µm/s and (c) 800 µm/s [12]

2.4 Light emission of LEDs after singulation due to roughened sidewall

The performance of the LEDs after singulation employing laser cutting methods is as important as the process of singulation. The LED performance is evaluated by measuring the light extraction efficiency of the devices.

Zhang et al. studied the dicing of sapphire wafers when multiple scans were made in a single scanning line by focusing the laser within the thickness at different scanning heights [14]. They named this technique as multiple laser stealth dicing (multi-LSD). Their study used an 80 ps laser with a wavelength of 532 nm, a repetition rate of 15 kHz and an output power of 0.15 W. An improvement of 26.5% was observed when compared with multi-LSD with a nanosecond laser, and an 11.2% improvement when compared with the conventional single laser stealth dicing technique. It was concluded that the increase in light extraction efficiency of InGaN-based LEDs was due to the side emissions from the roughened sidewalls via multi-LSD. The roughened sidewalls were believed to have decreased the effect of internal reflection within the material, allowing more photons to escape. Therefore, in Figure 2.16, increasing the number of passes, from a single pass to a quintuple pass, further roughened the sidewall and the light intensity increased accordingly. The reduction of debris formation and thermal damage also contributed to the increase in light intensity.

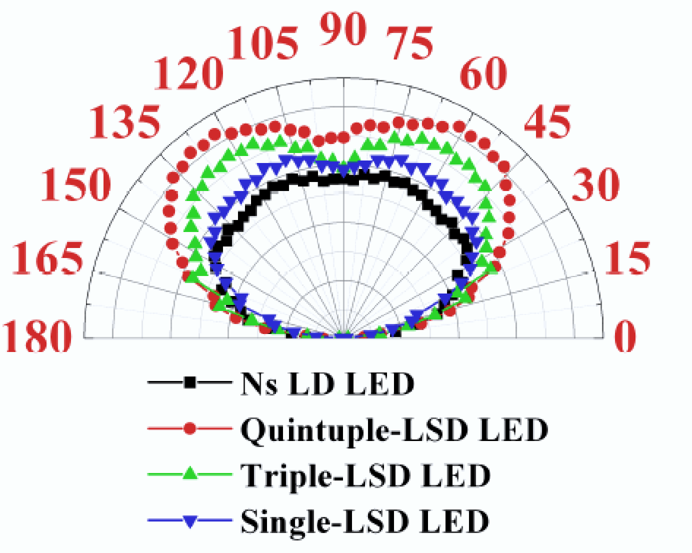

Figure 2.16 Far-field radiation patterns as a measure of light extraction efficiency for nanosecond (ns) laser dicing, multi- and single-LSD LED samples [14]

Known as shifted laser stealth dicing (shifted-LSD), Chang et al. explored a similar stealth dicing method with multiple scan lines at different scanning heights but by shifting the pulse focal position of adjacent scans [13]. In other words, the focal points for adjacent scans will not be in a vertical column but slightly displaced, see Figure 2.17. Figure 2.18 shows the sidewall profile after mechanical cleavage. The roughened layers were produced by laser-material modification and the smooth cleaved layers were a result of mechanical separation. The shifted-LSD method saw a 5.3% improvement in light emission due to the thicker roughened sidewalls as compared to a single laser scan technique with smooth sidewalls. In comparison, the multi-LSD method only saw a 3.1% improvement.

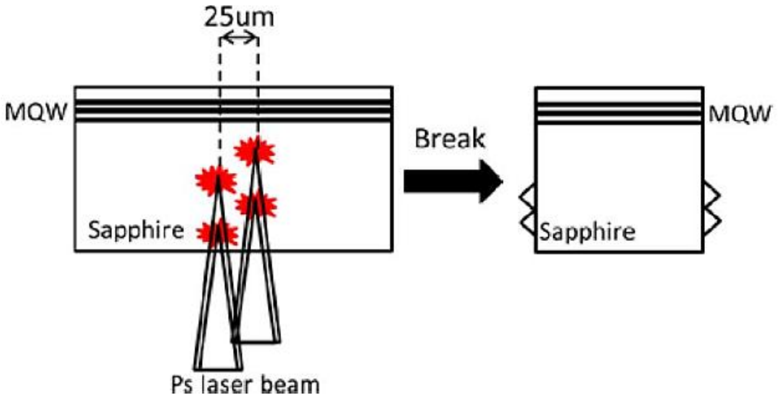

Figure 2.17 Schematic of the shifted-LSD method [13]
The active multiquantum well (MQW) region acts as a light source where photons are generated

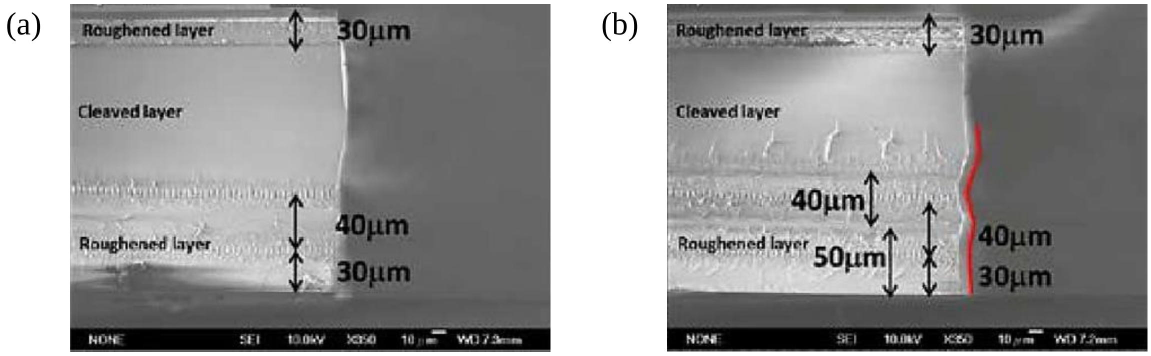

Figure 2.18 SEM images of sidewall profile for (a) multi-LSD and (b) shifted-LSD [13]

From these investigations, a roughened sidewall promotes higher light emissions due to a reduction in internal reflection within the LED. However, from a production perspective, multiple scans will be less efficient, and better and more precise control will be required.

2.5 Patterned sapphire substrates

LEDs are traditionally grown on the polished surface of a sapphire wafer. However, recent studies have suggested that the conventional flat sapphire substrates may not produce LEDs with optimal light output performance. In these substrates, most of the light generated from the active layers will be reflected into the nitride films. Since the refractive index of the nitride film was higher than sapphire, the nitride films trapped light through internal reflection and prevented light from propagating out of the LED structure. The majority of light will be propagated upwards into the various layers. Furthermore, as light propagated to the top of the LED structure, light incident on the electrodes were absorbed. Hence, it further reduced the amount of emitted light, thereby reducing the light output performance of such LEDs [15]. Instead, a novel solution in PSS was proposed.

Yamada et al. investigated the use of PSS on near-ultraviolet and blue LEDs [15]. The sapphire substrate was etched with a hexagonal pattern, with 2 μm edges and parallel to the a-axis of sapphire, through reactive ion etching, see Figure 2.19. Due to the non-flat interface between the nitride film layer and sapphire, the angle of incident light on the sapphire was changed to be more random which resulted in an increase in the scattering of light out of the LED structure through the side edges. It was reported that at 20 mA, the external quantum efficiency of a near-ultraviolet LED and a blue LED increased by 35.5% and 34.9% respectively.

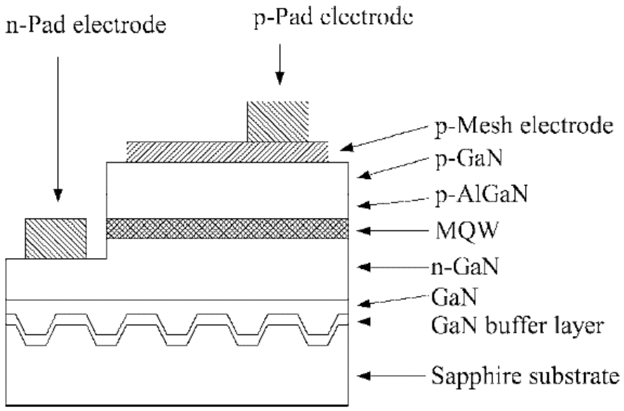

Figure 2.19 Schematic of a LED grown on PSS [15]

Wuu et al. studied the effects of PSS on the electroluminescence (EL) intensity and light extraction efficiency of LEDs [16]. Cylindrical holes, with a diameter of 3 μm and spaced 3 μm apart, were periodically etched into the c-plane of sapphire through photolithography. It was reported that PSS with a 1.5 μm etching depth produced better results. From Figure 2.20, it was concluded that PSS LEDs had larger EL intensities than that of conventional LEDs, especially in the near horizontal regions within ±45°. The improvement of EL intensities, and hence the increase of light extraction efficiency, was attributed to the scattering of light and a reduction of threading dislocations due to the structure of the cylindrical PSS.

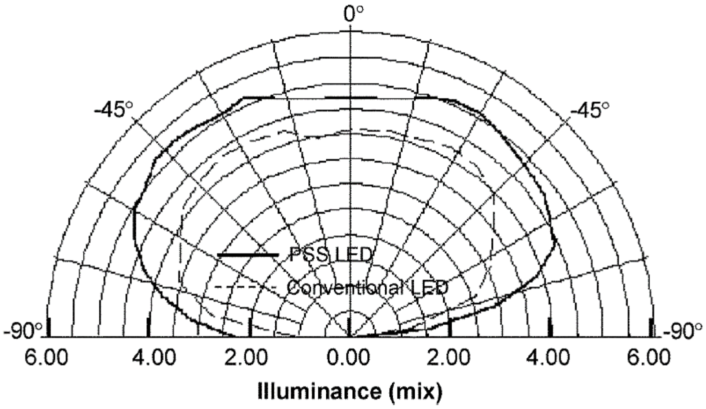

Figure 2.20 EL spectra of PSS and conventional LED [16]

Yang et al. explored the effects of different geometry of PSS on light output performance through light scattering [17]. The two geometries tested were mainly a hemispherical PSS (HPSS) and a triangular pyramidal PSS (TPSS), see Figure 2.21. The patterns were etched on the c-plane of the sapphire substrate via the inductively coupled plasma dry etching method. Both patterns had similar dimensions that were 2.4 μm in diameter and 0.4 μm in depth. The effects of fill factor (i.e. PSS area over the total area) on the light output performance were also investigated.

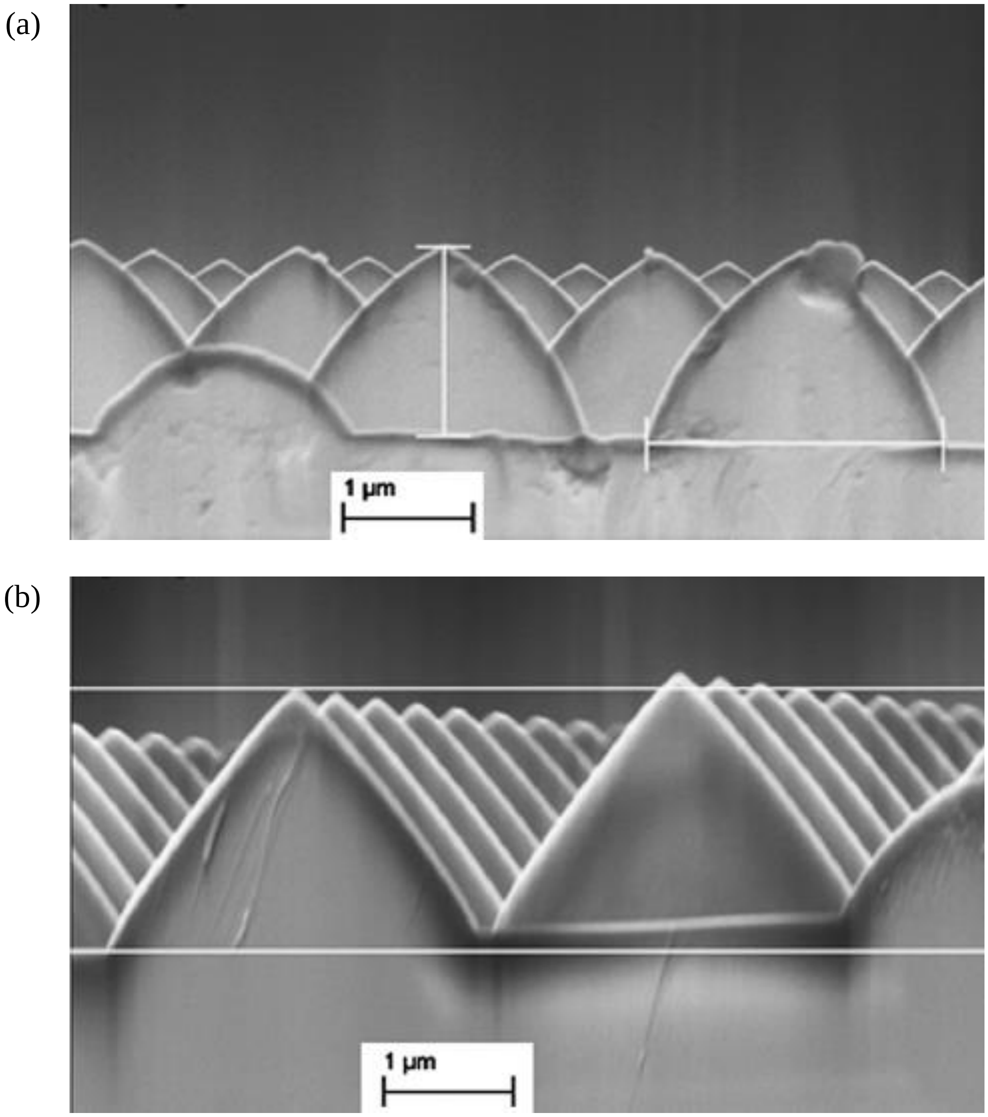

Figure 2.21 SEM images of the cross sections of (a) HPSS and (b) TPSS [17]

The authors suggested that by growing epitaxial GaN layers on PSS, it encouraged the lateral overgrowth of GaN, thereby producing better epitaxy quality of the LEDs. A better crystalline quality was achieved with the TPSS. The electrical properties of the PSS LEDs were enhanced as the leakage currents were much smaller than that of conventional LEDs. A reduction in threading dislocations of the epitaxial films also improved the electrical properties of the PSS LEDs. In Figure 2.22, TPSS exhibited the highest EL intensities amongst the different samples due the increase in internal reflection within the LED. As a result, the light extraction efficiency was improved through light scattering over a wider range. This implied that the shape of the pattern had an effect on the light extraction of LEDs. Moreover, as the fill factor of the patterns increased, the light extraction efficiency of LEDs saw an improvement.

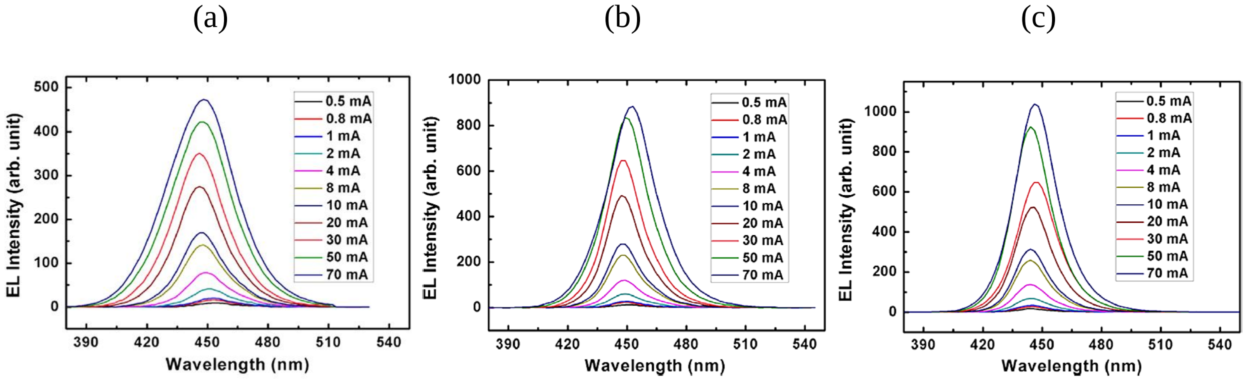

Figure 2.22 EL spectra of (a) conventional, (b) HPSS and (c) TPSS LEDs [17]

The literatures reviewed showed that introducing PSS of any geometry enhanced the light output performance of the LEDs over the use of conventional flat polished sapphire substrates. The better light extraction of the PSS LEDs was a result of the increase in light scattering and a reduction in threading dislocations in the GaN epilayer on the PSS.

3 Theoretical analysis of laser beam interaction with sapphire

3.1 Linear interaction of light with sapphire wafer

To have a better understanding of light interaction with a sapphire sample, the effect of sample surface roughness is studied, in particular the orientation of the sample surface with or without roughness towards the laser light source.

According to light-material interaction theory, when light is incident on a surface with a change in refractive index of the medium, it could either be reflected on the surface or refracted within the incident medium.

The angle to which light was reflected, as indicated in Figure 3.1, is determined by Fermat's law [29]:

$$\theta_i = \theta_r \tag{3.1}$$

Where θ_i and θ_r are respectively the angle of incident light and the angle of reflected light with respect to the surface normal.

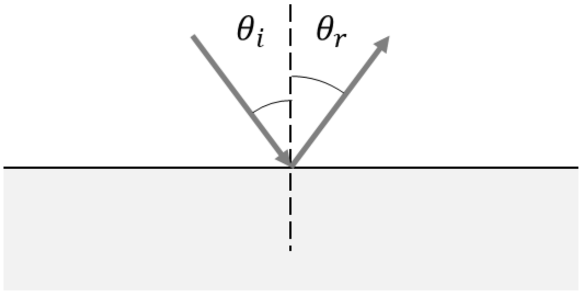

Figure 3.1 Reflection of light with a change in refractive index of medium

Light refraction indicated in Figure 3.2 can be described by Snell's law [30]:

$$n_1 \sin \theta_1 = n_2 \sin \theta_2 \tag{3.2}$$

Where n is the refractive index of a material and θ is the angle of light with respect to the surface normal, with the subscripts 1 and 2 denoting materials 1 and 2 respectively.

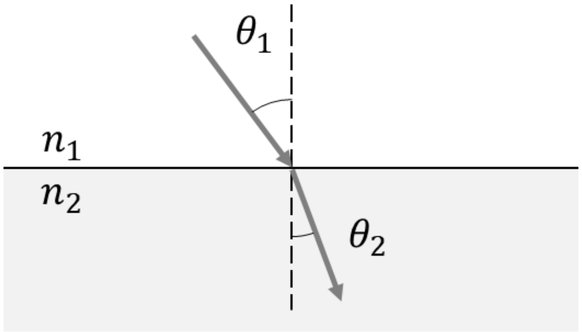

Figure 3.2 Refraction of light with a change in refractive index of medium

As light travels from a medium of lower refractive index to a medium of higher refractive index ($n_1 < n_2$), $\theta_1 > \theta_2$ as the light beam is refracted towards the normal. The reverse is true when light travels from a medium of a higher refractive index to a lower index ($n_1 > n_2$), light will be refracted away from the normal ($\theta_1 < \theta_2$).

The angle of incident resulting in a 90° angle of refraction is the critical incident angle. Any incident angle larger than the critical angle, the light will not exit the incident medium. Instead of being transmitted, the light will be reflected within the medium according to Fermat's law. This phenomenon is known as internal reflection and it can only occur for light travelling from a medium of higher refractive index to a lower index ($n_1 > n_2$) [29].

This critical angle may be determined using Snell's law:

$$\theta_c = \sin^{-1}\frac{n_2}{n_1} \tag{3.3}$$

Where θ_c is the critical angle.

An illustration of the critical angle and internal reflection is presented in Figure 3.3.

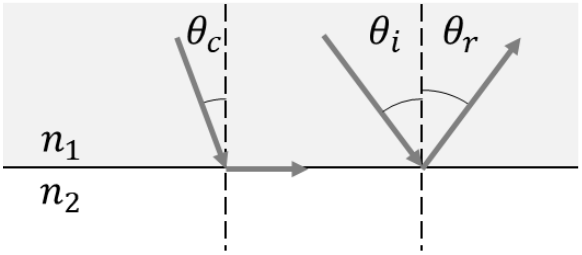

Figure 3.3 Critical angle and internal reflection

To determine the surface roughness effect on light transmission, three different orientations of the sapphire samples were tested, see Figure 3.4. The first was a double side polished sample. The second was a single side polished sample with light incident on the unpolished (rough) surface. The last was a single side polished sample with light incident on the polished surface.

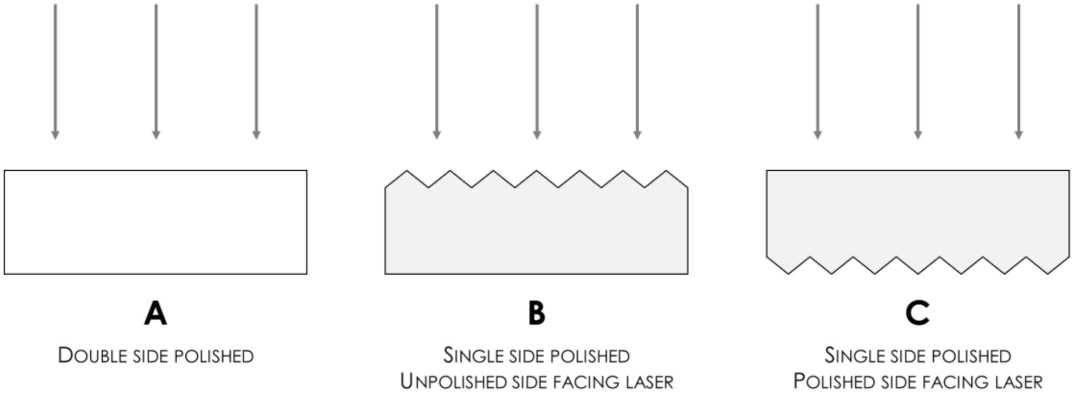

Figure 3.4 Sapphire samples used in the experiment with their respective orientations

The angle of incidence on a polished surface is well defined. Light will either be reflected or refracted at the polished surface if the critical angle is not exceeded for the incident laser light on the sample surface. This is the case for laser-sapphire sample interaction in this investigation as the focused laser beam has an incident angle close to 0°.

Interaction between light and an unpolished surface is more complicated as the incident angle is not well defined due to the surface roughness. The orientation of a sample with an unpolished surface either as the entry surface facing the incident light or the exit surface will have an effect on the amount of light transmitted, reflected and absorbed by the sample. This is because with a rough surface, a light beam's angle of incidence to either the entry or the exit surface of a sapphire sample will be distorted by the surface roughness.

The divergence angle is an important factor to determine if the light beam will emerge from the exit surface, and if so, at what angle. A focused laser beam is parabolic, i.e. the beam converges at the focal plane to form the beam waist, which then diverges shortly after, see Figure 3.5 [31].

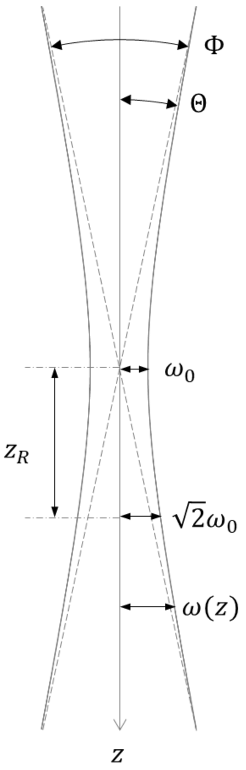

Figure 3.5 Illustration of focused beam

The focused spot diameter, twice the beam waist radius, for the focus at diffractive order 0 can be obtained as [31]:

$$\phi = 2\omega_0 = \frac{4M^2 f\lambda}{\pi D} \tag{3.4}$$

Where ϕ is the focused spot diameter, ω_0 is the beam waist radius, M^2 is the beam quality factor, f is the effective focal length, λ is the laser wavelength, D is the unfocused beam diameter (before the focusing lens).

As such, the divergence half angle can be calculated [31]:

$$\Theta = \frac{\Phi}{2} = \frac{\lambda}{\pi\omega_0} \tag{3.5}$$

Where Θ is the divergence half angle and Φ is the divergence angle.

For example, for a focusing lens with $f = 4.38$ mm (the smallest EFL employed with the largest divergence angle), and a laser with $M^2 = 1.3$, $\lambda = 1064$ nm and $D = 6.5$ mm, the focused spot diameter can be calculated:

$$\phi = \frac{4 \cdot 1.3 \cdot 4.38 \times 10^{-3} \cdot 1064 \times 10^{-9}}{\pi \cdot 6.5 \times 10^{-3}} \tag{3.6}$$

$$= 1.19 \times 10^{-6}\, m$$

$$= 1.19\, \mu m$$

The divergence half angle can be calculated:

$$\Theta = \frac{1064 \times 10^{-9}}{\pi \cdot (1.19 \times 10^{-6})/2} \tag{3.7}$$

$$= 32.7°$$

The critical angle for a sapphire sample can also be calculated:

$$\theta_c = \sin^{-1}\frac{n_s}{n_a} \tag{3.8}$$

$$= \sin^{-1}\frac{1.768}{1}$$

$$= 34.4°$$

Where n_s and n_a are the refractive index of sapphire and air respectively.

For Sample A with both surfaces polished, most of the light beams would be refracted on the polished top surface towards the normal. Light then transmits through the sample and emerges from the bottom surface by refracting away from the normal a second time, as it was travelling from a medium of a higher refractive index to a lower one. If light is incident perpendicularly to the sapphire sample surface (i.e. incident angle = 0°), it will not undergo refraction and will continue in its original propagation direction within the sample. Transmission will account for most of the light incident on the sapphire sample, with a small portion of incident light reflected by the shiny polished surface [30]. Figure 3.6 presents an illustration of light interaction with Sample A. Subscripts 1 and 2 denote the entry and exit surfaces respectively and subscripts i and r denote the incident and refracted rays respectively, unless otherwise stated. In some cases, subscript r is used to denote the reflected ray when internal reflection occurs.

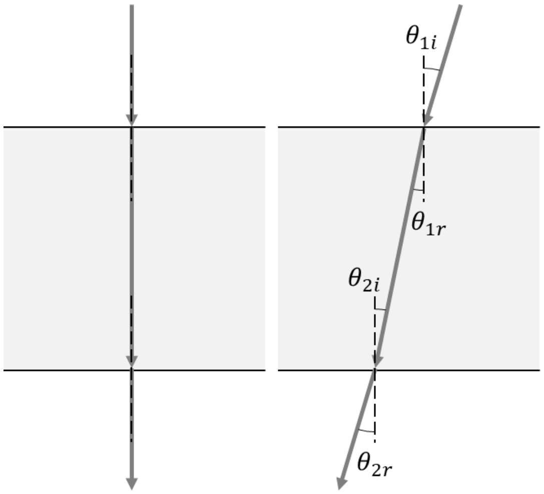

(a) (b)

Figure 3.6 Illustration of light interaction with Sample A
(a) light passes straight through as θ_{1i} *= 0° and (b) light gets refracted as* $0° < \theta_{1i} < 90°$

The relations between the angles in Figure 3.6 are as follows:

$$\theta_{1i} = \theta_{2r} = \Theta \tag{3.9}$$

$$\theta_{1r} = \theta_{2i} \tag{3.10}$$

Unless θ_{1i} makes an angle of incidence of more than 90° (not possible), θ_{2i} would not exceed θ_c (= 34.4°) and internal reflection will not occur.

For example, from first principles,

$$\Theta = \theta_{1\mathrm{i}} = 32.7° \tag{3.11}$$

$$\begin{aligned}\theta_{1r} &= \sin^{-1}\left(\frac{n_a}{n_s}\sin\theta_{1i}\right) \\ &= \sin^{-1}\left(\frac{1}{1.768}\sin 32.7°\right) \\ &= 17.8° = \theta_{2i}\end{aligned} \tag{3.12}$$

$$\begin{aligned}\theta_{2r} &= \sin^{-1}\left(\frac{n_s}{n_a}\sin\theta_{2i}\right) \\ &= \sin^{-1}\left(\frac{1.768}{1}\sin 17.8°\right) \\ &= 32.7° = \theta_{1i} = \Theta\end{aligned} \tag{3.13}$$

For Sample *B*, some of the light incident on the unpolished top surface diffuses at the top surface. Most light, however, will be refracted towards the normal and into the material. Since the bottom surface is polished as that of Sample *A*, light exits the material by refracting away from the normal. A smaller portion of light on the bottom surface that has an angle of incidence greater than the critical angle of 34.4° will be reflected at that surface according to the principle of internal reflection. In addition, as the rough surface has a larger “effective” surface area as compared to a smooth surface, a relatively larger portion of light incident on the rough entry surface will be diffusely reflected and do not enter the sapphire, resulting in a smaller portion of light transmitted through the sample. An idealization of plane of surface roughness is presented in Figure 3.7 which illustrates light interaction with Simple B. α denotes the plane of surface roughness with respect to the reference polished surface.

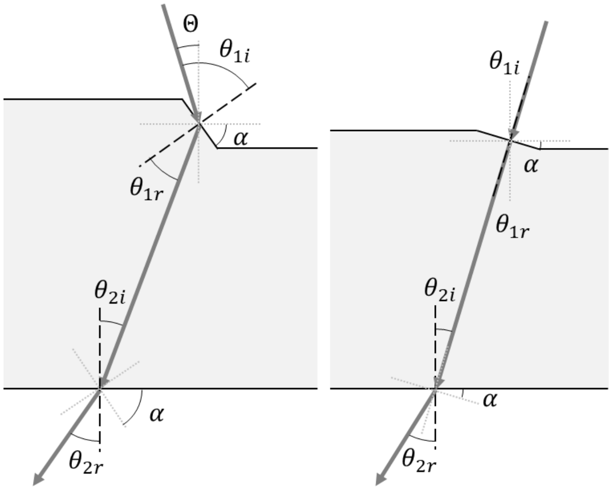

(a) (b)

Figure 3.7 Illustration of light interaction with Sample B
(a) with angle of incidence θ_{1i} maximized (slightly below 90°) and (b) special case where angle of incidence θ_{1i} = 0°

The relations between the angles in Figure 3.7 (a) are as follows:

$$\alpha = \theta_{1i} - \Theta \tag{3.14}$$

$$\theta_{2i} = \alpha - \theta_{1r} \tag{3.15}$$

The relations between the angles in Figure 3.7 (b) are as follows:

$$\theta_{1i} = \theta_{1r} = 0 \tag{3.16}$$

$$\alpha = \Theta = \theta_{2i} \tag{3.17}$$

The other angles can be calculated using Snell's law in Equation 3.2.

For example, the angle of incidence at the entry surface θ_{1i} is set at a maximum of 90°. The angle was chosen as it gives a refracted angle of $\theta_{1r} = \theta_c = 34.4°$.

Sample calculations for the example present in Figure 3.7 (a) can be summarized as:

$$\begin{aligned} \alpha &= \theta_{1i} - \Theta \\ &= 90° - 32.7° \\ &= 57.3° \end{aligned} \tag{3.18}$$

$$\begin{aligned} \theta_{1r} &= \sin^{-1}\left(\frac{n_a}{n_s}\sin\theta_{1i}\right) \\ &= \sin^{-1}\left(\frac{1}{1.768}\sin 90°\right) \\ &= 34.4° \end{aligned} \tag{3.19}$$

$$\begin{aligned} \theta_{2i} &= \alpha - \theta_{1r} \\ &= 57.3° - 34.4° \\ &= 22.9°\ (no\ internal\ reflection) \end{aligned} \tag{3.20}$$

$$\begin{aligned} \theta_{2r} &= \sin^{-1}\left(\frac{n_s}{n_a}\sin\theta_{2i}\right) \\ &= \sin^{-1}\left(\frac{1.768}{1}\sin 22.9°\right) \\ &= 43.4° \end{aligned} \tag{3.21}$$

Similarly, for the example of Figure 3.7 (b):

$$\alpha = \theta_{2i} = \Theta = 32.7° \tag{3.22}$$

$$\theta_{2r} = \sin^{-1}\left(\frac{n_s}{n_a}\sin\theta_{2i}\right) \tag{3.23}$$

$$= \sin^{-1}\left(\frac{1.768}{1}\sin 32.7°\right)$$

$$= 72.8°$$

When light is incident on the top entry surface, Samples *A* and *B* would exhibit slightly different light interactions at the top surface; light will be refracted into the material for Sample *A*, while light will be diffused and then refracted into the material for Sample *B*. Since both samples had a polished and smooth exit surface, there will be little or no internal reflection within the material. Most of the light would be transmitted through the material. Therefore, light interaction at the bottom surface would be similar.

However, Sample *C* can be expected to exhibit rather different light-material interaction as compared to the other samples. Sample *C* has a flat and polished top surface which is similar to that of Sample *A*. Likewise, most of the light beams will be refracted on the polished top surface towards the normal into the sample. Some light will be reflected due to the shiny polished surface. In contrast to Sample *A*'s polished bottom surface, Sample *C*'s bottom surface is unpolished and rough. Incident light forms different angles of incidence with the rough exit surface with some of these angles exceeding the critical angle of 34.4°. This results in a portion of light being internally reflected into the material, while the rest is refracted and exits the sample. When these reflected light beams reached the top surface, the light beams will again reflect internally or refract out of the surface depending if the incident angle has exceeded the critical angle. Sample *C* would have the least amount of transmitted light due to a larger portion of light internally reflected within the sample as compared to Samples *A* and *B*. In addition to light reflection on the top surface, light internally reflected at the rough exit surface could be refracted out of the top entry surface. Figure 3.8 illustrates light interaction with Sample *C*.

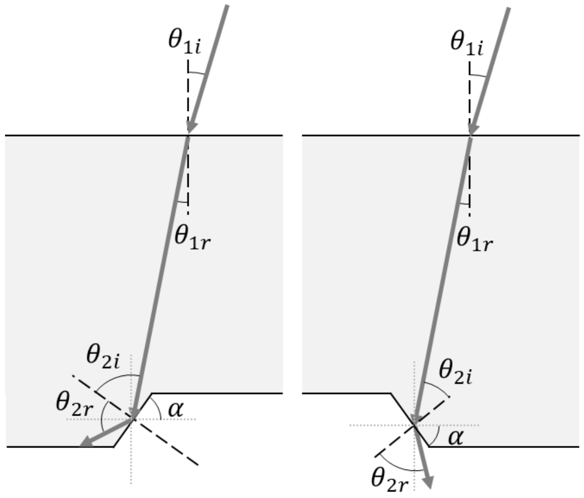

(a) (b)

Figure 3.8 Illustration of light interaction with Sample C
(a) where $0° \leq \alpha \leq 90°$*. In this case,* θ_{2r} *is internally reflected within the sample and*
(b) where $-90° \leq \alpha \leq 0°$*. In this case,* θ_{2r} *is refracted out of the sample*

The angles of the sapphire surfaces to produce the critical angle at the rough exit surface in Figure 3.8 are as follows:

$$(a)\ \alpha = \theta_c - \theta_{1r} \tag{3.24}$$

$$(b)\ \alpha = \theta_c + \theta_{1r} \tag{3.25}$$

Since $\Theta = 32.7°$, $\theta_{1r} = 17.8°$ from 3.7 and Equations 3.1. The α to reach critical angle for these cases are:

$$\begin{aligned}(a)\ \alpha &= 34.4° - 17.8° \\ &= 16.6°\ (clockwise)\end{aligned} \tag{3.26}$$

$$(a)\ \alpha = 34.4° + 17.8° \tag{3.27}$$

$$= 52.2°\ (counter\ clockwise)$$

Do note that these are with reference to the divergence half angle and plane of surface roughness as defined by the angle α with respect to the reference polished surface as shown in Figure 3.9.

Figure 3.10 presents θ_{2r} calculated against the change of α, when $\Theta = 0°$. The sudden change in θ_{2r} values indicates that there is a change in light interaction at the exit surface, from internally reflected (dotted) to refracted out of the sample (solid). Since Sample *A* is a double side polished sample, the entry and exit surfaces are parallel to one another. Hence, there is no change in α, and θ_{2r} is kept constant at 0°. Samples *B* and *C* exhibit both internal reflection and refraction. Since as $\Theta = 0°$, the incident ray is perpendicular to the reference polished surface. Changing α from negative to positive values will produce the same θ_{2r}, therefore the graphs are symmetrical. From the distribution of the graphs, it appears that Sample *C* exhibits a greater possibility of internal reflection compared to Sample *B*.

Figure 3.11 presents θ_{2r} calculated against the change of α, when $\Theta = 32.7°$ (the largest EFL employed). Likewise, the sudden change in θ_{2r} values indicates that there is a change in light interaction at the exit surface, from internally reflected (dotted) to refracted out of the sample (solid). For Sample *A*, there is no internal reflection as discussed previously and θ_{2r} is constant at 32.7°. Samples *B* and *C* exhibit both internal reflection and refraction. The curves found in the refraction graphs are due to the change in refractive index from sapphire to air. For Sample *B*, from -32.7° $< \alpha <$ 32.7°, the change in shape of the graph and the lack of symmetry is a result of having a divergence half angle of 32.7°. Sample *B* has a greater possibility of internal reflection when $\Theta = 32.7°$ (in Figure 3.11) compared to when $\Theta = 0°$ (in Figure 3.10) .Whereas for Sample *C*, the shape of the graph does not change from Figure 3.10. However, the graph has shifted to the right by $\theta_{1r} = 17.8°$. This indicates that changing Θ does not change the probability of internal reflection in Sample *C*, it only changes the range of values for internal reflection to occur.

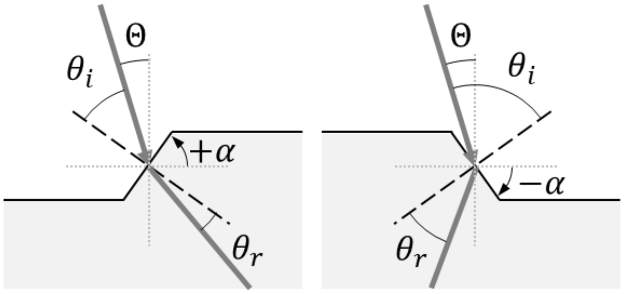

(a) (b)

Figure 3.9 Schematic for definitions of α and divergence half angle θ
(a) where $0° \leq \alpha \leq 90°$ (clockwise: positive α) and (b) $-90 \leq \alpha \leq 0°$ (counter clockwise: negative α)

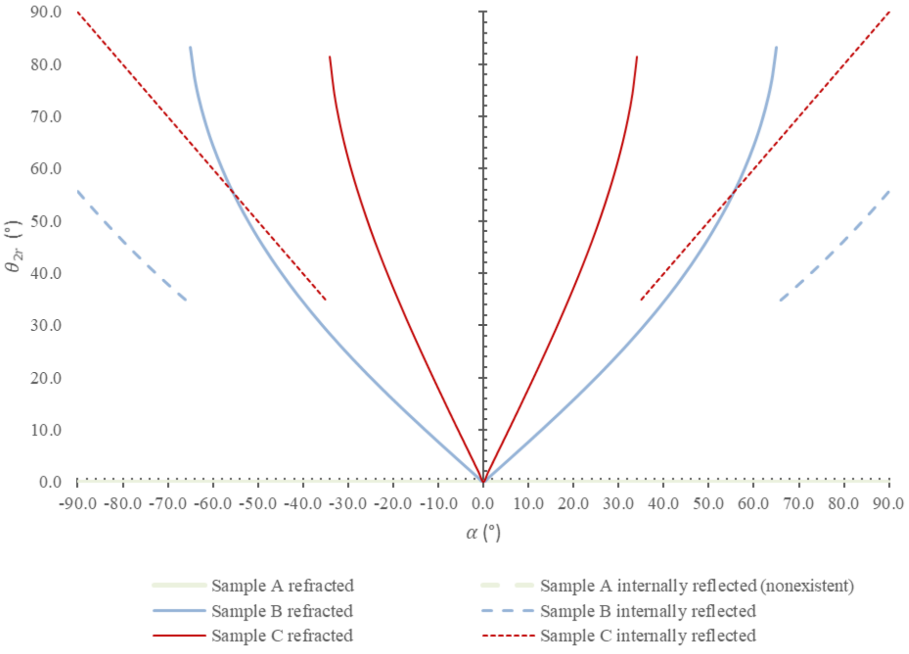

Figure 3.10 Graph of θ_{2r}, at the exit surface, against α, where $\Theta = 0°$

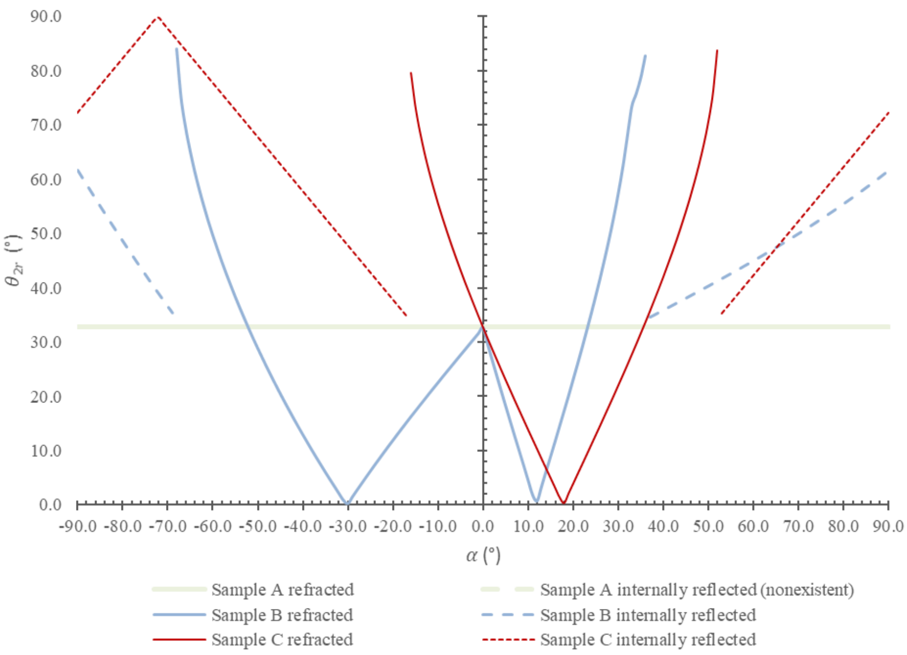

Figure 3.11 Graph of θ_{2r}*, at the exit surface, against* α*, where* $\Theta = 32.7°$

In summary, the interaction between the laser beam and the exit surface can be determined through Figure 3.12 for the various samples' surface morphologies, and that α will dictate if light will be internally reflected within or transmitted through the sample. These analyses indicate that Sample C could be a better choice for laser machining as more light could be trapped within the sample with the aid of internal reflection at the rough exit surface than the other samples. This would result in more energy to be absorbed by the material for machining purpose.

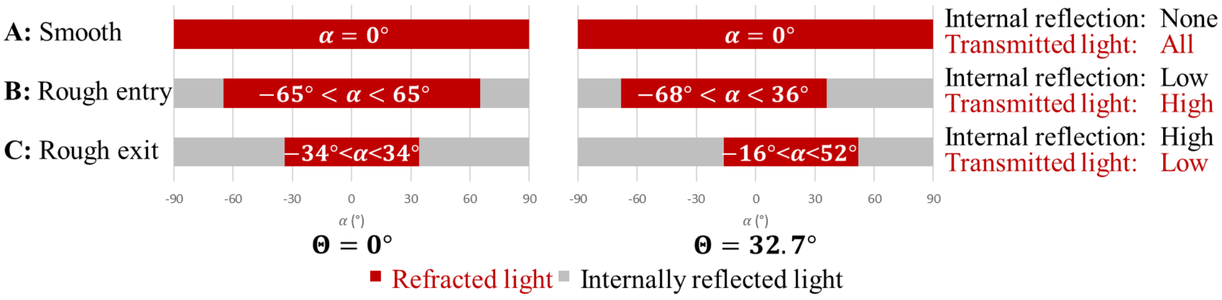

Figure 3.12 Laser beam interaction at the exit surface for the various samples, where $\Theta = 0°$ *or* $32.7°$

3.2 Nonlinear interaction of light with sapphire wafer

The linear interaction of light with sapphire alone is insufficient for weakening the bonds within sapphire. Nonlinear absorption within the transparent sapphire is required to modify the material. Ultrashort pulse lasers, such as lasers working in the picosecond regime, are capable of producing extremely high peak power density that induce nonlinear absorption within the material through multiphoton excitation.

A laser with a wavelength of 1064 nm can only produce a single photon with an energy of 1.17 eV [32], [33]. Since sapphire has a band gap energy of 9.9 eV, the energy of the single photon is insufficient to overcome the band gap between the valence band to the conduction band. For a laser with a wavelength of 1064 nm, a minimum of nine photons are needed to overcome the band gap between the valence band to the conduction band. Hence, a nine-photon absorption (9PA) process is required for nonlinear absorption to occur within the material [34].

However, the theory behind nonlinear absorption mechanisms is complicated. The effects of nonlinear absorption will be investigated and discussed through experiments in Section 5.3.

4 Methodology

4.1 Sapphire wafer

4.1.1 Sapphire wafer characteristics

The sapphire wafers supplied by Latech Scientific Supply Pte. Ltd. (Singapore) had a diameter of 50.8 mm with a thickness of 0.43 mm. The single crystal Al_2O_3 sapphire wafers had a c-plane crystal orientation of <0001> with a hexagonal crystalline structure and a crystal hardness of 9 Mohs [35]. The wafers were either double side polished or single side polished.

Sapphire exhibits birefringence and has an ordinary refractive index of n_o = 1.768 and an extraordinary refractive index of n_e = 1.760. The band gap energy of sapphire is 9.9 eV. The wafers have a tensile strength of 400 MPa and a flexural strength of 3.5 GPa (X. Lu, Latech Scientific Supply Pte. Ltd., private communication, Feb. 2019). The wafers have a thermal expansion coefficient of 7.5×10^{-6} /°C, a thermal conductivity of 12.56 W/mK at 400 °C, a dielectric constant of 11.58 and a melting point of 2040 °C [35].

4.1.2 Wafer surface roughness measurements

Two types of sapphire samples were used, namely double side polished samples or single side polished samples with the other side unpolished.

To have an appreciation of the surface roughness uniformity, and if the surface roughness depends on the orientation of sapphire surface, the surface roughness of the samples was measured using a stylus profilometer Form Talysurf Series 2 by Taylor Hobson. For roughness measurement, the stylus travelled a 10 mm line at the center of the wafer. Each sample surface was measured 12 times in two directions (6 times in each direction), namely 0° and 90° respectively, as shown in Figure 4.1. Two types of surface roughness readings were registered, Ra and Rz. Ra refers to the roughness average, while Rz is the difference between the highest peak and the lowest valley.

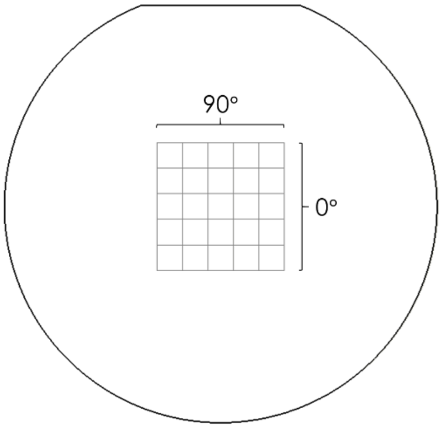

Figure 4.1 Illustration of stylus scribes on sapphire wafer (not to scale)

4.1.3 Sapphire wafer optical properties measurements

A PerkinElmer Lambda 1050 UV/Vis/NIR Spectrometer was employed to characterize the optical properties of the sapphire samples. Due to the difference in surface finish, the orientations of the (polished and/or unpolished) surfaces facing the incident light in the spectrometer were considered. Three different orientations of sapphire wafers to be tested are illustrated in Figure 3.4 of Chapter 3. As such, the effect of surface morphology on the optical property of sapphire can be determined. A baseline reading of the spectrometer was taken to ensure proper calibration. Optical transmittance and reflectance of the samples were subsequently taken for wavelengths ranging from 300 nm to 1200 nm, with an interval of 5 nm.

4.2 Singulation method

4.2.1 Laser system

A picosecond $Nd:YAG$ laser by Time-Bandwidth Products AG (Zurich, Switzerland), with vertical linear polarization, was used in this investigation. The laser has a laser wavelength of 1064 nm, a pulse width of 10.3 ps, a beam diameter of 6.5 mm, and an M^2 value of 1.3.

The laser is equipped with a galvo scanner which has an effective focal length (EFL) of 100 mm, making the focused spot diameter at the focal length to be 27.1 μm. The laser system also allows the insertion of a customized lens fixture for more complex applications.

The sapphire wafers were irradiated with various laser parameters and multiple foci conditions. The laser parameters investigated were the scanning height, scanning speed, pulse repetition rate and power levels.

4.2.2 Nonlinear absorption power measurements

A PowerMax PM30 power sensor with a FieldMaxII-TO laser power meter from Coherent, Inc. (California, United States) was used to measure the defocused laser power of a single focus with and without the sapphire samples. Measuring the laser power at the focal point will burn and damage the power meter. Figure 4.2 shows the setup with a sapphire sample. A flat top beam shaper was employed to facilitate the analysis of the power measured. The reference height z was placed at the top surface of the sapphire sample. For example, when the focal position was placed at the bottom surface of the sample, z = +430 μm.

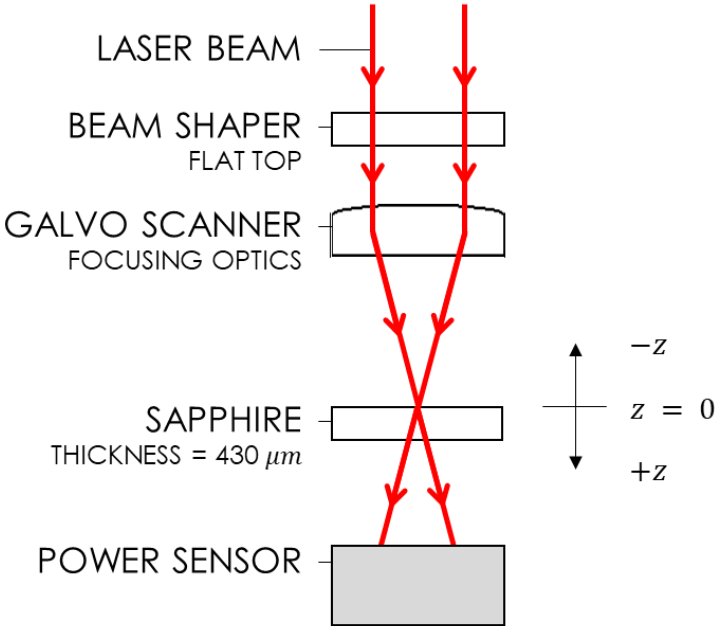

Figure 4.2 Schematic of nonlinear absorption power measurement setup

Each data point was measured with and without the sapphire sample. This procedure will minimize error introduced by fluctuation of laser power in-between each experiment, if any.

4.2.3 Multifocal optics setup

A multifocal (MF) lens accompanied with a focusing optic was employed for the laser experiments. The MF lens belongs to a type of diffractive optical element (DOE) [36]. The laser beam was focused by either a focusing lens or an objective lens. The focusing lenses were categorized by their EFL; the objective lenses were categorized by their magnifications with a prefix OB followed by their magnification. Optical elements employed in the experiments are listed in Table 4.1. Figure 4.3 shows an illustration of the MF lens of a binary design, with the elevated grooves acted as a grating (J. Fantl, HOLO/OR Ltd., private communication, Apr. 2019). The elevated grooves in Figure 4.3 have been exaggerated in height for ease of visualization.

Table 4.1 List of multifocal lenses, focusing lenses and objective lenses used

Multifocal lens	**Focusing lens**	**Objective lens**
9 foci (HOLO/OR)	7.5 mm (Edmund Optics)	OB10× (Meiji Techno)
27 foci (HOLO/OR)	12.0 mm (Edmund Optics)	OB20× (Meiji Techno)
		OB40× (Meiji Techno)

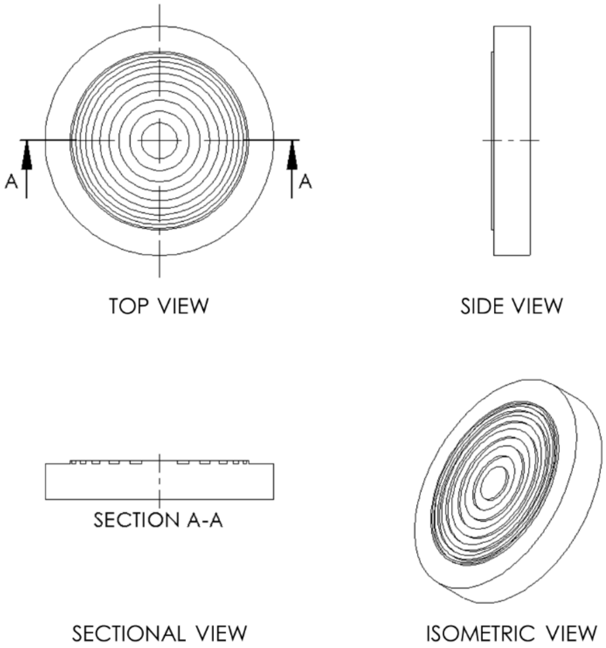

Figure 4.3 Illustration of multifocal lens (not drawn to scale)

The MF lens together with a focusing or objectives lens were mounted on a custom-made fixture that can be attached to the laser machine, see Figure 4.4. The laser beam entered from the top of the fixture and interacted with the work piece at the bottom as shown in Figure 4.5. The role of the MF lens was to change the phase of the incoming laser beam without changing the direction of light propagation. Therefore, the exact distance between the MF lens and the focusing lens is not a critical consideration. Refraction only occurred at the focusing lens, with the multiple foci focused at the designed focal lengths.

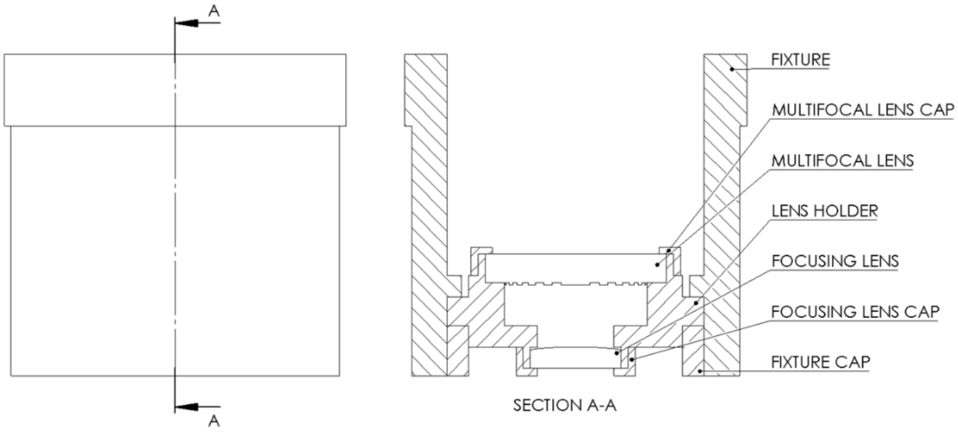

Figure 4.4 Lens fixture for usage with laser machine

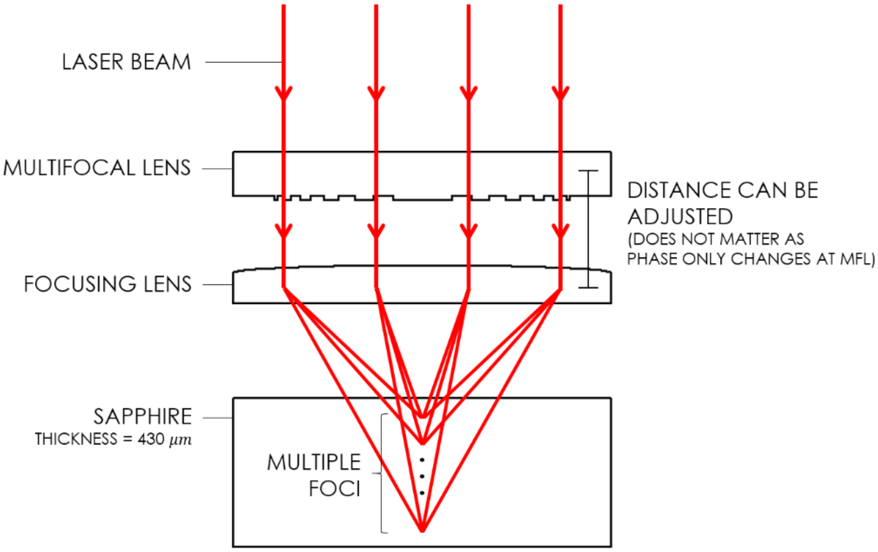

Figure 4.5 Schematic of multiple focus in sapphire

Each of the foci had a particular diffractive order depending on its relative position with respect to the focal length of the focusing lens. Figure 4.6 shows an illustration on the diffractive orders and their assignment to the foci. This illustration depicts 7 foci, but more foci are possible. The focus at the focusing lens' focal length was given the diffractive order of 0. Foci closer to the incident beam were given positive values, while foci further away were given negative values.

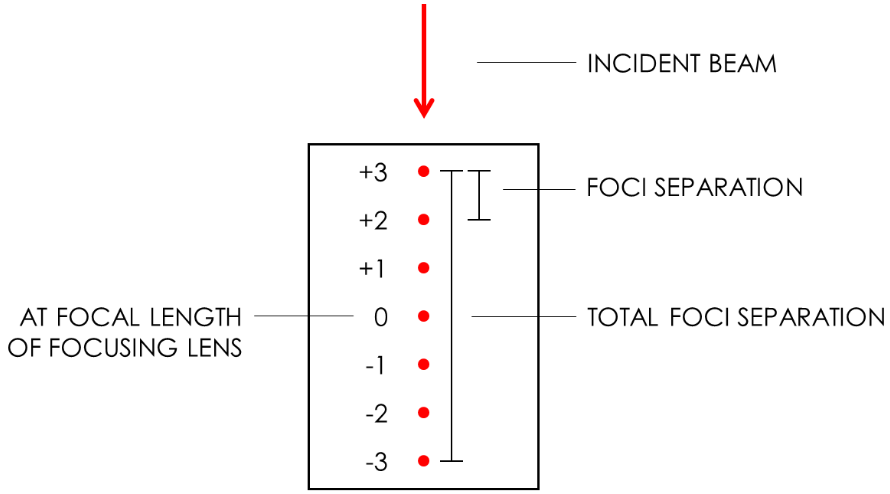

Figure 4.6 Diffractive orders for 7 multiple foci

The location of each individual focus can be approximated using the equation provided by the MF lens supplier HOLO/OR Ltd. [37].

$$\frac{1}{f_m} = \frac{1}{f_R} + \frac{m}{f_D} \qquad m = \pm 1, \pm 2, \pm 3 \tag{4.1}$$

Where f_m is the focal length of diffractive order m, f_R is the focal length of focusing (refractive) lens, and f_D is the focal length of multifocal (diffractive) lens. Focal length values are absolute values measured from the principal plane of the focusing lens. When $m = 0$, $f_m = f_R$.

Equation 4.1 is only valid for a refractive index of 1, i.e. with air as the medium. For refractive index other than 1, e.g. for sapphire as the medium with a refractive index $n = 1.76$, a simplified equation to account for the refractive index may be employed [29]:

$$f_{m,n} = nf_m \tag{4.2}$$

Where $f_{m,n}$ is the focal length of diffractive order m in a medium of refractive index n.

For a conventional focusing lens, the largest portion of power is concentrated at the center of focus, and power decreases slowly away from the focus. As such, one might intuitively assume that the largest portion of power is focused at diffractive order 0 and the power slowly decreases for foci located further away. However, this is not the case for a DOE MF lens. In contrast, the laser power is evenly distributed between the foci due to the nature of the DOE (J. Fantl, HOLO/OR Ltd., private communication, Apr. 2019).

4.2.3.1 Combinations of multifocal and focusing optics

As explained in Section 4.2.3, the separation distance between foci depends on the type of MF lens, the corresponding EFL of the focusing optic, and the refractive index of the material. For sapphire which has a refractive index of 1.768, the foci separation and total foci separation (see Figure 4.6 for definition) for different MF and focusing optic combinations are presented in Table 4.2.

In practice, the foci were not equally spaced out [36]. For ease of understanding, it was assumed that on average, the foci separation was constant. The length occupied by the maximum number of foci within the sample was estimated by multiplying the average foci separation and the total number of separations between the foci focused in the sample. Through this estimation, it appeared that the 27 foci MF lens with the OB10× lens could only have a maximum of four foci focused within the sample instead of the stated five foci. Since the foci separation was not constant, it was possible to focus five foci within the sample. For example, the total foci separation between diffractive orders +9 to +13 (foci that were closest to the laser source) was 408.8 μm. Since the length of the total foci separation between the foci was shorter than the sample's thickness, focusing a maximum of five foci simultaneously within the sample was possible. The actual separation distance between these foci are tabulated in Appendix I.

Table 4.2 Foci separations for combinations of MF and focusing optics

MF optic	**EFL of focusing optic (mm)**	**Average foci separation (μm)**	**Total foci separation (μm)**	**Max no. of foci within sample**
27 foci	20 (OB10×)	109.4	2844.6	5
27 foci	10 (OB20×)	27.3	710.3	16
27 foci	4.38 (OB40×)	5.2	136.3	27
27 foci	7.5	15.4	399.5	27
9 foci	12	43.6	348.9	9
9 foci	7.5	17.0	136.3	9

With different number of foci focused within the samples, the power level of the laser had to be adjusted accordingly such that the laser energy deposited within the samples will be consistent for an unbiased comparison between results.

4.2.3.2 Multifocal and focusing optics power measurements

PowerMax PM30 power sensor with a FieldMaxII-TO laser power meter from Coherent, Inc. (California, United States) was employed to measure the amount of laser power available after passing through the MF and focusing optics, see Figure 4.7.

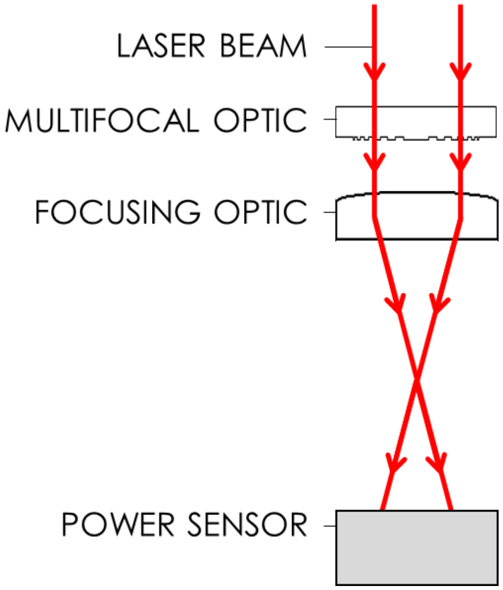

Figure 4.7 Schematic of MF and focusing optics power measurement setup

Due to the different EFL for the focusing optics, the corresponding depth of focus (DOF) will change accordingly. If the beam spot was larger than the power sensor, the measurement of the laser power after the optics will be underestimated. Hence, some adjustments to the height of the power sensor was needed to ensure that the defocused beam spot was entirely captured by the power sensor.

4.2.3.3 Multiple foci laser scanning with objective lenses of various effective focal lengths

In this investigation, a 27 foci MF lens was paired with objective lenses of different magnifications and hence different EFLs. Since a 27 foci MF lens was used, the first and the last foci had diffractive orders of +13 and –13 respectively. The first scan (Scan 1) was with diffractive order –13 at z = 0 μm. The scanning height was changed for each subsequent scan, known as the step size and was denoted by Δz. The last scan (Scan N) was with diffractive order +13 around

z = +430 μm, depending on the step size. The schematic for the changing of laser scanning height for each scan line is depicted in Figure 4.8. The foci separation between adjacent foci was not drawn to scale and it should be noted that the separation is a function of the EFL of the objective lens.

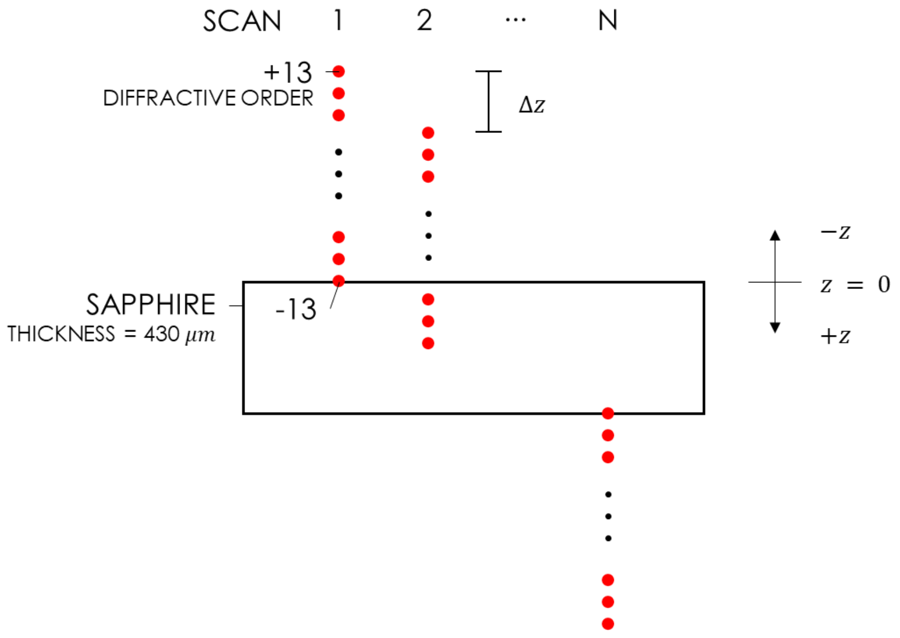

Figure 4.8 Schematic of scanning with the combination of 27 foci MF and various objective lenses at different scanning heights

The step size was determined by taking into consideration the average foci separation and the thickness of the sample. The step size and the foci separation were not multiples of each other. This allowed for the investigation of the effects of proximity of the focus to the respective surfaces on the presence of scribe formation. The respective parameters for each experiment are presented in Table 4.3.

Table 4.3 Parameters for experiments with the combination of 27 foci MF and various objective lenses

Objective lens	**EFL (mm)**	**Average foci separation (μm)**	**Step size (μm)**
OB10×	20	109.4	200
OB20×	10	27.3	50
OB40×	4.38	5.2	20

4.2.3.4 Sectional laser scanning

The 27 foci MF lens was paired with the OB40× lens. The OB40× lens was chosen as it had a total foci separation that was much shorter than the thickness of the sample (i.e. 136.3 μm and 430 μm respectively). Since the total foci separation was approximately one-third of the sample's thickness, each experiment was conducted individually at one of the three scanning sections with a single pass, see Figure 4.9. The vertical red line represents that all 27 foci were contained within that section, with diffractive order 0 located at the middle of the vertical red line. The indicated z values for each scanning section represent the positions where diffractive order 0 was focused respectively.

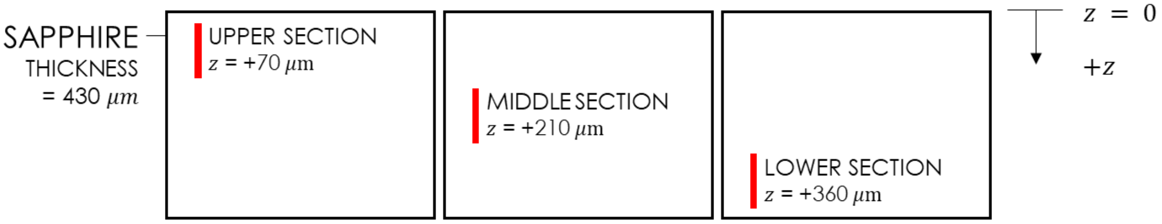

Figure 4.9 Schematic of the three scanning sections with diffractive order 0 positioned at the respective z values

4.2.3.5 Multiple foci laser scanning with conventional focusing lenses

The MF lenses with different number of foci were paired with carefully chosen conventional focusing lenses with specific EFL values to produce a total foci separation that was slightly less than the sample thickness. This is to ensure that all foci could be focused within a sample such that the laser power would be fully utilized to interact with the sample. Two sets of MF and conventional focusing lens combination were used. The first set was a 27 foci MF lens with an EFL of 7.5 mm focusing lens; the second set was a 9 foci MF lens with an EFL of 12 mm focusing lens. The resulting total foci separation of the two sets of optics were not exactly the same, see Table 4.2. Figure 4.10 depicts the difference in total foci separation for the 27 foci and 9 foci lens combinations. The vertical red line represents the length containing all the foci within that section, with diffractive order 0 located at the middle of the vertical red line. Regardless of the set of optics employed, a single scan was conducted whereby diffractive order 0 was focused at the midplane of the sample at $z = +210\ \mu$m, for a fair comparison between both sets of optics.

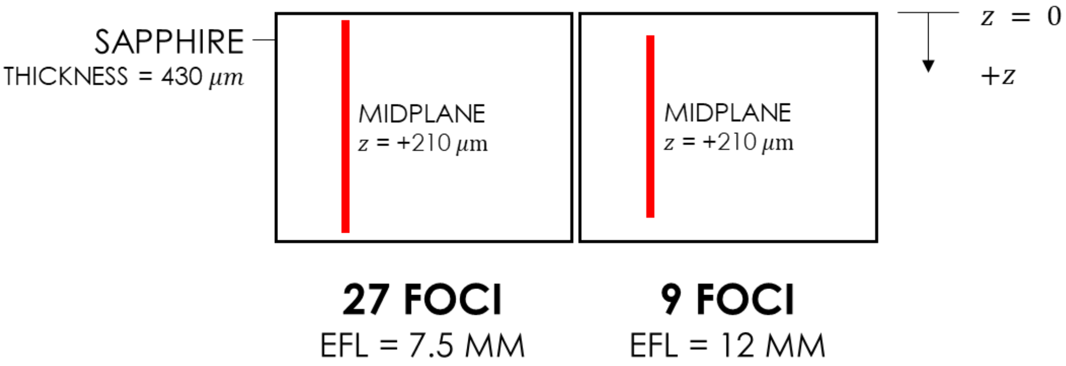

Figure 4.10 Schematic of total foci separation for different lens combinations with diffractive order 0 positioned at the respective z values

4.2.3.6 Two-zone laser scanning

The multizone experiments were conducted with a combination of a 9 foci MF lens and an EFL of 7.5 mm focusing lens. The total foci separation for the lens combination was slightly shorter than one-third of the sample's thickness, i.e. 136.3 μm out of 430 μm. This allowed a maximum of three scanning zones using the 9 foci lens combination.

When paired with an EFL of 7.5 mm focusing lens, the 9 foci setup had an average and a total foci separation of about a third of the 27 foci setup. In addition, the 27 foci setup had three times the number of foci compared to the 9 foci setup. If the same amount of power was employed, scanning the sample with the 9 foci setup at each of the three sections on the same scanning line sequentially would approximate to scanning the sample once with the 27 foci setup with diffractive order 0 focused at the sample's midplane.

Although scanning all three scanning zones one after another on the same scanning line is possible with this arrangement, each experiment was conducted with just two scanning zones. The different combinations of two-zone scanning were named as Multizone *D*, *E* and *F* accordingly and are presented in Figure 4.11. Each vertical red line represents the 9 foci contained within that section, with diffractive order 0 located at the middle of the vertical red line. Diffractive order 0 was positioned at the indicated z values for the scanning of the upper, middle and lower sections of the sample thickness respectively. Two separate scans for each specified section in the multizone would be conducted sequentially on the same scanning line. For example, Multizone *D* would require one scan for the upper section and another scan for the middle section to be conducted on the same scanning line. The order of the section to be scanned first would be determined in Section 7.2.

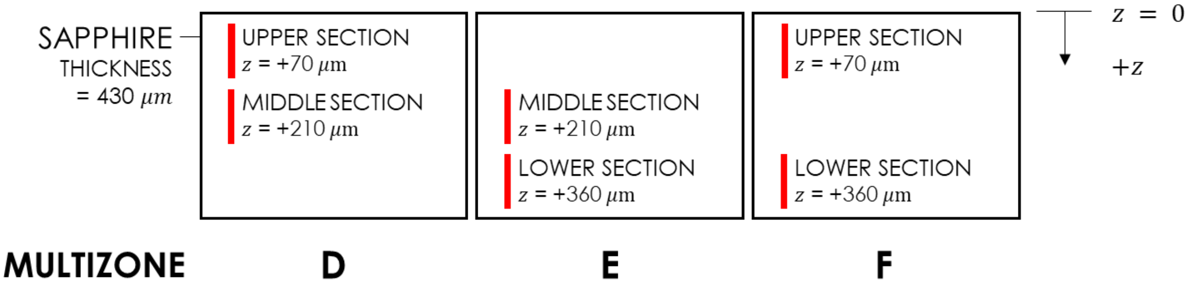

Figure 4.11 Schematic of different two-zone scanning combinations with diffractive order 0 positioned at the respective z values

4.2.4 Mechanical cleavage of sapphire samples

Mechanical cleavage by hand was carried out to observe and study the sidewall profile of the samples after multiple foci laser irradiation. Pressure was applied on the edges of the sample along the axis of a laser scribed line using two flathead screwdrivers positioned at a 45° angle to the vertical, see Figure 4.12. The small amount of pressure applied was just sufficient to induce crack propagation within the sample in the direction of laser scribing. If separation was not possible, it meant that the sample was insufficiently weakened by the laser and the sidewall profile could not be observed.

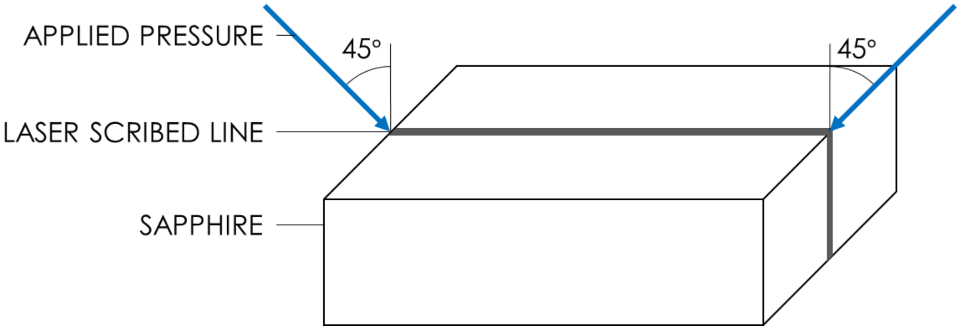

Figure 4.12 Schematic of mechanical cleavage setup

5 Effect of surface morphology on the optical properties of sapphire

The effect of surface morphology on the optical property of sapphire wafers was studied. This study aims to determine the optimal surface finish of sapphire to result in the highest level of absorbance to facilitate laser cutting of the transparent sapphire via nonlinear laser-material interaction.

5.1 Surface roughness

From Figure 5.1 and Figure 5.2, the average surface roughness of the polished surface was Ra = 1.93 nm and Rz = 9.80 nm. The average surface roughness of the unpolished surface was much higher with Ra = 0.954 μm and Rz = 6.74 μm. In addition, for both polished and unpolished surfaces, the surface roughness had no orientation effect as the roughness values obtained were independent of the direction of measurements, namely 0° and 90° respectively.

It is noted that the surface roughness of the unpolished surface was comparable to the dimensions of the geometrical patterns etched in PSS. Therefore, the unpolished surface may be considered as a representation of PSS surface. This allows the cost effective studies of laser singulation of sapphire wafers after the growth of PSS through the studies of the unpolished wafers.

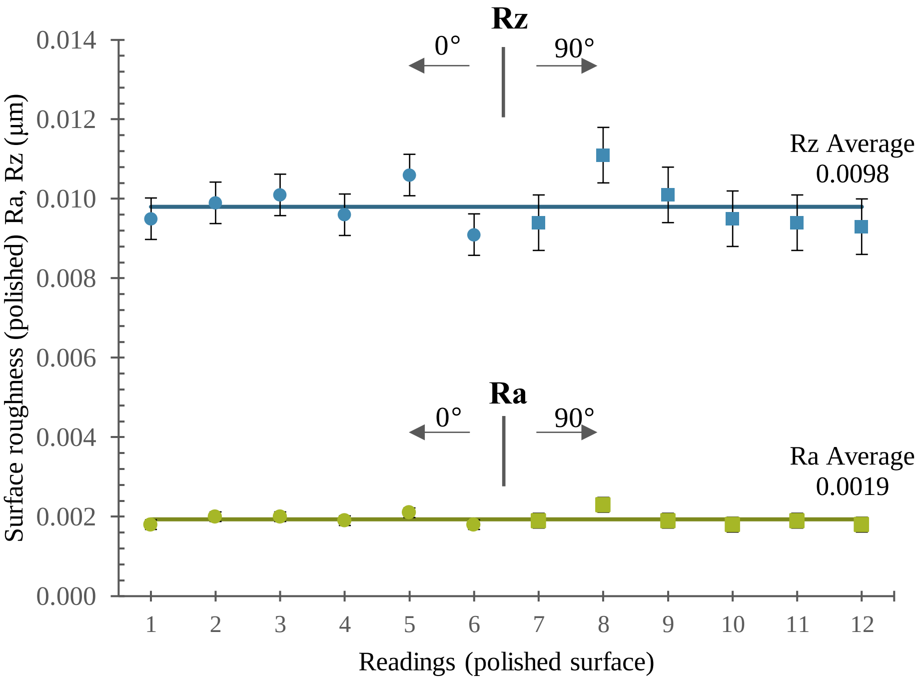

Figure 5.1 Surface roughness for a polished surface of sapphire wafer
The standard deviation for Ra is 0.00015 µm and Rz is 0.00061 µm

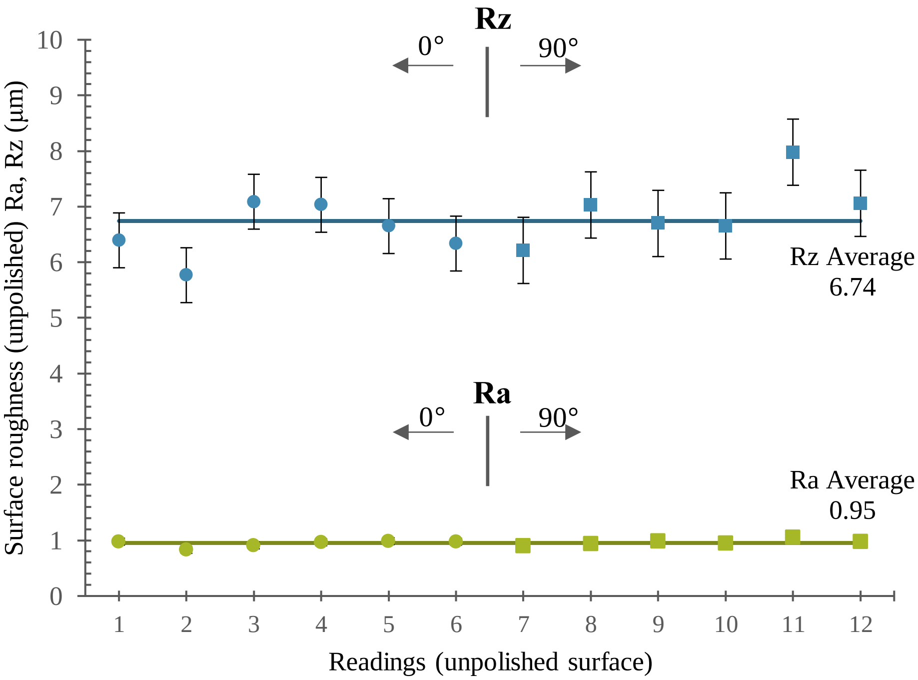

Figure 5.2 Surface roughness for an unpolished surface of sapphire wafer
The standard deviation for Ra is 0.059 µm and Rz is 0.544 µm

5.2 Linear optical properties

Each sample was placed in the spectrometer, in its particular orientation, and the readings for optical transmittance and reflectance were registered, see Figure 5.3 and Figure 5.4 respectively.

The results obtained indicated that the double side polish surface Sample *A* had the highest transmittance, followed by Sample *B* (single side polished with light incident on the unpolished surface), with Sample *C* (single side polished with light incident on the polished surface) having the lowest transmittance. The reverse order was true for the reflectance, i.e. Sample *C* had the highest reflectance followed by Sample *B* then Sample *A*. It appeared that transmittance and reflectance had an inverse relationship.

These observations are consistent with the analysis in Section 3.1. Sample *A* had the highest transmittance as both sides had smooth and flat polished surface that allowed light to pass through the sample easily. Sample *B* exhibited a slightly lower transmittance due to diffuse light reflection at the top unpolished surface. Sample *C* had the least measured transmittance. Due to internal reflection at the bottom unpolished surface, some portion of light that had an angle of incidence greater than the critical angle was reflected internally instead of being transmitted, resulting in a lower value of transmittance.

Similarly, Sample *C* had the highest reflectance due to two contributing factors. Firstly, light was reflected due to the top polished surface. Secondly, some light underwent internal reflection at the rough exit surface back to the top polished surface. Light was refracted out of the top surface when the angle of incidence was smaller than the critical angle. Sample *B* exhibited the second highest reflectance from the diffuse light reflection at the top unpolished surface. Sample *A* had the lowest reflectance due to light reflection on the top polished surface.

As shown in Figure 5.3 and Figure 5.4, it appeared that a smooth polished surface was better at light transmission, while a rough unpolished surface was better at reflecting light.

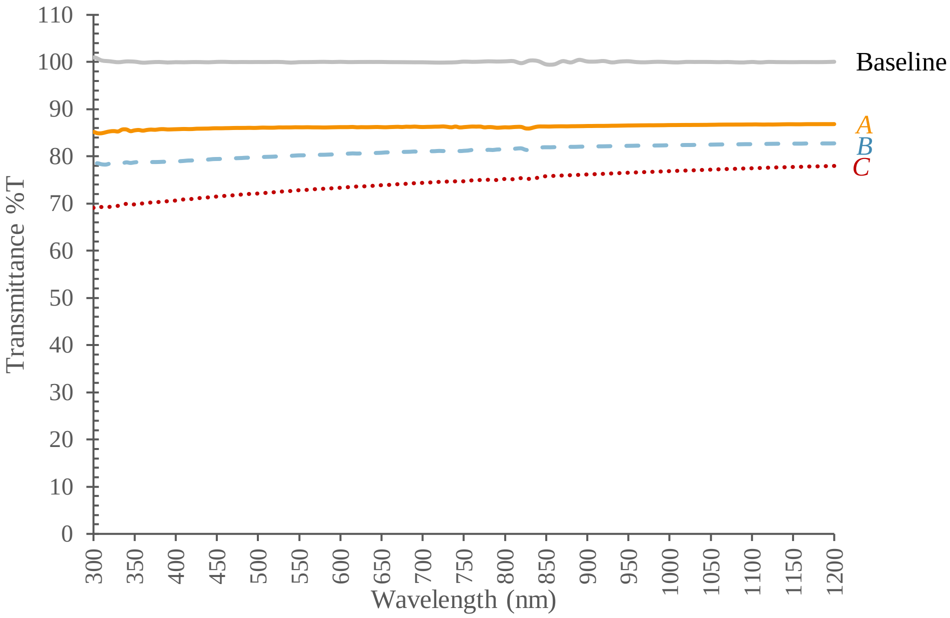

Figure 5.3 Optical transmittance of sapphire

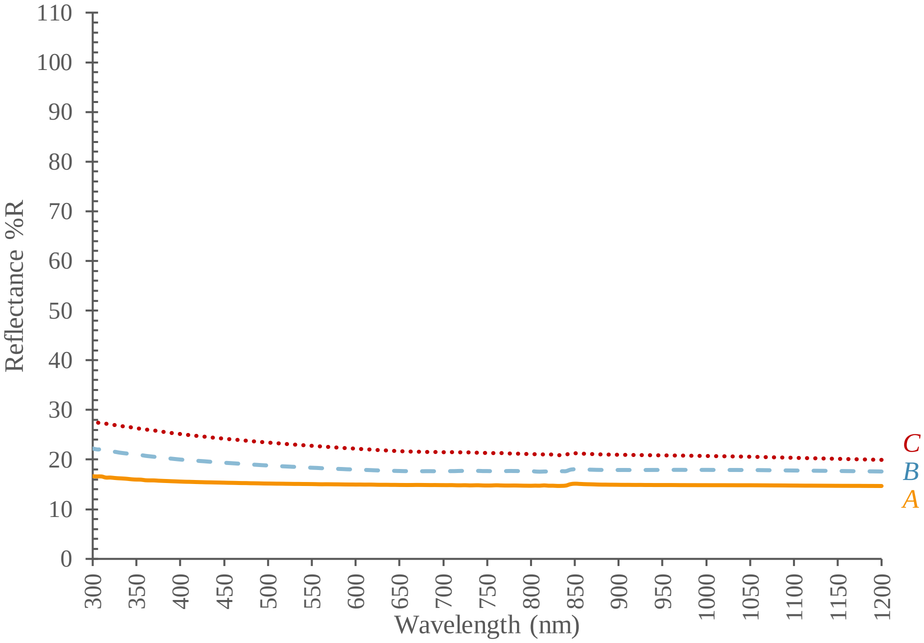

Figure 5.4 Optical reflectance of sapphire

There are three ways in which light interacts with an object; through reflection, transmission and absorption. The different modes of light interaction can be described with the conservation law [30]:

$$A + R + T = 1 \tag{5.1}$$

Where A is absorbance, R is reflectance and T is transmittance.

Since reflectance and transmittance had been obtained through experimental methods, absorbance can be calculated. The optical properties for the various sapphire samples were shown in Figures 5.5, 5.6 and 5.7 accordingly, showing similar relative distribution of light interaction. Transmittance is the highest, followed by reflectance and finally, in some cases, absorbance. However, their extent differed from sample to sample and was highly dependent on the surface morphology.

The spectrometer used light from ambient conditions and was highly sensitive to the water vapor and carbon dioxide content in the surrounding air. With low absorbance and experimental uncertainties, in some cases, the total value measured for R + T exceeded 100% thus resulting in negative values calculated for absorbance, which is physically impossible. As such, the absorbance value is set to zero, and thus only R + T values that were below 100% would have an absorption component.

From Figure 5.5, Sample *A* was observed to exhibit transmittance and reflectance only over the range of wavelengths tested. There was no or negligible absorbance component. Figure 5.6 indicates that Sample *B* demonstrated some absorbance at shorter wavelengths, i.e. from 325 nm to 900 nm. As shown in Figure 5.7, Sample *C* was observed to exhibit absorbance over the range of wavelengths tested, i.e. from 300 nm to 1200 nm. This could be the result of internal reflection allowing more light to be absorbed within the material as the path length of a light beam was increased. This resulted in a smaller portion of reflected and transmitted light.

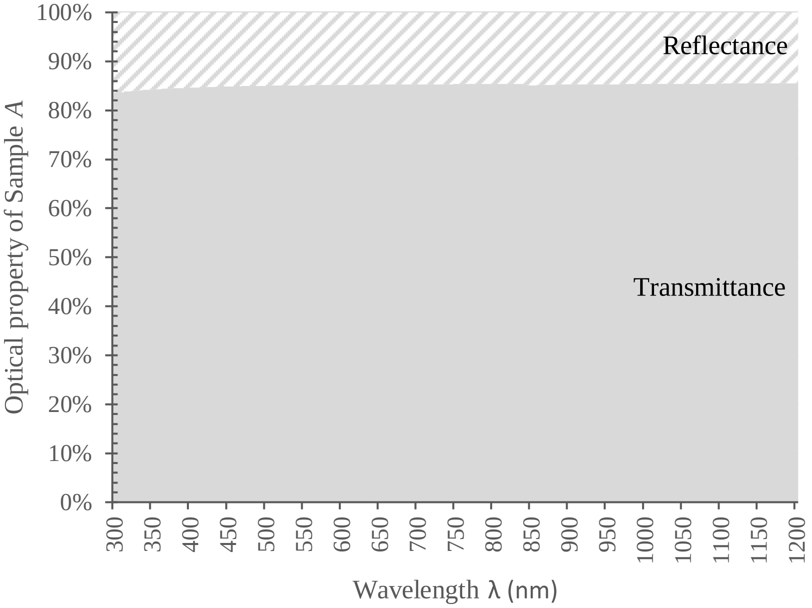

Figure 5.5 Light interaction with double side polished sapphire

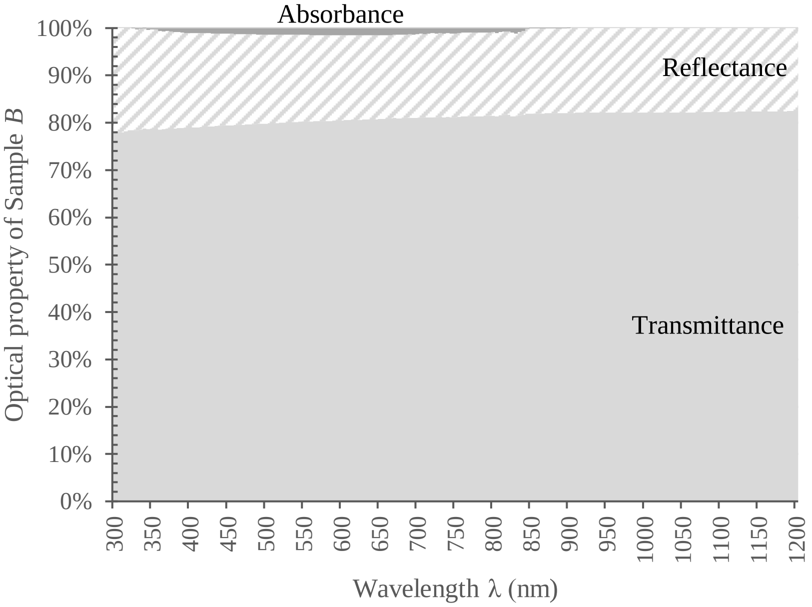

Figure 5.6 Light interaction of a single side polished sample with light incident on the unpolished surface

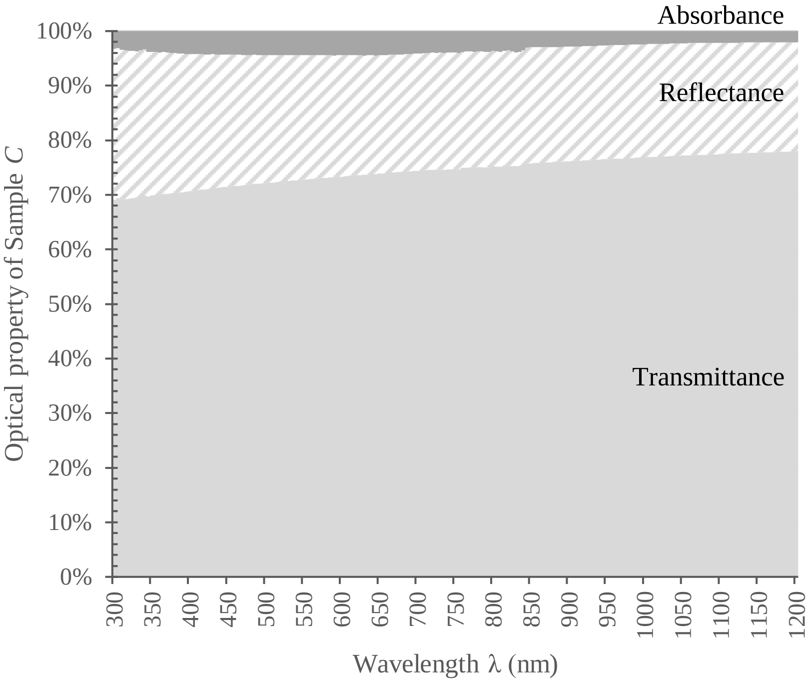

Figure 5.7 Light interaction of a single side polished sample with light incident on the polished surface

5.3 Nonlinear absorption of laser power

High intensity and ultrashort laser pulses induce nonlinear absorption within the material which modifies the material through the weakening of bonds. Therefore, it is imperative to analyze how surface morphology affects the threshold for nonlinear absorption within a material. Since it is impossible to directly measure the power absorbed by the sample, the power transmitted through the sample will be measured instead.

In reality, a Gaussian distribution is preferred as it has more applications for material processing. However, interpreting the results of a Gaussian distribution will be difficult due to its spatial non-uniform power intensity distribution. In the region of peak power intensity at the focus spot, the threshold for nonlinear absorption might have been surpassed. However, there could also be regions at the focus plane where the intensity is not high enough for nonlinear absorption to occur.

This makes the analysis problematic as the region of nonlinear absorption cannot be properly defined easily.

Instead, a laser beam with a flat top distribution was employed. A flat top distribution is rarely used in practice as more power is required to achieve the same high intensity, albeit for a smaller area. However, for a flat top distribution, the advantage is that the intensity at the focus spot is relatively constant. Therefore, any deviations from the expected result would be distinct and could be solely attributed to the change in power. The analysis of the results will be relatively straightforward as it will be distinct when the threshold for nonlinear absorption is surpassed. A beam shaper can be employed to change a Gaussian power distribution to that of a flat top.

The threshold for nonlinear absorption is determined as the first instance when the power absorbed by the sample was not directly proportional to the power irradiated on the sample. Since only the transmitted power was measured, the threshold was determined when the transmitted power through the sample decreased.

The determination of the threshold for nonlinear absorption for the three samples was done by changing the laser power output. The laser power levels were set at 5%, 20%, 40%, 60%, 80% and 95% of the maximum power output of 2.40 W. Once the nonlinear threshold was exceeded, additional data points of 5% power level increments between the two power levels were supplemented to increase the precision of nonlinear threshold determination.

The focus position was changed to determine if it has an impact on the threshold for nonlinear absorption. The focal positions chosen were at the top surface (z = 0 μm), midplane (z = +210 μm) and bottom surface (z = +430 μm) of the samples. The laser machine’s height setting was only accurate to 10 μm. Therefore, the midplane was focused at z = +210 μm, instead of exactly at the midplane where z = +215 μm. The focused spot diameter at the focal length was 27.1 μm.

5.3.1 Effect of scanning height on absorption characteristics

A control experiment was conducted where there was only linear absorption within the samples as a reference for these nonlinear absorption studies. It will give an indication to the extent of nonlinear absorption within the sample when the energy was sufficiently high. To identify the height at which only linear absorption was possible, the focal position was varied above the sample in the negative z direction until nonlinear absorption was not observed. In this experiment, the power level was set at 95% of the maximum power output as it gives the highest probability for nonlinear absorption to occur within the sample. The results are shown in Figure 5.8.

After the laser beam had passed through the samples, there was negligible fluctuation in power measured when the focus position of the laser beam was moved from z = –2 mm to z = –10 mm (i.e. the laser focus spot was above the sample's top surface). This indicated that the power absorption remained constant despite the change in the power intensity as the focal spot position and thus the area was varied. This meant that there was only linear absorption in the samples when the laser focus was positioned between z = –2 mm to z = –10 mm. As such, a focal position placed 5 mm above the top surface (z = –5 mm) would be more than sufficient to ensure that only linear absorption occurred.

The experiment was repeated at different focal positions for each sample. The largest standard deviations occurred mostly around the threshold for nonlinear absorption. Whereas for data points away from the threshold, most standard deviations were low indicating that the results were repeatable.

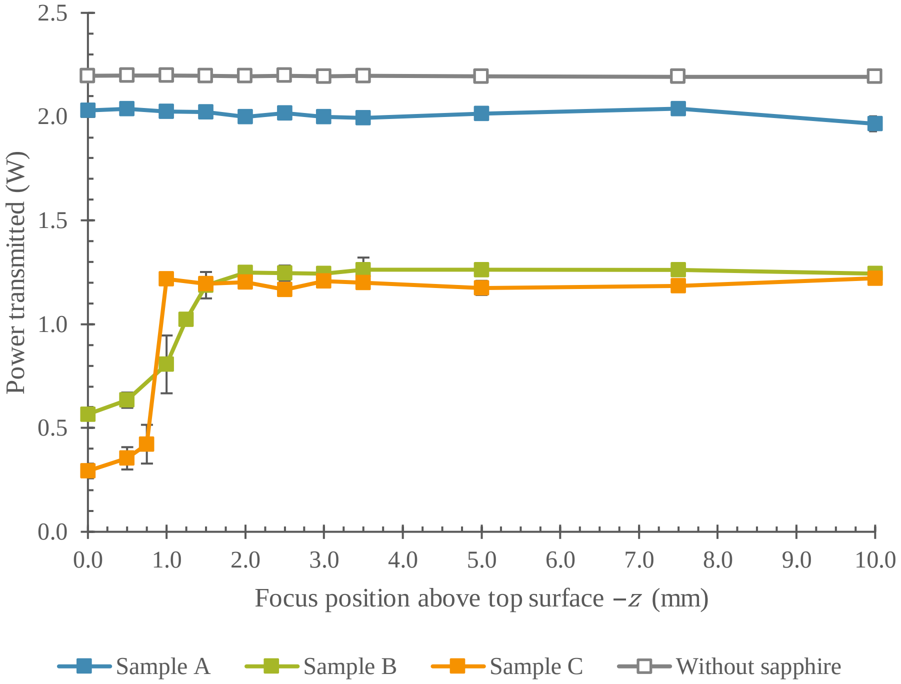

Figure 5.8 Power transmitted against focal position above top surface for all samples
The standard deviation ranges from 0.002 W to 0.059 W for linear absorption and 0.004 W to 0.139 W for nonlinear absorption

5.3.2 Linear absorption in Sample *A*

Even at high laser power levels, a flat top distribution was insufficient to trigger nonlinear absorption in the double side polished Sample *A*, see Figure 5.9. The power measured was linear and proportional to the laser power irradiated on the sample. Moreover, the percentage of power transmitted was relatively constant over the range of powers tested indicated that only linear absorption occurred.

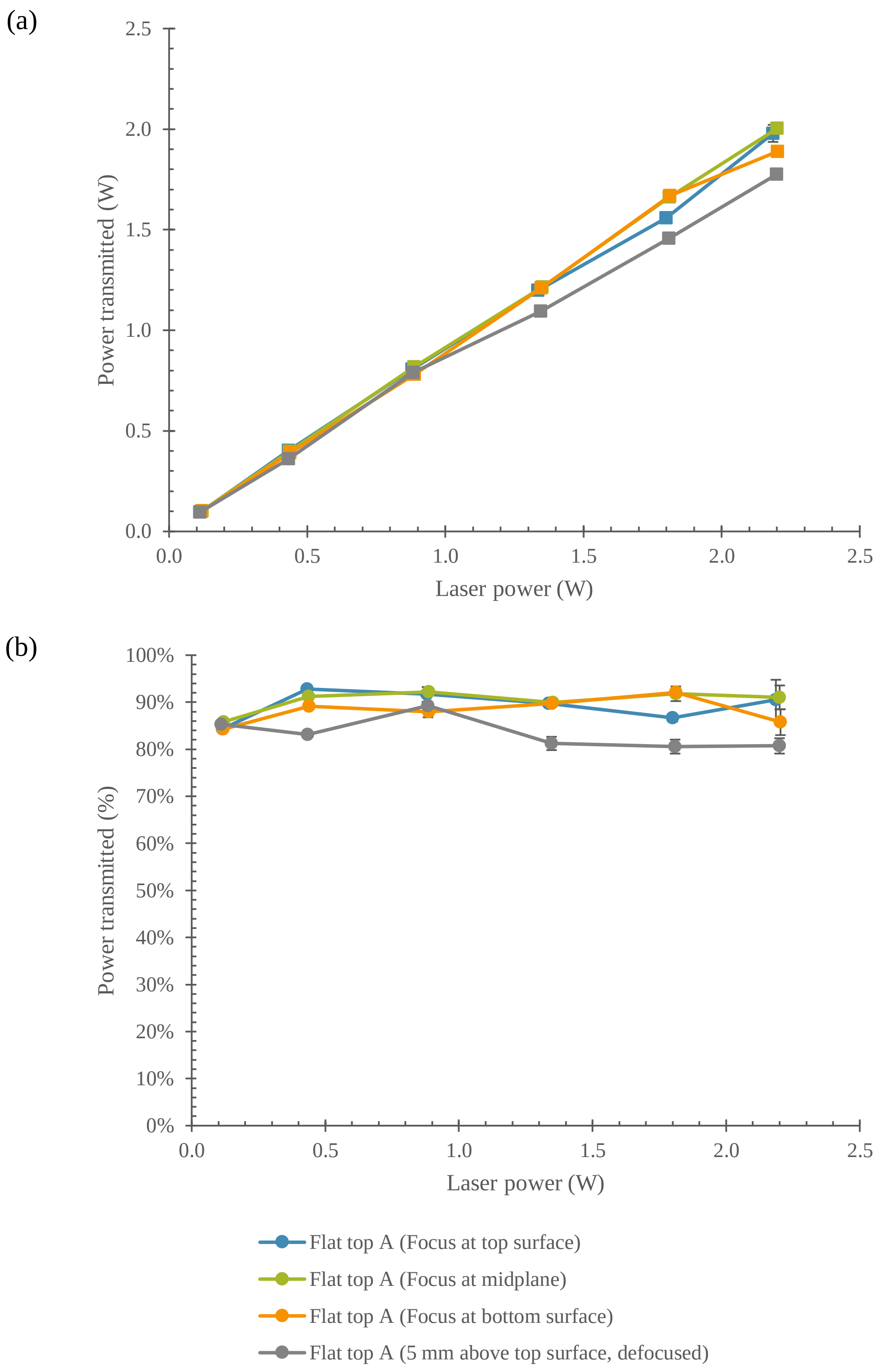

Figure 5.9 (a) Power measured and (b) percentage power transmitted against laser power irradiated for Sample A The standard deviation ranges from 0.001 W to 0.042 W

5.3.3 Nonlinear absorption in Sample *B*

In Figure 5.10, nonlinear absorption was observed for the experiments on Sample *B*. The only difference between Samples *A* and *B* was the introduction of a top rough surface for the latter. The threshold for nonlinear absorption for Sample *B* was estimated to be 1.4 W. When the laser light was incident on the rough surface, most of the reflected light will be diffusely reflected back into the atmosphere. However, due to the surface roughness of the top surface, some of the reflected light could be reflected onto the material itself. This trapped light and accumulated energy within this region. When there was sufficient accumulation of energy, nonlinear absorption within the sample was possible.

Additionally, the nonlinear absorption threshold was insensitive to the focal position within the sample. This may be further explained through the concepts of DOF, Rayleigh length z_R and fluence.

The Rayleigh length refers to the distance from the focal position to the point where the cross-sectional area of the laser beam has doubled, i.e. when the radius of the beam has increased by $\sqrt{2}$ of the focused spot diameter. The DOF is twice the Rayleigh length, above and below the focal position. The DOF and Rayleigh length are defined as [31], [38]:

$$DOF = 2z_R = 2\frac{\pi\phi^2}{4M^2\lambda} \tag{5.2}$$

Where DOF is the depth of focus, z_R is the Rayleigh length, ϕ is the focused spot diameter, M^2 is the beam quality factor and λ is the wavelength.

The Rayleigh length was calculated to be 417 μm, which was comparable to the thickness of the samples of 430 μm. Since the DOF is twice the Rayleigh length, this meant that the intensity of the laser did not vary to a large extent over the thickness of the sample. Therefore, the fluence and thus the energy deposition onto the sample at the different focal positions would be similar. This explains why the results for the different focal positions within the sample did not differ much from each other.

Once the threshold for nonlinear absorption for Sample *B* was exceeded, the amount of power measured by the sensor slowly decreased, even though the laser power output was increased steadily. Most of the fall in power transmitted could be attributed to the nonlinear absorption within the sample, if the assumption that the reflectivity of the sample remains constant holds true. When the power output was around 1.8 W, the power transmitted through the sample was relatively constant regardless of the focal position within the sample. At the largest power output of 2.2 W, the percentage power transmitted dropped to approximately 26%. By extrapolating the results, it indicated that as the power output further increases, nonlinear absorption within the sample would become more pronounced, resulting in a lower percentage of power transmission.

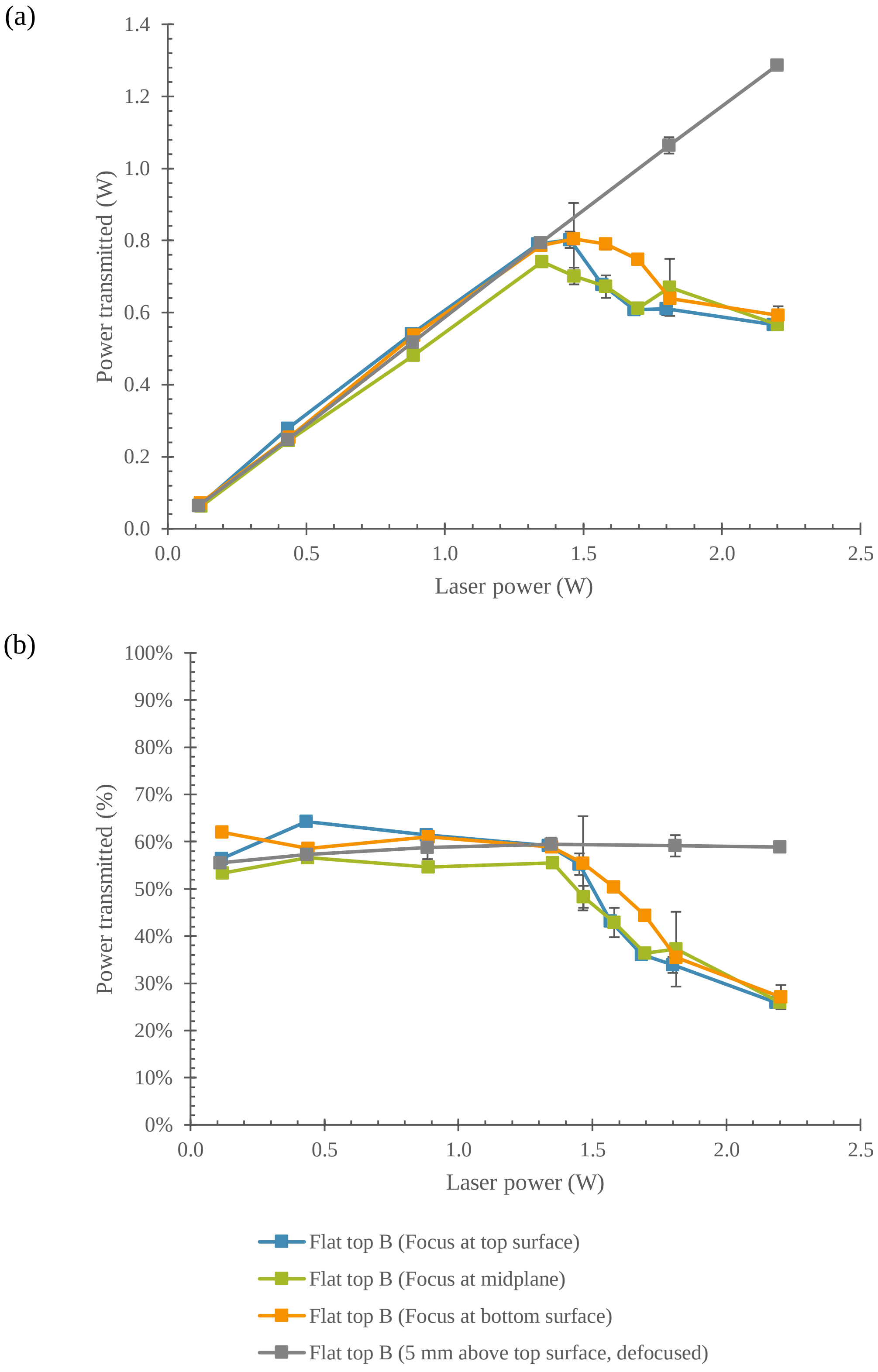

Figure 5.10 (a) Power measured and (b) percentage power transmitted against laser power irradiated for Sample B
The standard deviation ranges from 0.001 W to 0.025 W for linear absorption and 0.002 W to 0.100 W for nonlinear absorption

5.3.4 Nonlinear absorption in Sample *C*

The first occurrence of nonlinear absorption was at the bottom rough surface for Sample *C*. Although this is counter intuitive, its occurrence can be deduced by comparing the results of Sample *C* to Sample *A*. Intuitively, nonlinear absorption should occur on the sample's top surface as the laser power intensity would be the highest and progressively becoming less as the laser beam passes through the sample.

With the current setup for a rather thin sample and large Rayleigh length, even when the laser beam was focused on the bottom surface of the sample, the laser intensity on the top surface would still be higher than that of the lower surface due to linear absorption of energy within the bulk thickness. Sample *A* had double side polished surfaces, while Sample *C* had a top polished surface and a bottom rough surface. As such, for the same laser power, the condition at the top surface and the sample interior for Samples *A* and *C* would be similar. The only difference will be the rough bottom surface of Sample *C* as compared to the smooth bottom surface of Sample *A*. However, since Sample *A* did not experience nonlinear absorption even at high power levels, it could be concluded that the bottom rough surface of Sample *C* was indeed the location and cause for the observed nonlinear absorption. The plausible explanation is that the internally reflected light from the bottom rough surface had elevated the laser power intensity beyond the threshold for the occurrence of nonlinear absorption for Sample *C*.

From Section 5.2, it was concluded that Sample *C* exhibited a greater linear absorbance than the other two samples due to its bottom rough surface. Intuitively, one would expect that Sample *C* should have a lower threshold for nonlinear absorption than Sample *B*. Yet Sample *C* was observed to have an even higher threshold for nonlinear absorption at about 1.9 W, see Figure 5.11. Likewise, the threshold was insensitive to the focal position within the thin sample.

The reason was due to the location of the rough surface. For Sample *B*, the rough surface was facing towards the laser. While for Sample *C*, the rough surface was facing away from the laser. For internal reflection to occur in Sample *C*, light had to travel through the thickness of the sample before arriving at the bottom rough surface. Some of the laser's energy had already been linearly absorbed by the material as it was propagating through the sample. By the time the light reached the bottom rough surface, the energy it carried would have been lower than that at the top surface. Therefore, higher laser power output would be required before Sample *C* could reach the nonlinear absorption threshold within the material.

An observation was that just beyond the threshold for nonlinear absorption, by increasing the power irradiated slightly, the extent of nonlinear absorption greatly increased. In fact, the percentage power transmitted fell approximately from 54% to 14%, which was about a 40% decrease in transmitted power. This is expected as nonlinear absorption increases much faster with an increase in laser power as compared to liner absorption.

These experiments indicated that Sample *B*'s threshold for nonlinear absorption was the lowest at 1.4 W. It has to be highlighted here that the extent of nonlinear absorption spatially would be small overall. Yadav et al. mentioned that once the threshold for nonlinear absorption was exceeded, strong multiphoton absorption will occur at the laser focus of high intensity [10]. The damage will be localized and will not affect the other regions within the structure. Since Sample *B* has a rough top surface, most of the laser energy was diffused on that surface. The uneven surface allowed for the reflection of laser light back onto the material itself, trapping light within the region near the top surface. As such, this lower threshold for Sample *B* due to nonlinear absorption was confined to the rough top surface, where the laser energy was accumulated. The modified region near the top surface blocked energy from transmitting to the bottom surface and out of the sample. Even with some internal reflection at the bottom polished surface, the accumulation of energy was still insufficient to induce nonlinear absorption at the bottom surface. Hence, a lower power transmitted was measured by the sensor.

In Section 3.1, it was hypothesized that Sample *C* had the highest possibility for internal reflection at the bottom rough surface. If this hypothesis is valid, then once the nonlinear absorption threshold is reached at the bottom surface, there will be significant absorption within this region resulting in much less transmission as power increases. This significant increase can be attributed to the internal reflection of light back into the thickness of the sample, further enhancing the energy accumulation within the material. As the power was increased, the region of nonlinear absorption could expand from only the very vicinity next to the bottom surface to induce nonlinear absorption in the surrounding regions especially along the optical axis. As a result, an increase in nonlinear absorption was possible in the sample. Thus, a drastic fall in power transmitted can then be expected for Sample *C*. However, the extent of expansion of the nonlinear absorption region into the sample's thickness could not be ascertained.

Indeed, examining the results in Figure 5.11, it can be observed that as compared to Samples *A* and *B*, there was a much higher rate of decrease in transmitted power for Sample *C* once the nonlinear threshold was exceeded. This observation is consistent with the proposed hypothesis of internal reflection at the bottom rough surface of Sample *C*.

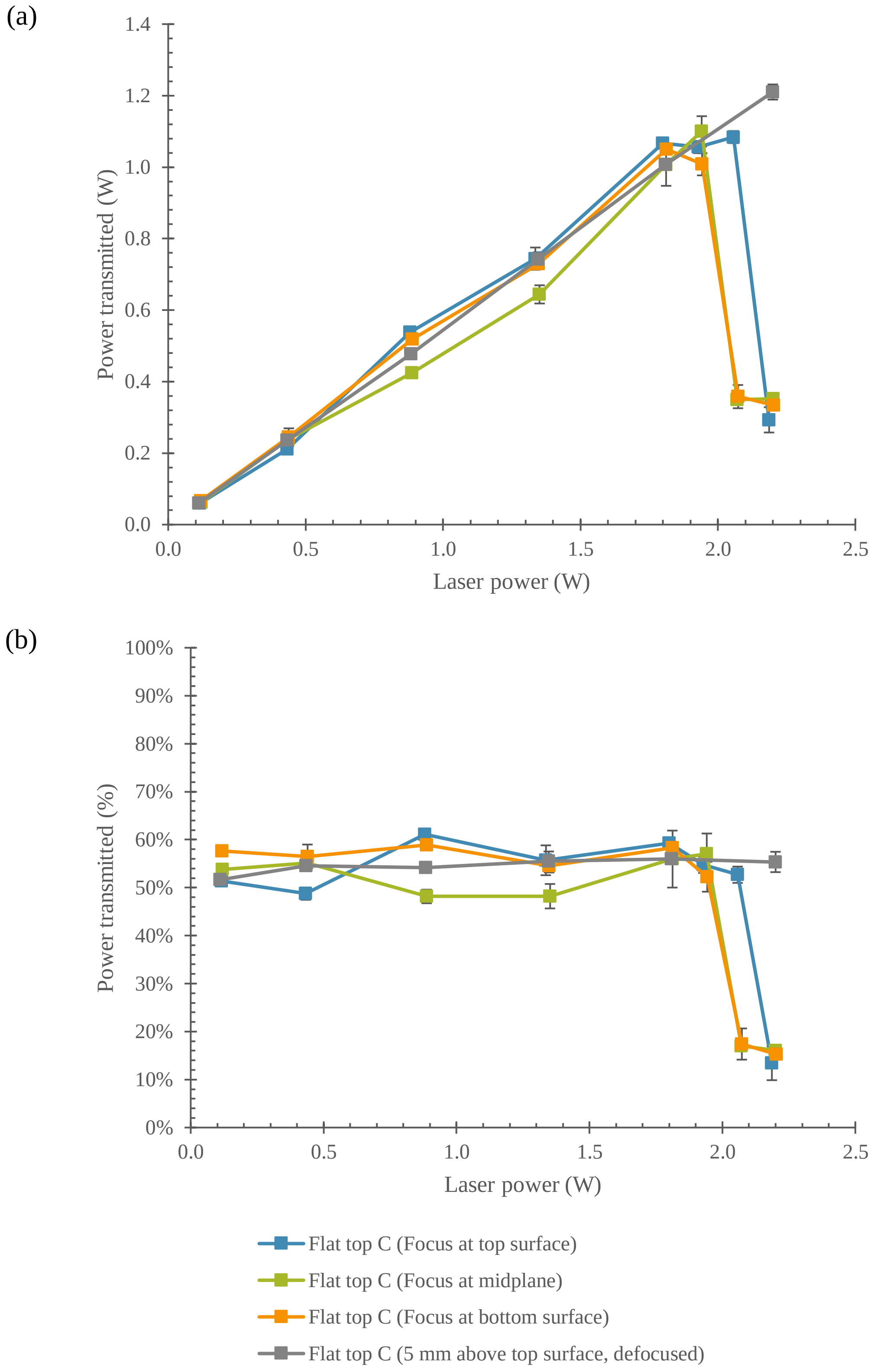

Figure 5.11 (a) Power measured and (b) percentage power transmitted against laser power irradiated for Sample C
The standard deviation ranges from 0.001 W to 0.031 W for linear absorption and 0.003 W to 0.059 W for nonlinear absorption

5.4 Picosecond laser irradiation

To better represent practical implementations, a Gaussian beam distribution was employed as this is the general industry practice. The laser beam, facilitated by a galvo scanner, was focused on the top surface of sapphire samples in the three orientations as described in Section 3.1. The laser powers employed were approximately 25%, 50% and 75% of the maximum power of 2.4 W. It was suggested that the optimal scanning speed for ablation scribing, without the formation of cracks or debris, was above 200 mm/s. At this speed, only a few overlapped pulses was required to achieve optimal material removal [39].

In this investigation, the laser scanned the sample in a single pass with a constant scanning speed of 240 mm/s and a pulse repetition rate of 50 kHz. The focused spot diameter at the focal length was 27.1 μm. When the laser was set to the minimum pulse repetition rate of 50 kHz, it produced pulses with maximum peak energy. As such, there would be a higher probability of the sample interacting with the laser in the nonlinear absorption regime at these higher powers.

The number of pulses overlap may be calculated as [40]:

$$N = \frac{R_p \phi}{v} \tag{5.3}$$

Where N is the number of pulses overlap, R_p is the pulse repetition rate, ϕ is the focused spot diameter on the material surface and v is the scanning speed.

Using Equation 5.3, the resulting number of pulses overlap in this investigation was calculated to be 5.65 pulses.

The pulse energy of a single pulse can be calculated as [41]:

$$Q = \frac{P}{R_p} \tag{5.4}$$

Where Q is the pulse energy and P is the average power.

The fluence at the top surface of the samples can be calculated as [42]:

$$F = \frac{Q}{\pi\omega^2} \tag{5.5}$$

Where F is the fluence and ω is the radius of the laser beam spot on the sample's top surface.

Table 5.1 presents the calculated fluence incident on a sample's surface for a given laser power.

Table 5.1 Power level and the corresponding fluence

Power level	**Actual power (W)**	**Fluence (J/cm^2)**
25%	0.5	1.73
50%	1.1	3.82
75%	1.7	5.90

Three lines were scanned, each with a single pass, to ensure repeatability of the results. At 0.5 W (25% power), there were virtually no scribes (or rather, very faint scribes) observed on the top and bottom surfaces of the samples, see Column A of Tables 5.2, 5.3 and 5.4. This was probably due to insufficient power to result in significant sample modification. At higher power settings of 1.1 W and 1.7 W (power levels of 50% and 75% respectively), some scribes were observed on the samples' surfaces, see Columns B and C of Tables 5.2, 5.3 and 5.4. The optical images of sapphire samples of different surface morphologies after laser irradiation at different power output at 5× and 10× magnifications are presented in Appendix II.

5.4.1 Irradiation of Sample *A*

For Sample *A* at 0.5 W, no scribes were observed as there was insufficient energy for scribes to form on either polished surface, see Column A of Table 5.2. Likewise, at 1.1 W, there was still insufficient energy at the top surface for scribes to form, see Row 1 Column B of Table 5.2. However, crack dominated scribes was observed on the bottom surface even though the surface was polished, see Row 2 Column B of Table 5.2. Natural reflection occurs at an interface between materials of different refractive indexes and it is more pronounced when a surface is polished. The reflected light along with the incoming light resulted in the accumulation of energy at the region near the bottom polished surface. The accumulated energy was higher than the threshold for crack formation, hence non-uniform cracks were observed.

The cracks produced many micro-surfaces within the sample, with each facing a different random direction. Similar to a rough surface, these micro-surfaces reflected light off the micro-surface onto other micro-surfaces. This trapped light effectively accumulated energy within this region. When there was sufficient energy to cross the threshold for ablation, ablation dominated scribes were formed. At areas where there was insufficient energy at the surface for ablation, only cracks were observed.

When the power irradiated on the surface was increased to 1.7 W, there was sufficient energy for the formation of crack dominated scribes on the top polished surface of Sample *A*. However, there was insufficient energy at the bottom surface for the formation of scribes, see Column C of Table 5.2. As suggested in Section 5.3, the top rough surface of Sample *B* trapped and accumulated energy within this region. Therefore, nonlinear absorption was only confined to the region near the top surface but not in the rest of the sample's thickness. Similarly, the micro-surfaces in Sample

A was a substitute rough surface that prevented high energy laser energy from propagating to the bottom surface. Hence, no scribes were observed on the bottom surface.

Table 5.2 Optical images of sapphire samples after laser irradiation at different power output for Sample A at 20× magnification

	Power		
	0.5 W 25% power level *Column A*	**1.1 W** 50% power level *Column B*	**1.7 W** 75% power level *Column C*
	A Double side polished		
Top (polished) *Row 1*			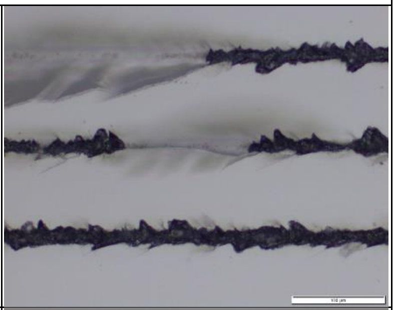
Bottom (polished) *Row 2*	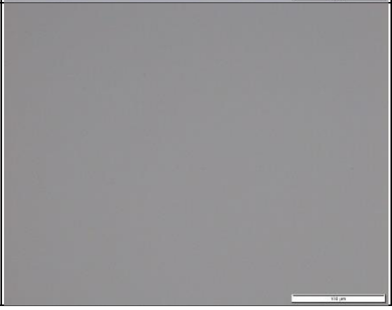	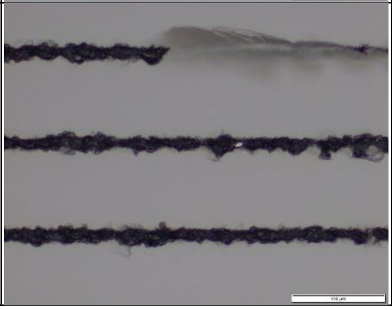	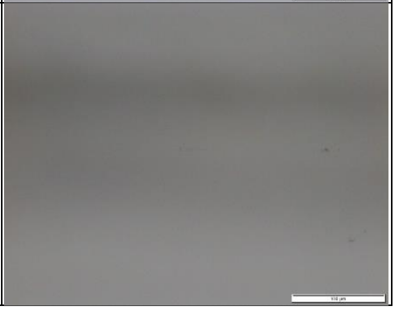

5.4.2 Irradiation of Sample *B*

For Sample *B*, ablation dominated scribes were observed on the top rough surface, even at a low power of 0.5 W, see Row 1 of Table 5.3. The reason was that the top rough surface was very effective in trapping light within this region and it accumulated enough energy within the rough surface for ablation to occur. However, due to the low power, the ablation scribes observed were rather faint. By increasing the laser power to 1.1 W and 1.7 W, more pronounced and thicker ablation dominated scribes were observed as more energy was accumulated at this region.

Since nonlinear absorption was only confined to the top region of the sample as previously discussed, only low energy light could propagate to the bottom surface. Hence, no scribes were found on the bottom polished surface of Sample *B* for all powers, see Row 2 of Table 5.3.

Table 5.3 Optical images of sapphire samples after laser irradiation at different power output for Sample B at 20× magnification

	Power		
	0.5 W 25% power level *Column A*	**1.1 W** 50% power level *Column B*	**1.7 W** 75% power level *Column C*
	B Single side polished Light incident on unpolished surface		
Top (unpolished) *Row 1*	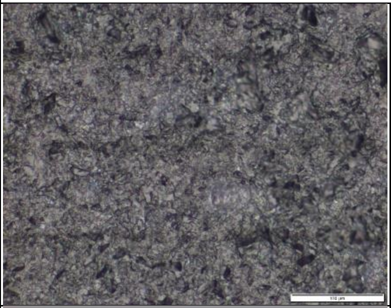	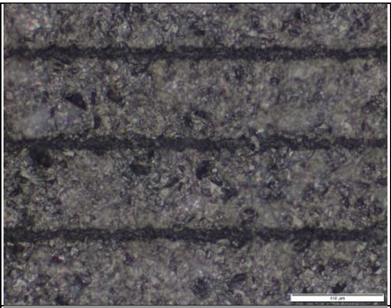	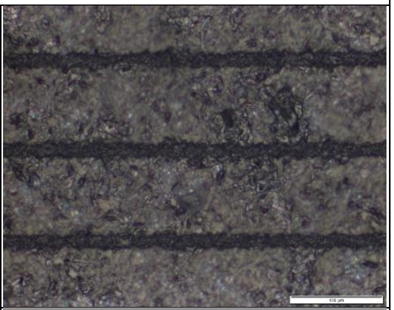
Bottom (polished) *Row 2*			

5.4.3 Irradiation of Sample *C*

Similar explanation could be employed to account for the ablation dominated scribes observed on the bottom rough surface for Sample *C*, even when the laser power was low, see Row 2 of Table 5.4. However, in this case, it was due to internal reflection at the bottom rough surface, back into the material, that allowed for the accumulation of energy for ablation.

For Sample *C* at 0.5 W, there was insufficient energy for any scribes to form on the sample's top polished surface, see Row 1 Column A of Table 5.4. The interesting observation was that at the higher powers of 1.1 W and 1.7 W, there was some form of scribes found on the top surface, see Row 1 Columns B and C of Table 5.4 respectively. At 1.1 W, there was mostly insufficient energy for nonlinear absorption on the top surface for any scribes to form. However, at some instances, there was sufficient accumulation of energy from both incoming laser light and internally reflected light from the bottom surface to exceed the threshold for crack formation. Thus, some cracks could be observed. While at a higher power of 1.7 W, the energy accumulated on the top polished surface was just sufficient to cross the threshold for ablation. Therefore, thin ablation dominated scribes were mostly observed. Though at certain areas whereby the accumulated energy was insufficient for ablation, crack dominated scribes were observed instead.

Table 5.4 Optical images of sapphire samples after laser irradiation at different power output for Sample C at 20× magnification

	Power		
	0.5 W 25% power level *Column A*	**1.1 W** 50% power level *Column B*	**1.7 W** 75% power level *Column C*
	C Single side polished Light incident on polished surface		
Top (polished) *Row 1*			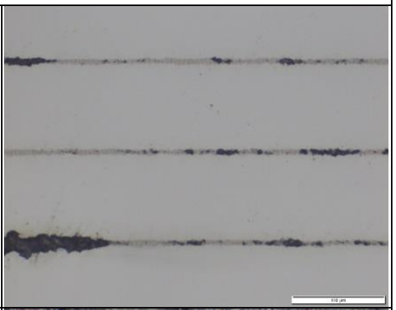
Bottom (unpolished) *Row 2*	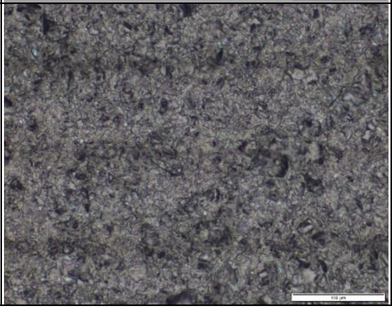	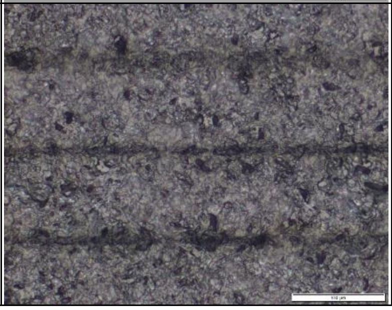	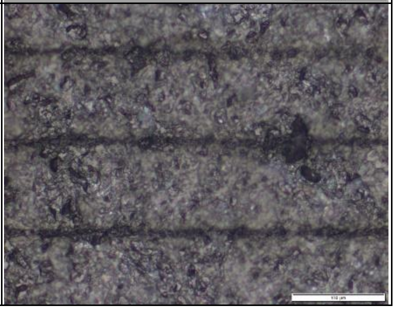

5.5 Conclusion

The investigation of the linear optical properties of sapphire samples highlighted the difference in light interaction between a rough and smooth surface. A smooth surface displayed higher levels of transmittance; a rough surface displayed higher levels of reflectance. As such, Sample *A*, with two polished surfaces, exhibited the highest transmittance; Sample *B*, with a top rough surface, exhibited the highest reflectance. As a result of a bottom rough surface that encouraged internal reflection of light within the sample, Sample *C* displayed the highest level of absorbance.

The study of the nonlinear absorption characteristics of the sapphire samples highlighted the dependency of the nonlinear absorption threshold on the surface roughness of the samples. A flat top beam distribution was employed to provide a relatively constant intensity at the focus spot, such that the threshold could be more precisely determined. Nonlinear absorption could not be induced in the two polished surfaces Sample *A* and the light was mostly transmitted through the sample. With the introduction of a single rough surface, nonlinear absorption could be detected in Sample *B* and Sample *C*. The location of the rough surface affected the nonlinear absorption threshold and the extent of nonlinear absorption within the samples. The top rough surface of Sample *B* had a lower threshold, and likely that nonlinear absorption was confined to the region around the top rough surface. Sample *C* required more laser power to reach the nonlinear absorption threshold as a result of having its rough bottom surface located away from the laser source. However, internal reflection at the bottom surface back into the sample encouraged a more dominant nonlinear absorption in the vicinity of the bottom surface once the threshold is exceeded.

A Gaussian beam distribution is preferred for machining applications as the laser beam has higher intensity at the focal spot. With a higher intensity, nonlinear absorption was observed for all samples at the highest laser power of 1.7 W. Even though nonlinear absorption was now possible for Sample *A*, the extent was not large enough to form ablation dominated scribes; instead crack dominated scribes were observed on the top surface instead. In contrast, the presence of a top rough surface on Sample *B* encouraged the formation of ablation scribes. However, since nonlinear absorption was mainly confined to the region around the top surface, no scribes were observed on the bottom polished surface. Sample *C* with internal light reflection at its bottom rough surface had sufficient energy accumulation throughout the sample's thickness to form ablation scribes on both top and bottom surfaces of the sample.

Machining and singulation of sapphire would require nonlinear absorption within the material. Sample *C* with ablation scribes on both sample surfaces indicated that a sample with a rough bottom surface will be favorable for laser-material interaction for machining of transparent sapphire.

6 Single zone multiple foci laser irradiation of sapphire

MF optics can be utilized to split the laser energy among multiple foci. When coupled with a focusing optic, a line of foci is produced at different focal lengths along the optical axis, forming a quasi-elongated focus within the material [36]. As such, the temperature distribution within the material thickness would not be concentrated at a single spot, but over a larger region. Hence, the formation of a more even thermal and mechanical stress distributions within the material would result in less crack deviations away from the intended scan lines [12]. In addition, the introduction of MF optics allowed the samples to interact nonlinearly with the laser at different focal lengths simultaneously. As a result, a plane of modification was produced along the optical axis. Successful mechanical cleavage of the samples revealed a roughened sidewall profile.

In this chapter, the MF optics were paired with focusing optics with various EFL for sample irradiation. Each sample would only be scanned once by the laser at a specified z height. As such, it is defined as a single zone scan.

6.1 Laser power under various single focus lenses

It is imperative that a fair comparison between different combinations of MF and focusing optics be carried out. This allows the end user to understand and to select the combination which is best suited for each specific experiment.

Figure 6.1 shows the laser power transmitted for a controlled setup, without any optics, and with the various focusing optics only, without MF lens. The aperture of the laser beam was shrunk to form an unfocused beam diameter of 6.0 mm; this corresponded to the focusing optic with the smallest aperture (focusing lens with EFL = 7.5 mm).

Each focusing optic exhibited different levels of power attenuation. The focusing lens with an EFL of 12 mm had the least attenuation of about 0.5%, while the OB40× lens displayed the highest power loss of about 40%. The OB10× lens had an attenuation of approximately 12%, while both the OB20× lens and the focusing lens with an EFL of 7.5 mm displayed a similar power loss of approximately 20%. Both MF lenses (9 foci and 27 foci) had an attenuation of about 2%.

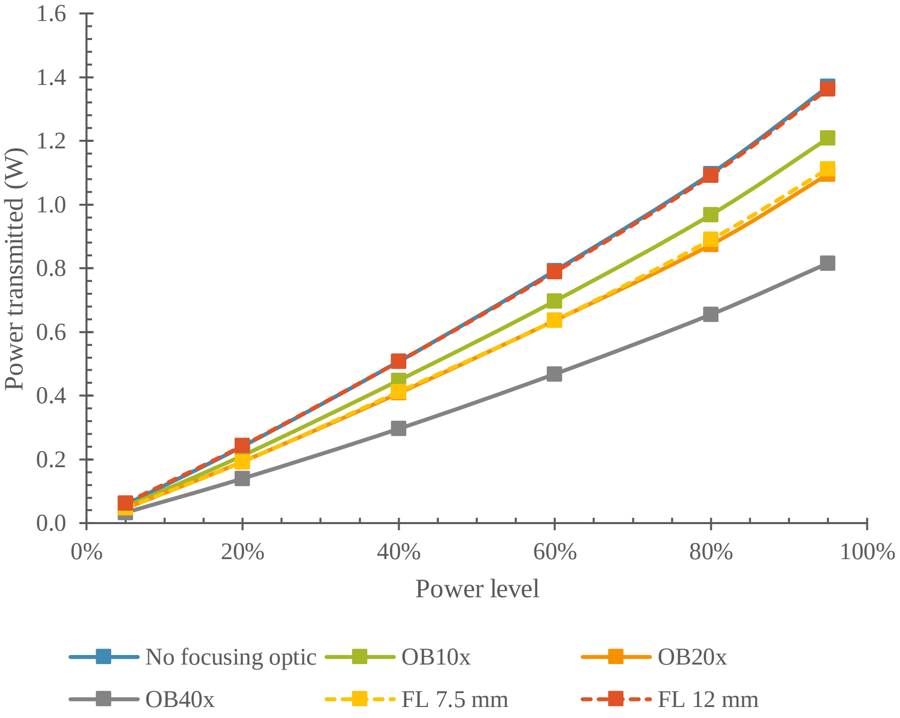

Figure 6.1 Power transmitted for different focusing optics without MF lens or samples
OB refers to the objective lens magnification (solid line) and FL refers to the focusing lens (dashed line)
The standard deviation ranges from 0.000 W to 0.005 W

6.2 Effect of effective focal length on multiple foci laser irradiation

This investigation aims to understand how these parameters affect the scribe characteristics of the samples. The EFL of the focusing optic determines the foci separation between the multiple foci. By changing the EFL of the objective lenses and laser scanning heights, as seen in Figure 4.8 of

Section 4.2.3.3, the effects of foci separation, number of foci focused within the sample and the power distribution amongst foci can be studied.

In this investigation, the 27 foci MF lens was paired with three different objective lenses to determine the most suitable EFL for the singulation of the sapphire samples with thickness of 430 μm. Although employing the 9 foci MF lens was possible, its limited number of foci did not provide the flexibility required to study a large variation in the number of foci focused within the sample. In addition, its average foci separation was similar to that of the 27 foci counterpart, see Table 6.1. The 27 foci MF lens was chosen as the 27 foci MF lens provided more foci to work with, allowing a larger range of parameters for investigation.

Table 6.1 Comparison of foci separations between 27 foci and 9 foci MF lens

EFL of focusing optic (mm)	**Average foci separation (μm)**		**Max no. of foci within sample**	
	27 foci	**9 foci**	**27 foci**	**9 foci**
20 (OB10×)	109.4	121.2	5	4
10 (OB20×)	27.3	30.3	16	9
4.38 (OB40×)	5.2	5.8	27	9

6.2.1 Laser power under various multiple foci

Without any sample, the power transmitted was measured after the laser passed through the 27 foci MF lens and an objective lens. Figure 6.2 presents the power transmitted for the combination of the MF lens with each of the three objective lenses individually. Although the combination with the OB40× lens had the largest power attenuation, it could focus all 27 foci within the sample's thickness such that all of the laser power could theoretically be deposited into the sample. Even though the OB10× lens exhibited the least power attenuation, only a maximum of 5 foci could be focused within the sample at any point in time. As such, only a small percentage of the laser power could be transferred to the sample and the laser power would not be entirely utilized.

The laser power was adjusted accordingly such that the laser power deposited into the sample remained constant regardless of the combination of optics employed. Experiments in this section were carried out at a power of 0.22 W for irradiation within the samples.

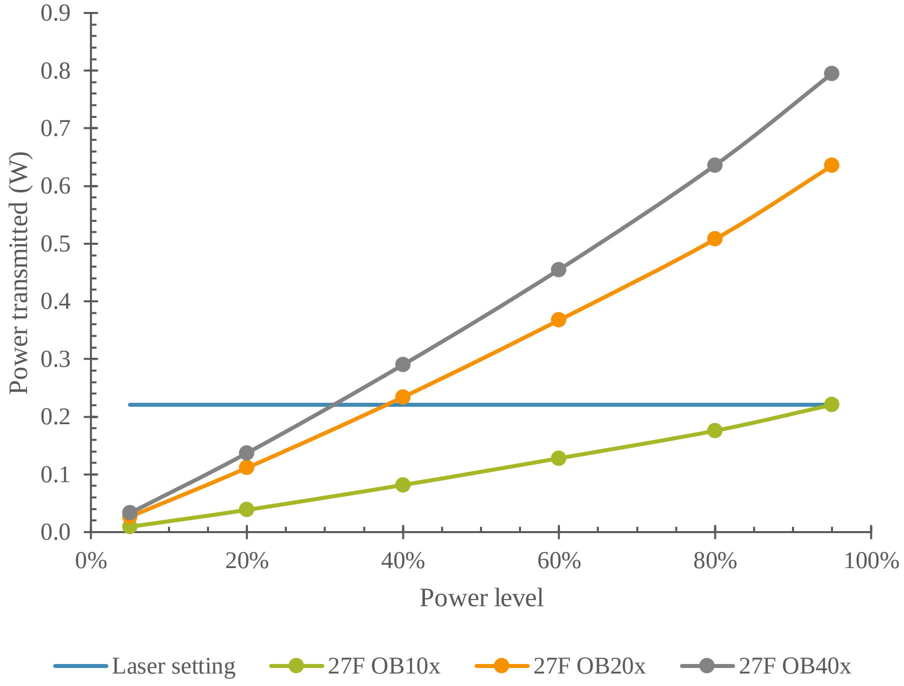

Figure 6.2 Power transmitted for 27 foci lens and respective objective lenses without any samples The standard deviation ranges from 0.000 W to 0.004 W

Even though the same power was employed, the power density differed depending on the focused spot diameter. In turn, the focused spot diameter depended on the EFL of the focusing optic.

The power density at the focused spot, also known as intensity, can be calculated from [42]:

$$I = \frac{P}{\pi \omega_0^2} \tag{6.1}$$

Where I is the power density, P is the average power and ω_0 is the focused spot radius.

By introducing an objective lens with a higher magnification, the EFL of the focusing optic would decrease and the light would be focused into a smaller focus spot according to Equation 3.4. Reducing the EFL while keeping the overall laser power constant ultimately increases the power density at each focus. With the laser power set at 0.22 W, the power densities for each experiment are tabulated in Table 6.2.

Table 6.2 Power densities for experiments with a combination of 27 foci MF and various objective lenses

Focusing optics	**EFL (mm)**	**Power per focus (W)**	**Focused spot radius (μm)**	**Power density per focus (W/cm^2)**
OB10×	20	44.1	2.94	16300
OB20×	10	13.8	1.47	20400
OB40×	4.38	8.18	0.643	63000

The power per focus spot for the OB10× lens was the highest compared to the other two objective lenses. However, since it exhibited the largest focused spot radius, it's power density per focus was the lowest. Since nonlinear absorption within a sample required high laser intensity to occur, the combination with the OB10× lens would be less effective to result in nonlinear absorption.

For all the experiments, the laser had a low pulse repetition rate of 50 kHz and a moderate scanning speed of 1 mm/s. This pulse repetition rate was selected as it generated the highest peak power the laser could produce. A high peak power was required to encourage nonlinear absorption within the samples for internal modification of the material. The scanning speed was much slower than the speed used in Section 5.4, i.e. 240 mm/s, to account for the reduction in laser power employed. Sample *C*, with a top polished surface and a bottom rough surface, was used in the experiments.

6.2.2 27 foci irradiation with OB10× lens

For the OB10× lens, no ablation dominated scribes were observed on the top polished surface of the sample. Even with more power allocated to a single focus, each focus had a low power density. Coupled with the large foci separation of 109.4 μm and a long Rayleigh length of 19.6 μm, it was simply unable to accumulate sufficient energy at the top surface for ablation dominated scribes to form. Instead, only when a focus was positioned close enough to the top surface, the accumulation of energy was just sufficient to form a crack dominated scribe. Figure 6.3 (a) shows the scan where diffractive order –6 was positioned about 10 μm away from the top surface. Since the distance between diffractive order –6 and the top surface was below the Rayleigh length of 19.6 μm, a crack dominated scribe was observed. Furthermore, successive scans did not always produce crack dominated scribes on the top surface due to the lack of proximity of the focus to the surface.

However, a different trend was observed on the bottom rough surface. As a result of internal reflection at the bottom rough surface, it allowed the accumulation of energy effectively within this region close to the bottom surface. Even though the foci separation was large, and sometimes the distance between a focus and the surface was larger than the Rayleigh length, the energy accumulated due to internal reflection was sufficiently high to form ablation dominated scribes on the bottom surface for successive scans. Figure 6.3 (b) shows a faint ablation scribe with a width of 4.3 μm on the bottom surface, when diffractive order –4 was about 45 μm away from the surface.

Only at two instances scribes were observed on the top surface, i.e. when diffractive orders –6 and +5 were positioned close to the top surface. Whereas for the bottom surface, successive scribes were observed from diffractive orders of –8 to +5. It appeared that foci further away from the focus of diffractive order 0 had a smaller proportion of power allocated. Therefore, scribes on both the top and bottom surfaces were only observed for foci closer to diffractive order 0. Furthermore, the same set of diffractive orders were responsible for the scribes observed on either surface. A slight difference in scribes was observed for the negative diffractive orders which could be a result of the larger step size compared to the foci separation (i.e. 200 μm and 109.4 μm respectively). The average thickness of the scribes observed was 7.2 μm and 6.8 μm of for the top and bottom surfaces respectively. The standard deviation ranges from 0.3 μm to 0.8 μm for the top surface scribes and 0.1 μm to 1.4 μm for the bottom surface scribes.

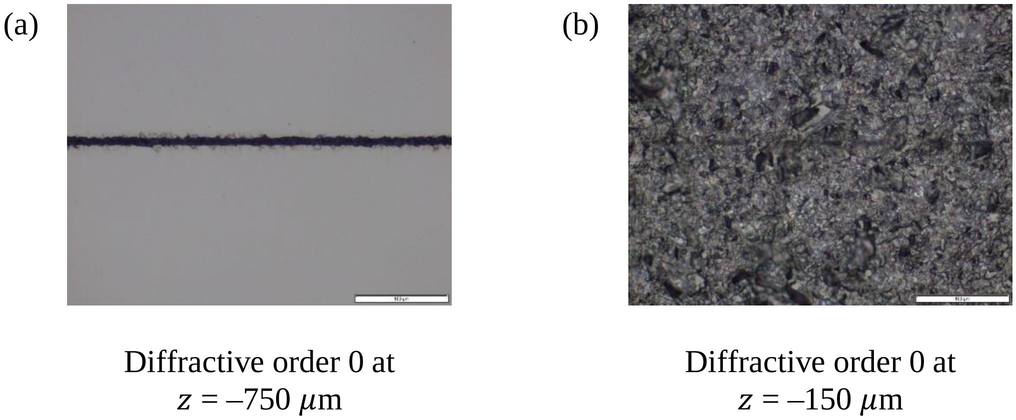

Diffractive order 0 at
z = –750 μm

Diffractive order 0 at
z = –150 μm

Figure 6.3 Optical images of scribes on (a) top and (b) bottom surfaces for MF laser irradiation with OB10× lens

6.2.3 27 foci irradiation with OB20× lens

The optical images for multiple foci laser irradiation with OB20× lens are presented in Figure 6.4. For the OB20× lens, a combination of crack and ablation dominated scribes were observed on the top polished surface of the samples. Figure 6.4 (a) is an example of an ablation dominated scribe.

Similar to the observations for the OB10× lens experiments, consecutive scribes on the top surface were not observed. However, the frequency of scribes was more consistent as the foci separation and Rayleigh length were greatly reduced (27.3 μm and 4.89 μm respectively). At certain scanning heights whereby there was no visible scribe formation, subsurface damage was observed instead, see Figure 6.4 (b).

The bottom rough surface of the samples were observed to have successive ablation dominated scribes. Despite having a shorter Rayleigh length, internal reflection at the unpolished surface allowed the accumulation of energy for the formation of ablation scribes. These ablation scribes were observed to be either dotted or in a solid line, see Figure 6.4 (c) and (d) respectively. It appeared that the type of scribe formed was independent of the distance between the focus and the bottom surface. Instead, it could be dependent on the interaction between the internally reflected light at the bottom surface with the incoming light. Since the rough surface was uneven and not uniform, this interaction was random resulting in randomness of the type of scribes formed. The average thickness of the scribes was 3.8 μm and 3.5 μm for the top and bottom surfaces respectively. The standard deviation ranges from 0.3 μm to 0.5 μm for the top surface scribes and 0.1 μm to 1.6 μm for the bottom surface scribes.

With the OB20× lens, a larger range of diffractive orders was responsible for the scribes formed on both the top and bottom surfaces. Diffractive orders –3 to +10 were responsible for the scribes observed on the top surface, while diffractive orders –9 to +4 scribed the bottom surface. Although the range of diffractive orders responsible for scribing on the top and bottom surfaces differed, the number of foci within the ranges remained the same. A possible explanation was that a minimum number of foci had to be focused within the sample such that there was sufficient accumulation of energy through nonlinear absorption for scribes to be formed or subsurface damage to be observed.

In this case, approximately ten foci had to be focused in the sample's thickness to induce nonlinear absorption in the sample. Since ten foci was lower than the maximum number of foci that could be focused within the sample, modifications were observed on the surface which the foci were close to. For example, if the ten foci were close to the bottom surface, the scribe would be formed on the bottom surface.

For some experiments, even though diffractive order 0 was not focused within the sample's thickness, scribe formation on either surface by other diffractive orders was possible. For example, diffractive order –3 was near the top surface and was responsible for the scribe observed in Figure 6.4 (a). At this scanning height, diffractive order 0 was 70 μm above the sample's top surface.

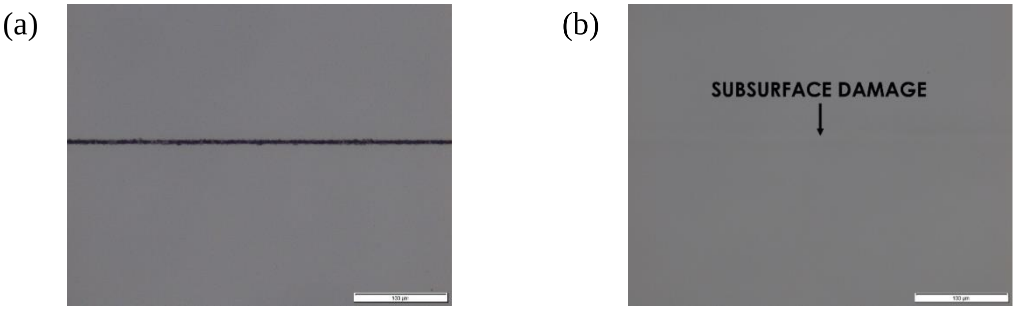

Diffractive order 0 at $z = –70\ \mu$m

Diffractive order 0 at $z = +180\ \mu$m

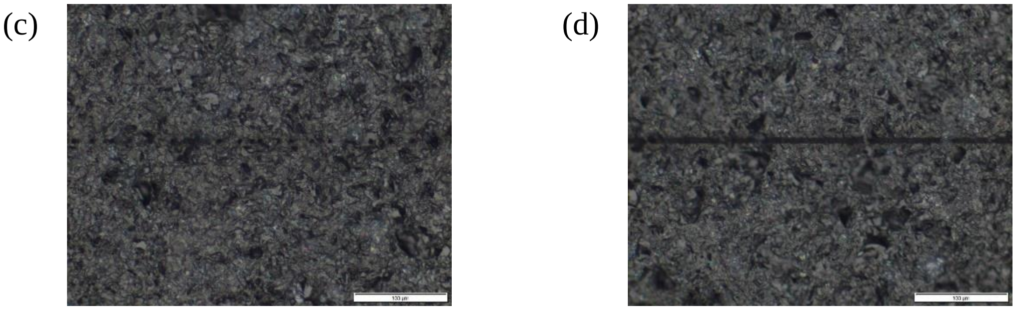

Diffractive order 0 at $z = +180\ \mu$m

Diffractive order 0 at $z = +530\ \mu$m

Figure 6.4 Optical images of scribes on (a and b) top and (c and d) bottom surfaces for MF laser irradiation with OB20× lens

6.2.4 27 foci irradiation with OB40× lens

For the OB40× lens, a combination of crack and ablation dominated scribes were observed on the top polished surface of the samples, see Figure 6.5 (a). Consecutive scribes were observed as a result of an even shorter foci separation and Rayleigh length (5.2 μm and 0.94 μm respectively). Due to the higher power density of each focus when the OB40× lens was employed, a larger range of diffractive orders could be responsible for the formation of scribes on the top surface. From the optical images, it was deduced that diffractive orders –9 to +10 could be responsible for the top surface scribes. Taking into consideration the step size of the experiments, it was possible that only a few foci of high power density were required to be focused within a sample for the formation of visible scribes.

Diffractive order +13 (i.e. the focus closest to the laser source) was responsible for the ablation scribe observed in Figure 6.5 (b). Additionally, a single cracked line was observed adjacent to the scribe. This could be due to the high laser energy concentration near the top surface that induced internal modification of the sample. Since the laser power was concentrated at this region, the steep temperature gradient between the modified areas and the surrounding areas could lead to the formation of an internal crack that propagated to the top surface. In Figure 6.5 (c), the entire multiple foci column was focused within the sample and diffractive order +13 was at z = +20 μm (below the top surface). Since the foci were relatively far from the top surface, no scribes were formed and subsurface damage was observed instead.

A peculiar and unexpected observation was that ablation dominated scribes were formed on the bottom rough surface even before diffractive order –13 (i.e. the focus furthest away from the laser source) reached the bottom rough surface of the sample, see Figure 6.5 (d). The first and last scribes on the bottom surface were observed when diffractive order –13 was at z = +280 μm and +380

μm respectively. The types of ablation scribe formed were also either a dotted or a solid line and were rather random.

The average width of the scribes was 2.6 μm and 3.7 μm for the top and bottom surfaces respectively. The standard deviation ranges from 0.3 μm to 0.5 μm for the top surface scribes and 0.0 μm to 0.7 μm for the bottom surface scribes. The width of the scribes scanned by the OB40× lens combination was the thinnest compared to the scribes formed by the other objective lens combinations. This could be attributed to the OB40× lens having the shortest EFL, which resulted in the formation of the smallest focused spot diameter. As a result, the laser affected areas were much smaller and thus thinner scribes were formed with this objective lens.

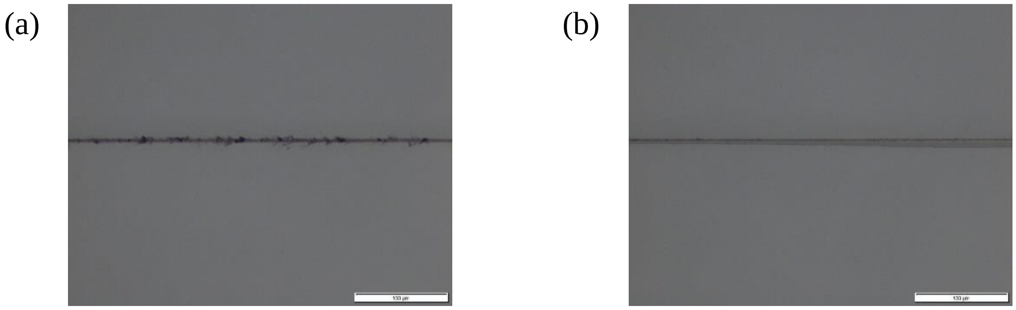

Diffractive order 0 at
z = +30 μm

Diffractive order 0 at
z = +50 μm

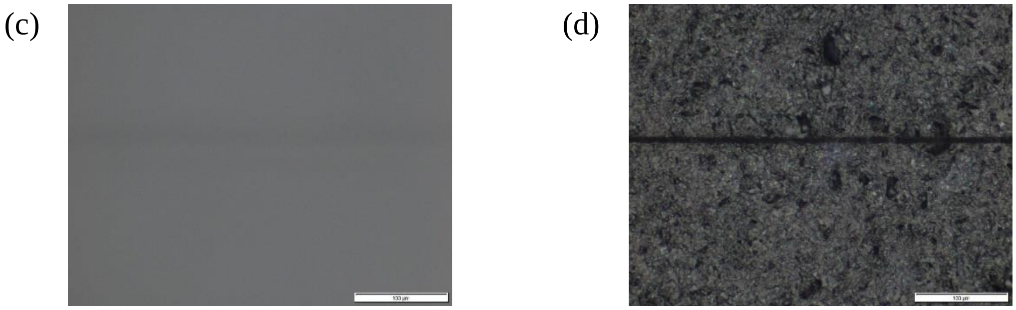

Diffractive order 0 at
z = +90 μm

Diffractive order 0 at
z = +250 μm

Figure 6.5 Optical images of scribes on (a, b and c) top and (d) bottom surfaces for MF laser irradiation with OB40× lens

6.3 Single section scanning with multiple foci

A test to demonstrate that the MF lens with multiple foci could be simultaneously focused within the sample was conducted. In this section, the 27 foci lens was paired with the OB40× lens. The OB40× lens was chosen as it produced a total foci separation that was much smaller than the thickness of the sample (i.e. 136.3 μm and 430 μm respectively). Sample C, with a top polished surface and a bottom rough surface, was used in the experiments. The single scan in one section of the sample allowed the multiple foci to modify only a section of the sample thickness, while leaving the remaining areas untouched, see Figure 4.9 of Section 4.2.3.4. After mechanical cleavage, the sidewall profile with the modified and unmodified sections could be studied.

The laser scanned the samples at the highest possible power of 0.80 W. This value was selected as it would provide the highest possible power density to the sample. This gave the best probability of nonlinear absorption within the sample for internal modification for subsequent mechanical cleavage. The effect of energy deposition within the sample on the scribe characteristics was investigated by having different laser scanning speeds for each of the experiments, namely 0.1 mm/s, 1 mm/s and 10 mm/s.

The amount of energy deposited can be derived:

$$E_d = QN \tag{6.2}$$

$$= \frac{P}{R_p} \times \frac{R_p \phi}{v}$$

$$E_d = \frac{P\phi}{v} \tag{6.3}$$

Where E_d is the energy deposited within the sample, Q is the pulse energy, N is the number of pulses overlap, P is the average power, R_p is the pulse repetition rate, ϕ is the focused spot diameter and v is the laser scanning speed.

Equation 6.3 indicated that the energy deposited into the sample was independent of the pulse repetition rate and was dependent on the scanning speed, assuming that other parameters were kept constant. The scanning speeds selected were much slower than that used in Section 5.4, i.e. 240 mm/s. This drastic reduction in scanning speed was to account for the reduction in overall laser power and the power allocated to each focus. Therefore, the slower scanning speeds was to allow sufficient energy to accumulate within the sample to facilitate the occurrence of nonlinear absorption, assuming that the intensity of the foci was high enough.

Table 6.3 shows the relationship between the scanning speed and the energy deposition to the sample.

Table 6.3 Relationship between scanning speed and energy deposition for laser power of 0.80 W

Scanning speed (mm/s)	0.1	1	10
Energy deposition (mJ)	10.2	1.0	0.1

6.3.1 Observation of sample surfaces after irradiation

6.3.1.1 Scanning of the upper section

Laser irradiation of the upper section had diffractive order +13 (i.e. the focus closest to the laser source) and was just 2 μm away from the top surface. With a Rayleigh length of 0.94 μm, the distance to the top surface was further reduced. This allowed the foci to interact with the top polished surface for visible scribe formation.

A 5.6 μm thick crack dominated scribe was formed on the top polished surface, with a standard deviation of 0.4 μm. Large uncontrollable cracks deviated away from the scanning direction were observed on the top surface at a scanning speed of 0.1 mm/s, see Row 1 Column A of Table 6.4. This could be attributed to an excess of energy deposition into the sample. The excess energy further heated the sample and induced the formation of internal cracks. Excess energy was channeled to the propagation of cracks that deviated from the scanning direction. Even though the foci were focused at the upper section, due to the uncontrolled crack formation, the cracks at the upper section could extend towards the bottom rough surface. Consequentially, a curved crack was observed on the bottom surface, see Row 2 Column A of Table 6.4.

At a moderate scanning speed of 1 mm/s, less energy was deposited into the sample. Although the energy deposited was much lower, it was still in excess. Hence, a 6.3 μm thick crack dominated scribe was observed on the top polished surface, with a standard deviation of 1.0 μm, see Row 1 Column B of Table 6.4. The excess energy mostly formed internal cracks and propagated the cracks to the top surface. As such, small cracks around the ablation scribes were observed on the top surface. Occasionally, when the energy deposited in that area was slightly higher, longer cracks that deviated from the scanning direction were observed as a result of the highly sensitive nature of the experiment. Since the energy deposition at 1 mm/s scanning speed was lower than that at 0.1 mm/s, the cracks on the top surface were much shorter at the 1 mm/s scanning speed. At this scanning speed, it was still possible for the cracks to extend to the lower section of the sample. Hence, very faint and short cracks could be observed on the bottom rough surface, see Row 2 Column B of Table 6.4.

A 6.5 μm thick crack dominated scribe was formed on the top polished surface, with a standard deviation of 0.4 μm. Shorter and smaller cracks were formed around the scribe when the sample was irradiated at a scanning speed of 10 mm/s, see Row 1 Column C of Table 6.4. Occasional crack deviation was observed. Unlike the cracks formed at the slower scanning speeds, these cracks were shorter and ran almost parallel to the scanning direction. Due to the lower energy deposited, there was not enough excess energy to extend the cracks to the lower section of the sample. Therefore, there were no visible scribes or cracks observed on the bottom rough surface of the sample, see Row 2 Column C of Table 6.4.

Table 6.4 Optical images of samples' surfaces after 27 foci irradiation using OB40× lens at different scanning speeds for upper section scans

	Scanning speed		
	0.1 mm/s *Column A*	**1 mm/s** *Column B*	**10 mm/s** *Column C*
	Upper section scan		
Top *Row 1*	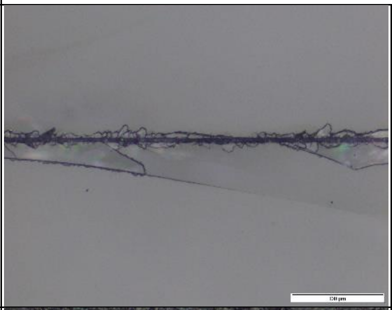	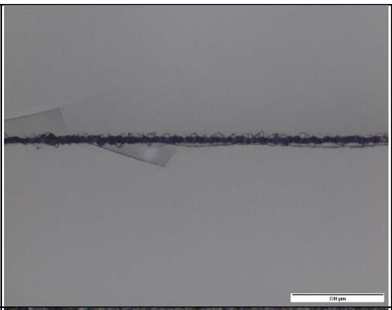	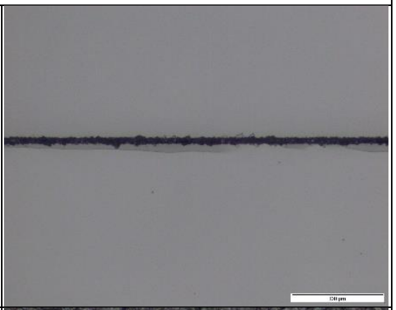
Bottom *Row 2*	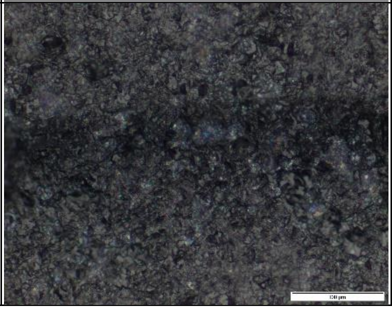	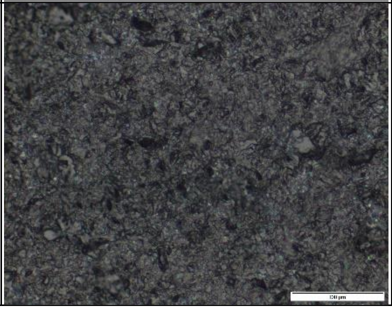	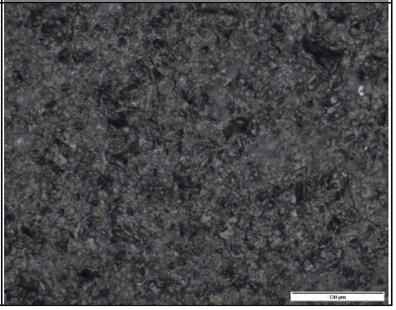

6.3.1.2 Scanning of the middle section

When the multiple foci were focused at the middle section, there were no visible scribes observed on the top polished surface. It was impossible for the multiple foci to interact with the top surface of the sample to form scribes due to the large distance between the foci and the top surface. Instead, some subsurface damage could be observed on the top surface for all scanning speeds. The sample irradiated with the slowest scanning speed of 0.1 mm/s exhibited the most distinct subsurface damage, see Row 1 Column A of Table 6.5; the damage covered a wider area compared to the samples irradiated with the faster scanning speeds of 1 mm/s and 10 mm/s, see Row 1 Columns B and C of Table 6.5 respectively. The slower scanning speed allowed for more energy deposition to the sample. As a result, internal modification of the sample could occur to a larger extent and thus more distinct subsurface damage was observed.

Although the multiple foci were focused in the middle section and were far from the bottom rough surface of the sample, some ablation dominated scribes could be observed on the bottom surface, see Row 2 of Table 6.5. As the laser interacted with the bottom surface, a portion of the laser beam would have been internally reflected from the rough surface allowing more effective energy accumulation within this region. When sufficient energy was accumulated, an ablation scribe was formed on the bottom surface. With increasing scanning speed, there was less energy deposition within the sample and thinner scribes were observed. The average widths of the scribes decreased from 14.4 μm to 1.3 μm, with the standard deviation ranging from 0.3 μm to 1.7 μm.

Table 6.5 Optical images of samples' surfaces after 27 foci irradiation using OB40× lens at different scanning speeds for middle section scans

	Scanning speed		
	0.1 mm/s *Column A*	**1 mm/s** *Column B*	**10 mm/s** *Column C*
	Middle section scan		
Top *Row 1*			
Bottom *Row 2*	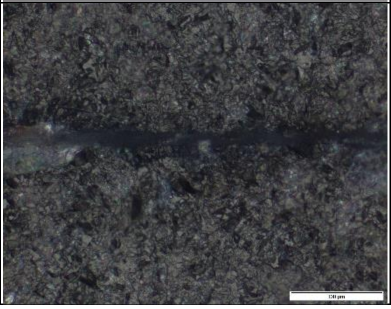	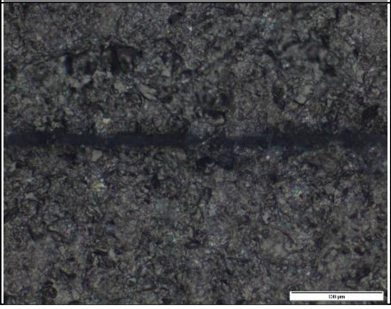	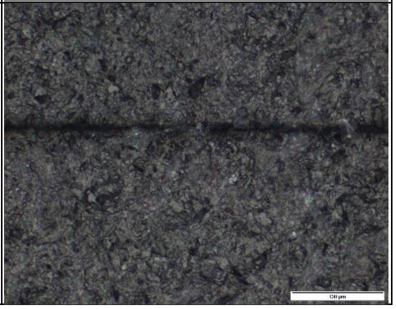

6.3.1.3 Scanning of the lower section

When the multiple foci were focused at the lower section, neither visible scribes nor subsurface damage could be observed on the top polished surface, see Row 1 of Table 6.6. This was because the laser energy was focused too far away from the top surface to observe any visible modifications.

With the multiple foci focusing at the lower section, intuitively one would expect that ablation scribes would be observed on the bottom sample surface. However, no visible scribes were observed for any scanning speed, see Row 2 of Table 6.6. A possible explanation was that significant amount of the laser energy had been linearly absorbed by the bulk thickness as the light was propagating to the lower section. By the time the laser beam was focused at the lower section, the loss of laser energy through linear absorption by the bulk of the sample meant that there was insufficient energy to cause any significant nonlinear absorption at the bottom surface. Even with internal reflection at the bottom surface and accumulation of energy within this region, there was still insufficient energy for scribes to form.

Table 6.6 Optical images of samples' surfaces after 27 foci irradiation using OB40× lens at different scanning speeds for lower section scans

	Scanning speed		
	0.1 mm/s *Column A*	**1 mm/s** *Column B*	**10 mm/s** *Column C*
	Lower section scan		
Top *Row 1*			
Bottom *Row 2*	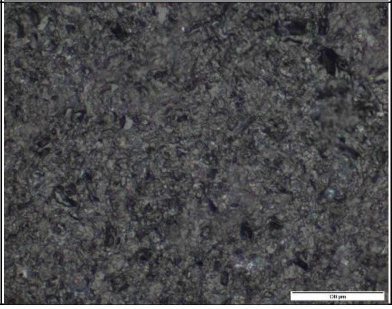	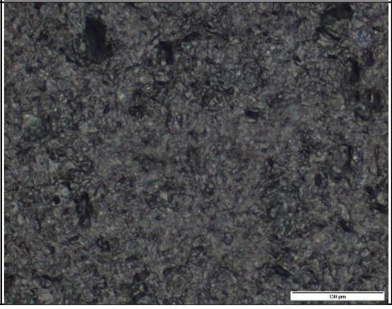	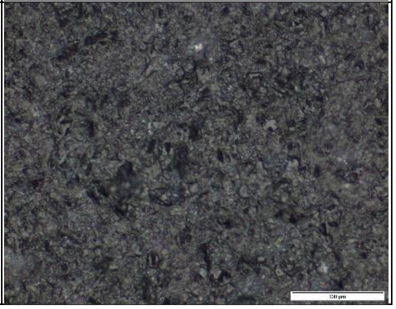

6.3.2 Mechanical cleavage of samples after irradiation

Mechanical cleavage of the samples was attempted after laser irradiation. Generally, there were three distinct observations of the sidewalls. Firstly, areas where modifications were made by the laser through nonlinear absorption resulted in uneven distortions forming the roughened sidewall. Secondly, cracked areas from interaction with the laser formed non-uniform waves on the sidewall. Lastly, areas that were neither modified nor cracked by the laser formed smooth surfaces after mechanical cleavage.

6.3.2.1 Scanning of the upper section

When the laser was focused at the upper section, samples that were scanned at 0.1 mm/s and 1 mm/s scanning speeds were successfully cleaved, see Columns A and B of Table 6.7 respectively. However, mechanical cleavage was not possible for samples that were irradiated with a scanning speed of 10 mm/s, see Column C of Table 6.7.

The depth of internal modification was about 141 μm, with a standard deviation of 12 μm, for the sample irradiated at the upper section with a scanning speed of 0.1 mm/s. However, large wave-like cracks and inconsistent modification region were observed, see Column A of Table 6.7. A probable cause could be that the excess energy deposited into the sample resulted in the formation of the large internal cracks. These internal cracks obstructed the regular propagation of the laser along the optical axis. Since the laser was unable to properly focus at the intended foci positions, the intensity at these positions would be lower than expected. As a result, nonlinear absorption was not guaranteed in these areas. With only linear absorption, the formation of consistent internal modifications was prevented in the section. Furthermore, there were some modifications observed near the bottom surface of the sample. The presence of these structures provided an explanation on the crack observed (which was not present for the other scanning speeds) in the optical images of the bottom surface in Row 2 of Table 6.4.

When the sample was irradiated with a scanning speed of 1 mm/s, the depth of modification was 123 μm, with a standard deviation of 8 μm, see Column B of Table 6.7; this was similar to that of the sample irradiated with a scanning speed of 0.1 mm/s. With a moderate scanning speed, it provided a shorter time for the laser to interact with the sample and less energy was deposited. There was less excess energy to form internal wave-like cracks. This allowed the beam to continue propagating along the optical axis with less obstructions. Since the laser exhibited less scattering of light, the depth of modification was shorter and the internal modifications by the laser were more consistent.

Even though there was a scribe observed on the top surface for the sample irradiated with a scanning speed of 10 mm/s, mechanical cleavage was unsuccessful, see Column C of Table 6.7. A faster scanning speed translated into a shorter time period for the laser to interact with the sample. This resulted in lower energy deposited into the sample, and thus inadequate internal modification and weakening of the sample. Thus, mechanical cleavage of the sample was unsuccessful.

Table 6.7 Optical images of samples' sidewall profiles after 27 foci irradiation using OB40× lens at different scanning speeds for upper section scans

	Scanning speed		
	0.1 mm/s *Column A*	**1 mm/s** *Column B*	**10 mm/s** *Column C*
	Upper section scan		
Sidewall	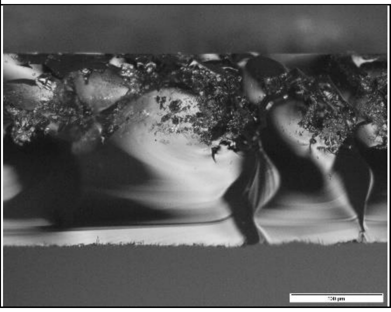	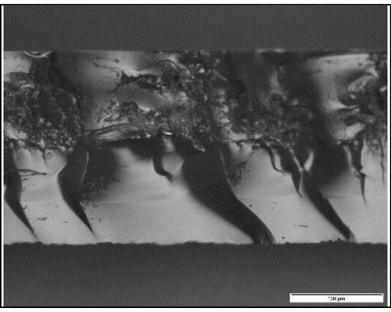	No cleavage

6.3.2.2 Scanning of the middle section

Similarly to laser irradiation of the upper section, mechanical cleavage was successful when the samples were irradiated at the middle section with a scanning speed of either 0.1 mm/s or 1 mm/s, see Columns A and B of Table 6.8 respectively. Similar to previous observations, the sample irradiated with a scanning speed of 10 mm/s could not be cleaved, see Column C of Table 6.8.

The sidewall profiles of the cleaved samples at the slower scanning speeds were rather similar. There appeared to be two distinct types of modification regions. The first modification region was closer to the top surface. This region had larger, more consistent and dense modifications; some wave-like cracks could be detected above the modification region. The second modification region was located just below the first region and was closer to the bottom rough surface. In this region, smaller modifications that were less consistent and sparse were observed. The depth of the first and second modification regions was about 120 μm and 54 μm respectively. The standard deviation ranges from 6 μm to 7 μm for the first region and 2 μm to 4 μm for the second region. The formation of these different modification regions could well depend on the amount of laser energy absorbed by the sample at these regions.

It was highly probable that the first modification region was produced directly by the incoming laser beam when it was focused at the various multiple foci positions. Since the sample was absorbing energy directly from the laser, the energy deposited and accumulated within this region was high; this enabled the formation of large and more consistent modifications. Thus, large wave-like cracks were formed as a result of the excess energy deposited.

The second modification region could have been produced after internal reflection at the bottom rough surface. The internally reflected light would have a lower energy as a portion of light would have been refracted out of the sample. Interaction between the incoming laser beam and the internally reflected laser beam resulted in the accumulation of energy in this region. Due to the low laser energy in this region, it was more difficult to accumulate sufficient energy to modify the sample. Hence, smaller and less consistent modifications were observed. The presence of these modifications demonstrated that energy could be accumulated near the bottom surface and provided an explanation for the scribes observed on the bottom surface of the samples.

Some modifications were observed near the top surface of the sample that was irradiated with a scanning speed of 0.1 mm/s, see Column A of Table 6.8. These modifications explained the formation of the more distinct subsurface damage observed on the top surface.

At a scanning speed of 1 mm/s, there was less energy deposited within the sample. The sidewall profile was observed to have more uniform internal modifications in both regions with shorter internal cracks, see Column B of Table 6.8. There were no other modifications observed near the top surface. This verified the observation of a less distinct subsurface damage on the top polished surface.

Although subsurface damage and bottom scribes were observed, the sample irradiated at 10 mm/s scanning speed could not be successfully cleaved, see Column C of Table 6.8. The low amount of energy deposited was insufficient to modify and weaken the sample for cleaving.

Table 6.8 Optical images of samples' sidewall profiles after 27 foci irradiation using OB40× lens at different scanning speeds for middle section scans

	Scanning speed		
	0.1 mm/s *Column A*	**1 mm/s** *Column B*	**10 mm/s** *Column C*
	Middle section scan		
Sidewall	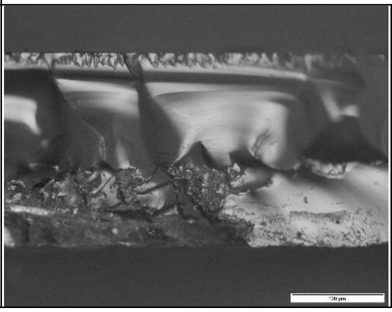	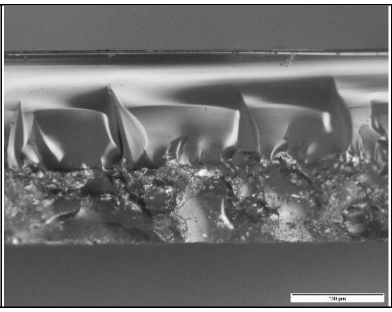	No cleavage

6.3.2.3 Scanning of the lower section

When the multiple foci were focused at the lower section, mechanical cleavage was not possible for all scanning speeds, see Table 6.9. As mentioned previously, most of the laser energy could have been linearly absorbed by the bulk thickness before the formation of the multiple foci. By the time the laser was focused at the intended multiple foci positions, it did not have sufficient amount of energy to interact with the sample for nonlinear absorption to occur. Even with the extra boost in energy from the internally reflected light energy from the bottom rough surface, the energy accumulated was still inadequate for internal modification to sufficiently weaken the sample for cleavage.

Table 6.9 Optical images of samples' sidewall profiles after 27 foci irradiation using OB40× lens at different scanning speeds for lower section scans

	Scanning speed		
	0.1 mm/s *Column A*	**1 mm/s** *Column B*	**10 mm/s** *Column C*
	Lower section scan		
Sidewall	No cleavage	No cleavage	No cleavage

6.4 Multiple foci scanning with conventional focusing lenses

Experiments in Section 6.2 employed a 27 foci MF lens that was paired with objective lenses with large power attenuation. For a fair comparison between the different objective lens combinations, the optics combination that exhibited the largest attenuation dictates the maximum "effective" laser power delivered to a sample, which was lower due to the attenuation. However, due to the low laser power employed for irradiation, the energy deposited into the samples was insufficient for mechanical cleavage and the sidewall profiles of the samples after cleavage could not be studied. The results obtained were limited and the true potential of the multiple foci laser irradiation could not be fully investigated.

In Section 6.3, the 27 MF lens was paired with the OB40× lens, with all 27 foci focused within the sample. Due to the short EFL of the objective lens, the foci separation was short and the laser power was only concentrated in a section of the sample's thickness. The large concentration of energy with high intensity in a small section led to the formation and deviation of cracks along the scanning direction. As such, some samples could be mechanically cleaved and the sidewall profiles were studied.

In this section, experimental investigation was carried out to address the above limitations of the previous studies. This study explored the distribution of laser power over different number of foci through the use of 9 foci and 27 foci MF lenses. Each MF lens was paired with carefully selected conventional focusing lens with an appropriate EFL that could spread the foci such that the total foci separation was just slightly less than the sample’s thickness. This ensured that all foci produced by the optics would be focused within a sample and that the laser power would be fully utilized and deposited into the sample.

Since the foci were spread out, the laser power would not be concentrated at a certain section but more evenly distributed within a sample. This provided a gentle temperature gradient between the areas that were directly irradiated by the laser and the surrounding areas. Hence, there will be a lower probability for the formation and deviation of cracks. Since the multiple foci were spaced apart, if the intensity was sufficiently high, each focus could interact with the sample through nonlinear absorption. When there was sufficient energy accumulated within the sample, internal modification at various focus positions led to the formation of a roughened sidewall. Additionally, the internal modifications could weaken the sample at the various focal positions to further encourage complete mechanical cleavage of the sample.

This investigation explored the effect of changing the scanning speed and pulse repetition rate on the irradiation characteristics of the samples. The most appropriate scanning speed and pulse repetition rate for successful mechanical cleavage would be determined.

In Section 6.3, it was found that the energy deposited to the sample was independent of the repetition rate. Energy deposition depended on the power and scanning speed. Therefore, with the same power and the same scanning speed, the energy deposited to the sample would theoretically remain the same. In contrast, having the same pulse repetition rate but changing the scanning speed would provide the same pulse energy but the amount of energy deposited to the sample would be different.

This investigation was to understand the order of magnitude of the various laser parameters for facilitating a successful cleavage of multiple foci laser irradiated sapphire samples. The values were increased by an order of magnitude for each iteration such that the results obtained were more distinct and more definitive conclusions could be drawn.

The experiments were conducted with three pulse repetition rates of 50 kHz, 500 kHz and 5.12 MHz. 50 kHz was selected as the lowest pulse repetition rate as this was the lowest setting the laser could provide and produced the highest peak power. 5.12 MHz was chosen as the laser was unable to produce a pulse repetition rate of 5 MHz exactly. A high repetition rate would result in low peak power. The experiments were conducted with three scanning speeds of 0.1 mm/s, 1 mm/s and 10 mm/s. The scanning speed of 100 mm/s was not selected as the energy deposited within the samples would likely be insufficient to weaken the samples for subsequent mechanical cleavage.

In the previous studies, the highest peak power was employed as it would provide a higher probability for nonlinear absorption to modify and weaken the sample for mechanical cleavage. However, the samples may not require such high peak powers for cleavage and an excess of energy would result in undesirable crack formation and deviation. A moderate pulse repetition rate could have been optimal to ensure a successful cleavage of samples while minimizing crack formation and deviation.

6.4.1 Laser power selection

Commercially available conventional focusing lenses were chosen that were specifically designed to have a working range containing the 1064 nm laser wavelength. As a result, the power attenuation of the focusing lens was much lower and more of the laser power could be harnessed for laser irradiation of the samples.

Even though the conventional focusing lens had less power attenuation, there was still a slight difference in laser power transmitted for different optic combinations. For a fair comparison between results, the laser power levels were adjusted accordingly such that similar amount of power would be deposited into the sample regardless of the optic combination. Figure 6.6 presents the variation in power transmitted through both sets of MF and focusing lenses combination. Since the 27 foci MF lens paired with an EFL of 7.5 mm focusing lens exhibited a higher power attenuation, laser power of 1.13 W was selected for subsequent experiments.

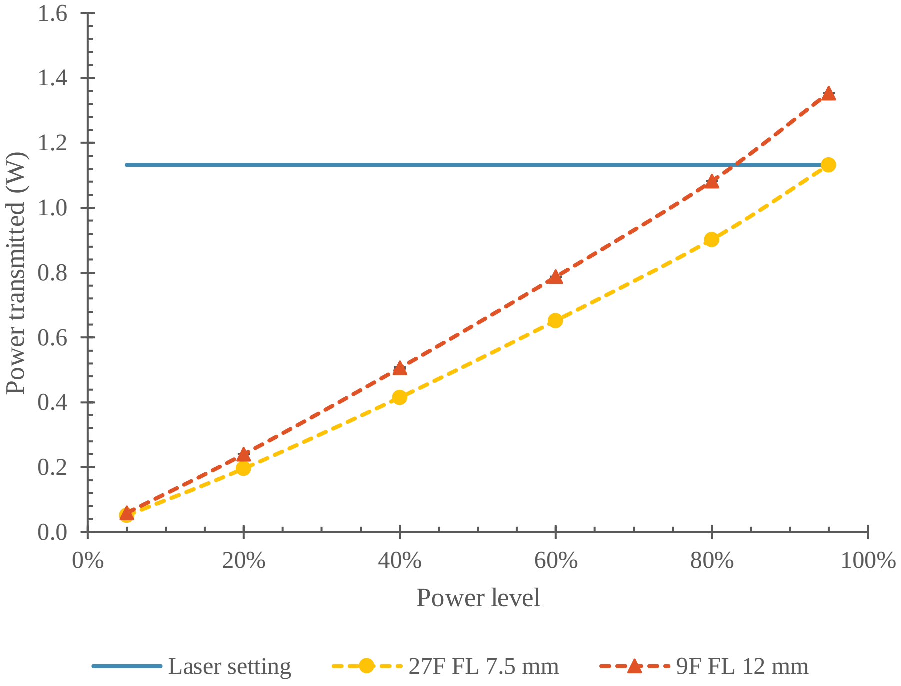

Figure 6.6 Power transmitted for combination of MF and FL optics for single zone scanning without any samples The standard deviation ranges from 0.000 W to 0.004 W

As the laser power was kept constant for the experiments, the total pulse energy delivered by the laser to the sample was only dependent on the pulse repetition rate of the laser and the relationship between the two parameters is presented in Table 6.10. The pulse energy was distributed among the multiple foci. The amount of pulse energy allocated to a single focus was dependent on the number of foci formed by the MF lens. Each focus of the 9 foci setup would have approximately three times the energy of a single focus of the 27 foci setup. Therefore, it was possible to study if it was more favorable to split the laser energy into more foci that were spaced closer together or to have fewer foci, each with more power, but were spaced further apart.

As the laser power was kept constant, the energy deposition depended on both the focused spot diameter and the laser scanning speed. Depending on the EFL of the focusing lens employed, the focused spot diameter changed accordingly. The relationship between the scanning speed, the EFL of the focusing lens and the energy deposition within the sample is tabulated in Table 6.11. Regardless of the combinations of optics, the number of foci and the corresponding total foci separation, diffractive order 0 was positioned at the midplane where $z = +210\ \mu$m, see Figure 4.10 in Section 4.2.3.5. Sample *C*, with a top polished surface and a bottom rough surface, was used in the experiments.

Table 6.10 Relationship between pulse repetiotion rate and pulse energy for laser power of 1.13 W

Pulse repetition rate (kHz)		50	500	5120
Pulse energy (μJ)		22.6	2.26	0.221
Energy of a single focus (μJ)	**27 foci**	0.839	0.084	0.008
	9 foci	2.52	0.252	0.025

Table 6.11 Relationship between scanning speed and energy deposition for laser power of 1.13 W

Scanning speed (mm/s)		0.1	1	10
Energy deposition (mJ)	**27 foci (EFL = 7.5 mm)**	24.9	2.49	0.249
	9 foci (EFL = 12 mm)	39.9	3.99	0.399

6.4.2 27 foci irradiation with a 7.5 mm EFL focusing lens

This section contains the results for samples irradiated by a 27 foci MF lens and a focusing lens with a 7.5 mm EFL. The focused spot diameter at the focal length was 2.20 μm. The pulse repetition rates and scanning speeds were varied. Optical images of the top and bottom surfaces of the samples after irradiation were studied. In addition, the sidewall profiles were studied if the samples could be cleaved after irradiation.

6.4.2.1 Pulse repetition rate of 50 kHz

For a pulse repetition rate of 50 kHz, all scanning speeds registered some form of crack formation and the occasional subsurface damage on the top polished surface, see Row 1 of Table 6.12. The subsurface damage observed was a result of internal modification in the sample by multiple foci irradiation. Ablation dominated scribes were observed at the bottom rough surface for all scanning speeds, see Row 2 of Table 6.12. The ablation scribes had similar widths that were about 12.9 μm thick. The standard deviation ranges from 0.4 μm to 2.8 μm. No crack dominated scribes were observed on either the top or the bottom surface.

At a 0.1 mm/s scanning speed, there appears to be an excess in energy deposited into the sample. A portion of the energy deposited in the sample was nonlinearly absorbed forming internal modifications. Consequently, the excess energy deposited induced the formation of internal cracks and propagated these cracks to the top polished surface of the sample. The excess energy led to a large deviation of cracks from the scanning direction. Subsurface damage was observed on the top surface, see Row 1 Column A of Table 6.12.

At a 0.1 mm/s scanning speed, a thick ablation dominated scribe was observed on the bottom rough surface surrounded by cracks, see Row 2 Column A of Table 6.12. With internal reflection at the bottom rough surface, sufficient accumulation of energy in this region resulted in the formation of an ablation scribe. Adjacent to the ablation scribe, cracks that had large deviations from the scanning direction were observed. The presence of cracks on the bottom surface could have been formed in a similar manner as the cracks found on the top surface. The excess energy accumulated within the region propagated the internal cracks to the bottom surface of the sample.

The sample irradiated with a 0.1 mm/s scanning speed was mechanically cleaved and the optical image of the sidewall profile of the sample was studied. In the optical image, it appeared that the modifications in upper section was in the focal plane of the camera lens, whereas the modifications in the lower section appeared to be out of focus, see Row 3 Column A of Table 6.12. This meant that the plane of cleavage was not perfectly perpendicular to the top and bottom surfaces of the sample. An explanation for the uneven plane of cleavage could be due to the random formation of internal cracks as a result of excess energy deposition within the sample. Indeed, mechanical cleavage would follow the path of least resistance and tend to propagate in the direction of the weakened path with internal cracks instead of the plane of laser modification. Since the cracks were formed randomly, the plane of cleavage was not perfectly perpendicular to the sample’s surfaces.

When a 1 mm/s scanning speed was utilized, energy from the laser induced the formation of internal modifications and internal cracks. Excess energy was channeled to the propagation of the internal cracks to the top polished surface. The lower amount of energy deposition reduced the extent of crack deviation; the cracks formed on the top surface were almost parallel to the scanning direction. Subsurface damage was observed on the top surface, see Row 1 Column B of Table 6.12.

At a 1 mm/s scanning speed, only an ablation scribe was observed on the bottom rough surface, see Row 2 Column B of Table 6.12. Internal reflection of light encouraged by the bottom rough surface allowed the accumulation of energy for the formation of ablation dominated scribes. Since energy was not excessively in excess, the internal cracks did not extend to the bottom surface.

The sample irradiated with a 1 mm/s scanning speed could be cleaved. The sidewall profile presented a plane of cleavage that appeared to be along, or closer to, the plane of laser modification, see Row 3 Column B of Table 6.12. With the moderate scanning speed, there was less energy in excess to form large internal cracks within the sample. When pressure was applied to the sample, the separation crack was inclined to propagate along the plane of laser modification. Since the plane of cleavage was along the plane of laser modification, the sidewall profile could be better studied. The roughened sidewall profile appeared to contain non-uniform modifications. Although there was no formation of large internal cracks, the energy deposition in the sample was sufficient to form smaller cracks that were closer to the laser modified areas. As such, the sidewall profile observed could be a combination of both the laser modified areas and small internal cracks.

The fastest scanning speed of 10 mm/s resulted in less energy deposition into the sample. Even with the reduction in energy deposition, there was still sufficient energy for the formation of a thin crack on the top polished surface, see Row 1 Column C of Table 6.12. The lower energy deposited did not result in any deviation of the crack. In fact, the crack was observed to be largely parallel to the scanning direction. There were minimal signs of subsurface damage on the top surface due to the reduction in the amount of energy deposition in the sample.

Internal reflection at the bottom rough surface enabled the accumulation of energy within the region, such that an ablation dominated scribe could be formed on the bottom surface of the sample scanned by a scanning speed of 10 mm/s, see Row 2 Column C of Table 6.12.

Although subsurface damage was observed on the top polished surface and ablation scribe formed on the bottom rough surface, mechanical cleavage was not possible when the fastest scanning speed of 10 mm/s was utilized, see Row 3 Column C of Table 6.12. Even though sufficient energy was deposited into the sample for internal modification and ablation scribe formation on the bottom surface, it was ineffective to weaken the sample sufficiently for subsequent mechanical cleavage. This illustrated that the presence of internal modification and scribe formation on the sample’s surfaces did not mean that a successful mechanical cleavage of the sample was guaranteed.

Table 6.12 Optical images of samples after irradiation with 27 foci and a focusing lens of 7.5 mm EFL at a pulse repetition rate of 50 kHz with various scanning speeds

	Scanning speed		
	0.1 mm/s *Column A*	**1 mm/s** *Column B*	**10 mm/s** *Column C*
	R_p = 50 kHz		
Top *Row 1*	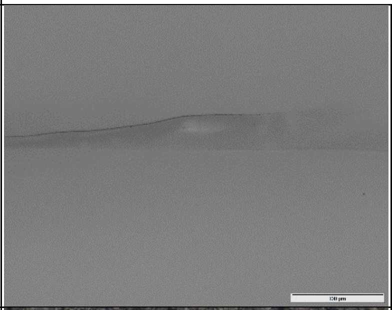	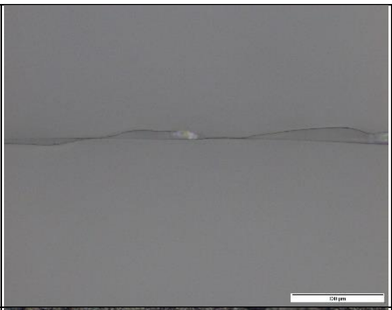	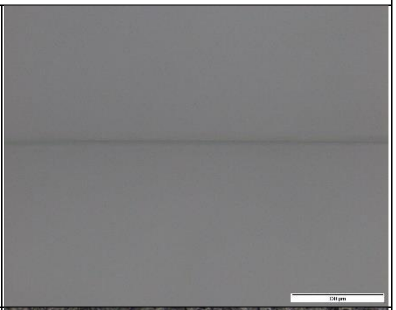
Bottom *Row 2*	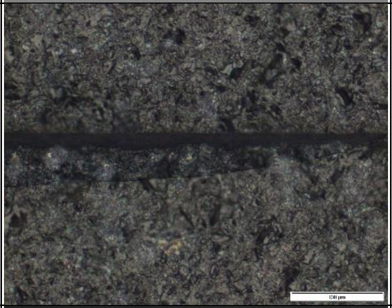	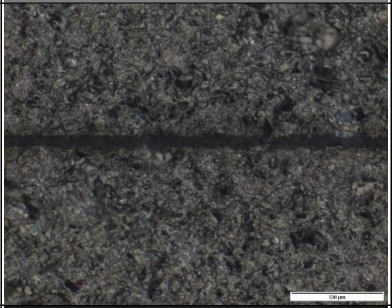	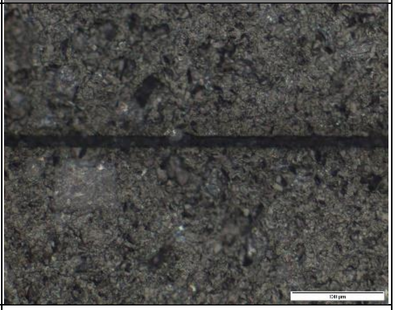
Sidewall *Row 3*	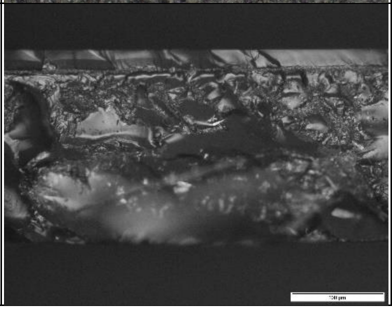	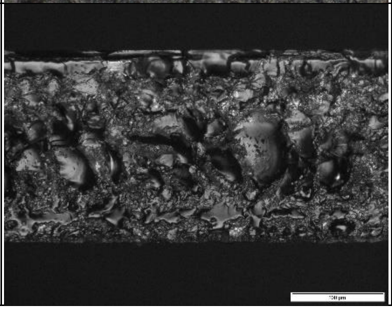	No cleavage

6.4.2.2 Pulse repetition rate of 500 kHz

When a 500 kHz pulse repetition rate was employed, there were no cracks, scribes or subsurface damage observed on the top polished surface for all scanning speeds, see Row 1 of Table 6.13. The higher pulse repetition rate resulted in a lower pulse energy and a lower peak power. There was insufficient energy to induce large scale nonlinear absorption within the sample for internal modification or crack formation and thus subsurface damage was not observed. Likewise, the lower pulse energy was insufficient to form scribes or cracks on the top surface.

On the bottom rough surface, as a result of internal reflection and energy accumulation, very thin ablation dominated scribes were observed for all scanning speeds, see Row 2 of Table 6.13. Cracks were absent on the bottom surfaces of the samples. The widths of the ablation scribes were similar with an average width of 3.2 μm for all scanning speeds. The standard deviation ranges from 0.4 μm to 0.6 μm. As the scanning speed increased, the consistency of scribe formation reduced. At a 0.1 mm/s scanning speed, the ablation scribe was continuous, see Row 2 Column A of Table 6.13. When the scanning speed was increased to 10 mm/s, the scribes were discontinuous, see Row 2 Column C of Table 6.13. This could be attributed to the reduction of energy deposition into the sample at the faster scanning speed. Even with internal reflection at the bottom surface, there were instances whereby the accumulation of energy was insufficient in the scanning direction. The areas where sufficient energy was accumulated resulted in scribe formation, while the areas with insufficient energy accumulation had no scribes.

Mechanical cleavage could not be performed on the samples irradiated with a 500 kHz pulse repetition rate at any scanning speed, see Row 3 of Table 6.13. Without large scale nonlinear absorption within the samples, weakening of the samples were ineffective for subsequent cleavage. As such, no samples could be mechanically cleaved and the sidewall profiles of the samples could not be studied.

Table 6.13 Optical images of samples after irradiation with 27 foci and a focusing lens of 7.5 mm EFL at a pulse repetition rate of 500 kHz with various scanning speeds

	Scanning speed		
	0.1 mm/s *Column A*	**1 mm/s** *Column B*	**10 mm/s** *Column C*
	R_p = 500 kHz		
Top *Row 1*			
Bottom *Row 2*	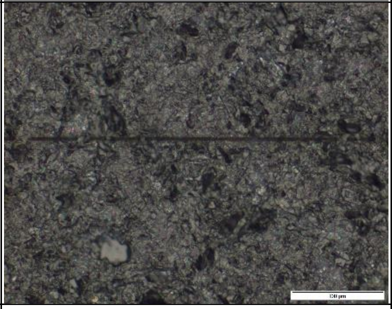	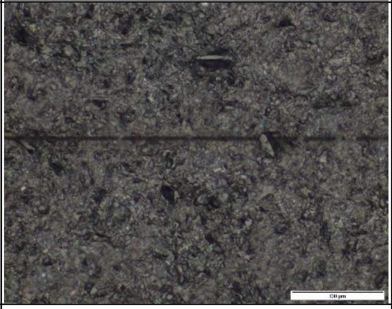	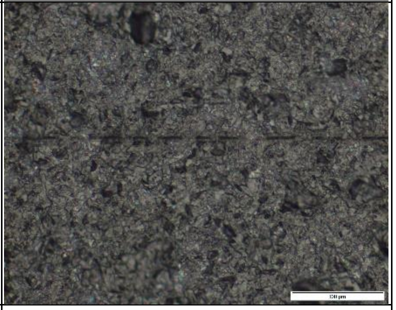
Sidewall *Row 3*	No cleavage	No cleavage	No cleavage

6.4.2.3 Pulse repetition rate of 5.12 MHz

When the samples were irradiated with the highest pulse repetition rate of 5.12 MHz, cracks and scribes were absent on both surfaces for all scanning speeds, see Rows 1 and 2 of Table 6.14. In addition, no subsurface damage was observed on the top polished surface. The lack of visible changes could be attributed to the high pulse repetition rate resulting in a low pulse energy and low peak power. The low peak power was likely to be insufficient to induce nonlinear absorption within the sample for modification, and thus only linear absorption occurred. Since there was insufficient energy deposition to effectively weaken the samples, mechanical cleavage could not be performed on all samples, see Row 3 of Table 6.14.

Table 6.14 Optical images of samples after irradiation with 27 foci and a focusing lens of 7.5 mm EFL at a pulse repetition rate of 5.12 MHz with various scanning speeds

	Scanning speed		
	0.1 mm/s *Column A*	**1 mm/s** *Column B*	**10 mm/s** *Column C*
	R_p = 5.12 MHz		
Top *Row 1*			
Bottom *Row 2*	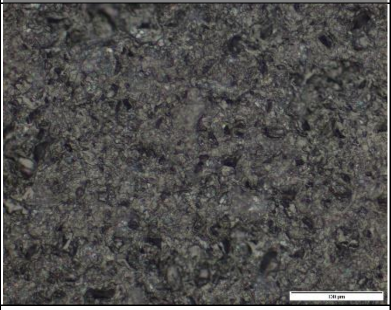	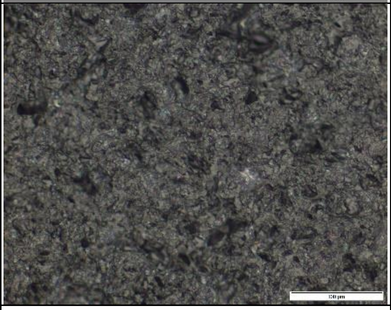	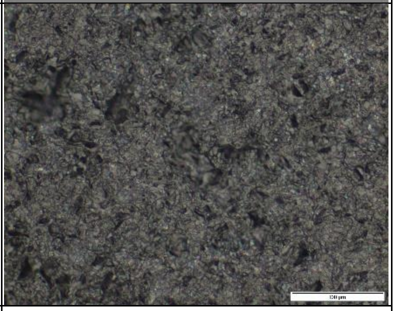
Sidewall *Row 3*	No cleavage	No cleavage	No cleavage

6.4.3 9 foci irradiation with a 12 mm EFL focusing lens

A 9 foci MF lens and a focusing lens with a 12 mm EFL was investigated. The focused spot diameter at the focal length was 3.52 μm. The pulse repetition rates and scanning speeds were varied. Optical images of the top and bottom surface of the samples after irradiation were studied. In addition, the sidewall profiles were studied if the samples could be cleaved after irradiation.

6.4.3.1 Pulse repetition rate of 50 kHz

When a 50 kHz pulse repetition rate was employed, scribes were observed on the top polished surface of the samples for all scanning speeds, see Row 1 of Table 6.15. However, the presence of visible scribes on the top surface were not expected intuitively as the total foci separation was about 20% less than the thickness of the sample (i.e. the foci were not close to the surfaces). An explanation for the presence of these scribes could be attributed to the high energy deposition. As the scanning speed was increased from 0.1 mm/s to 10 mm/s, the width of the scribes decreased from 5.8 μm to 1.3 μm. The standard deviation ranges from 0.1 μm to 0.6 μm.

Ablation dominated scribes were observed on the bottom rough surface of the samples, see Row 2 of Table 6.15. Similarly, as the scanning speed increased, the width of the scribes decreased from 10.6 μm to 6.6 μm. The standard deviation ranges from 0.4 μm to 1.9 μm. The scribes on the bottom surface were always thicker than those on the top surface for all scanning speeds employed. This could be attributed to the diffusion of light and internal reflection at the bottom rough surface. As such, with diffusion, the laser beam was incident on a larger surface area. When there was sufficient energy accumulated within this region, a thicker scribe at the bottom surface was formed.

At the slowest scanning speed of 0.1 mm/s, a crack dominated scribe was observed on the top polished surface of the sample with some deviated cracks surrounding the scribe, see Row 1 Column A of Table 6.15. Energy deposited to the sample was utilized for internal modification and crack formation within the sample. The excess energy propagated the internal cracks upwards. Since the propagation of cracks was not controlled, it led to the formation of the deviated cracks on the top surface. Internal micro-surfaces were formed as a by-product of internal crack propagation to the top surface. The presence of these micro-surfaces reflected incoming laser beam onto other micro-surfaces, thereby effectively trapping light within this region. In addition, since the laser power was now split among a smaller number of foci, the energy of a single focus was higher. A combination of both effects allowed energy accumulation near the top surface of the sample by the unfocused laser. When sufficient energy was accumulated, ablation could occur resulting in the formation of the crack dominated scribe.

At the bottom rough surface of the sample irradiated at 0.1 mm/s scanning speed, an ablation dominated scribe was observed with an absence of cracks in the surrounding area, see Row 2 Column A of Table 6.15. The ablation scribe was formed due to internal reflection at the bottom surface; this allowed energy to accumulate within this region until there was sufficient energy for ablation.

Mechanical cleavage on the sample irradiated at 0.1 mm/s scanning speed was successful and the sidewall profile was studied, see Row 3 Column A of Table 6.15. Wave-like structures were observed at the region closest to the top surface of the sample. This verified the presence of cracks observed on the top surface. Below this region contained mostly distortions produced by laser modification with small wave-like cracks. The formation of two different regions was dependent on how much energy each focus had at its focus position. Foci that were closer to the top surface of the sample had more energy at their focus positions as it had travelled a shorter distance. There was less energy lost through linear absorption by the sample. As such, there was more excess energy to form large internal cracks in addition to laser modification of the sample. Whereas for foci further from the top surface, a longer distance travelled meant that more energy was lost through linear absorption. As a result, there was less excess energy left over after modification to form large internal cracks.

With a moderate scanning speed of 1 mm/s, a crack dominated scribe was observed on the top polished surface of the sample. With a reduction in energy deposited into the sample, there was less energy in excess for the propagation of cracks to the top surface and the extent of crack deviation was much reduced, see Row 1 Column B of Table 6.15. However, the presence of the micro-surfaces near the top surface allowed for the reflection and accumulation of incoming light within this region. When sufficient energy was accumulated, the formation of a crack dominated scribe was possible.

Similarly, with a scanning speed of 1 mm/s, an ablation dominated scribe was observed on the bottom rough surface, see Row 2 Column B of Table 6.15. Due to internal reflection at the bottom surface, the accumulation of energy within the region was sufficient to form the ablation scribe.

At the fastest scanning speed of 10 mm/s, the energy deposited into the sample was just sufficient for ablation dominated scribes to form on the top polished surface of the sample, see Row 1 Column C of Table 6.15. At this scanning speed, there was insufficient energy deposited to propagate the internal cracks, if any, to the top surface of the sample. Hence, only a very thin ablation scribe was observed.

Likewise, when a scanning speed of 10 mm/s was employed, a thin ablation scribe was observed on the bottom rough surface that was formed in a similar manner to that of the other samples, see Row 2 Column C of Table 6.15.

Mechanical cleavage was unsuccessful for samples irradiated by a scanning speed of 1 mm/s and 10 mm/s, see Row 3 Columns B and C of Table 6.15 respectively. The energy deposited to the samples was insufficient to effectively weaken the sample for mechanical cleavage.

In Section 5.4, it was concluded that the formation of crack dominated scribe was the result of low power irradiation. It seemed counterintuitive here that the slower scanning speeds had crack dominated scribes on the top polished surface when there was more energy deposition into the sample. The slower scanning speeds of 0.1 mm/s and 1 mm/s could indeed have a small extent of ablation scribe formation on the top surface due to the higher energy deposition. However, it was outweighed by the effects of light reflection on the micro-surfaces near the top surface. The reflection and trapping of light in this region resulted in the accumulation of energy and thus produced the crack dominated scribes observed. Therefore, the main type of the scribes observed on the top surface of the sample was a crack dominated scribe instead of an ablation dominated scribe.

Table 6.15 Optical images of samples after irradiation with 9 foci and a focusing lens of 12 mm EFL at a pulse repetition rate of 50 kHz with various scanning speeds

	Scanning speed		
	0.1 mm/s *Column A*	**1 mm/s** *Column B*	**10 mm/s** *Column C*
	R_p = 50 kHz		
Top *Row 1*	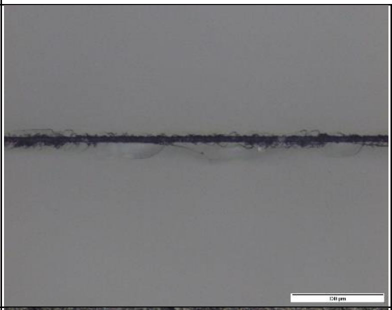	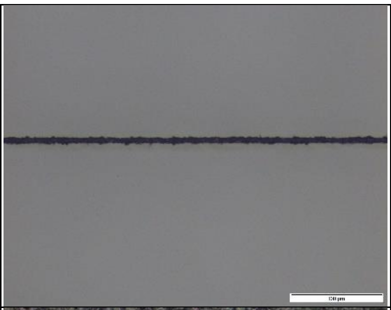	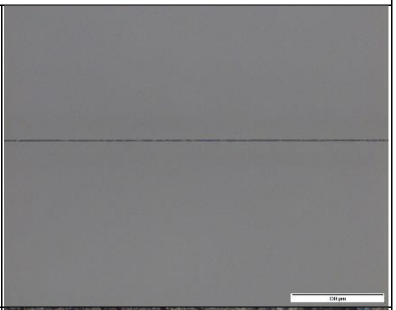
Bottom *Row 2*	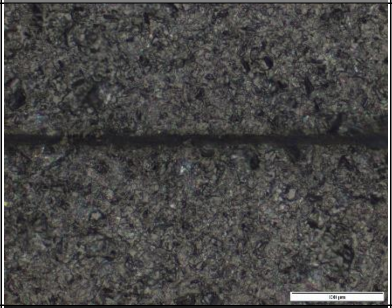	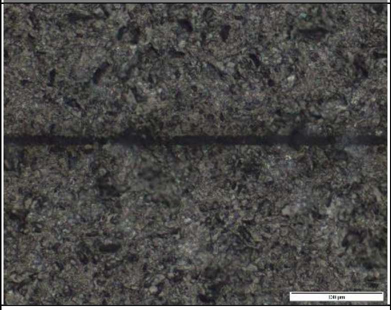	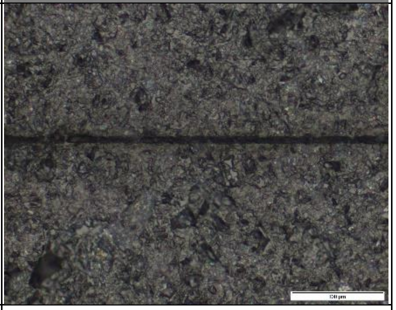
Sidewall *Row 3*	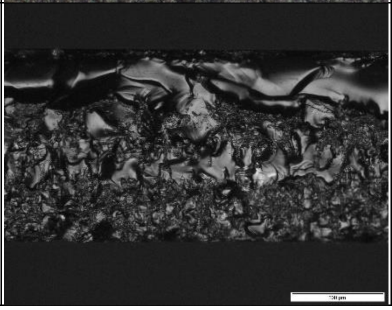	No cleavage	No cleavage

6.4.3.2 Pulse repetition rate of 500 kHz

When a 500 kHz pulse repetition rate was employed, no scribes, cracks or subsurface damage was observed on the top polished surface of the sample for all the scanning speeds, see Row 1 of Table 6.16. The higher pulse repetition rate resulted in a lower pulse energy which was unable to induce large scale nonlinear absorption within the sample. Since mostly linear absorption occurred in the sample, internal modification and crack formation was not possible and subsurface damage was not observed. The lower pulse energy was insufficient to form cracks or scribes on the top surface.

Some discontinuous ablation dominated scribes were observed on the bottom rough surface for the slower scanning speeds of 0.1 mm/s and 1 mm/s, see Row 2 Columns A and B of Table 6.16 respectively. The latter exhibited longer breaks between scribes due to less energy deposition in the sample. The average width of the scribes was about 2.9 μm, with the standard deviation ranging from 0.4 μm to 0.5 μm. No scribes were observed on the bottom surface for the fastest scanning speed of 10 mm/s, see Row 2 Column C of Table 6.16. Even with energy accumulation by internal reflection at the bottom surface, there was still insufficient energy for scribe formation.

Minimal or no internal modifications occurred within the samples for all scanning speeds. As a result, the samples were insufficiently weakened along the scan lines and thus mechanical cleavage of the samples were unsuccessful, see Row 3 of Table 6.16.

Table 6.16 Optical images of samples after irradiation with 9 foci and a focusing lens of 12 mm EFL at a pulse repetition rate of 500 kHz with various scanning speeds

	Scanning speed		
	0.1 mm/s *Column A*	**1 mm/s** *Column B*	**10 mm/s** *Column C*
	R_p = 500 kHz		
Top *Row 1*			
Bottom *Row 2*	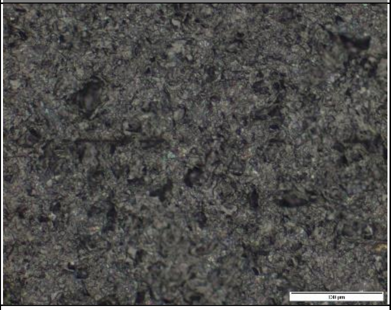	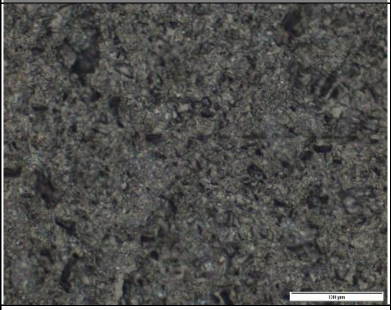	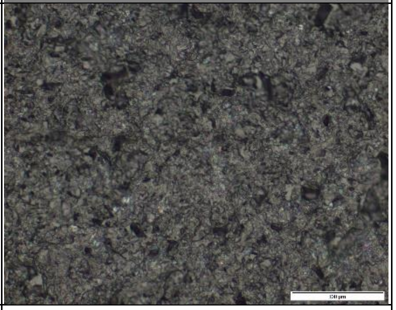
Sidewall *Row 3*	No cleavage	No cleavage	No cleavage

6.4.3.3 Pulse repetition rate of 5.12 MHz

When a 5.12 MHz pulse repetition rate was employed, no scribes or cracks was observed on either surface of the samples at any scanning speed, see Rows 1 and 2 of Table 6.17. The high pulse repetition rate produced pulses with low energy that was insufficient for nonlinear absorption in the sample and no modifications were observed. As such, mechanical cleavage could not be performed on the samples for all scanning speeds, see Row 3 of Table 6.17.

Table 6.17 Optical images of samples after irradiation with 9 foci and a focusing lens of 12 mm EFL at a pulse repetition rate of 5.12 MHz with various scanning speeds

	Scanning speed		
	0.1 mm/s *Column A*	**1 mm/s** *Column B*	**10 mm/s** *Column C*
	R_p = 5.12 MHz		
Top *Row 1*	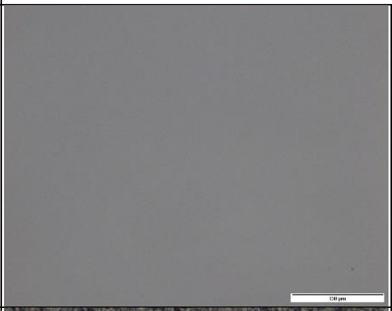	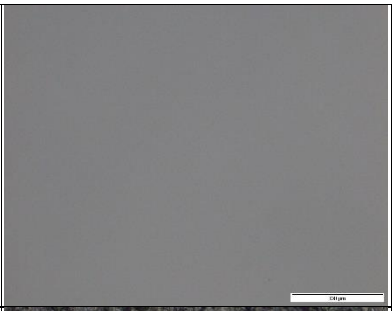	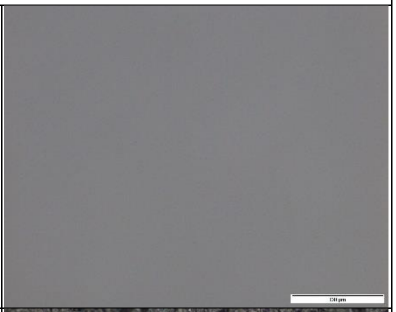
Bottom *Row 2*	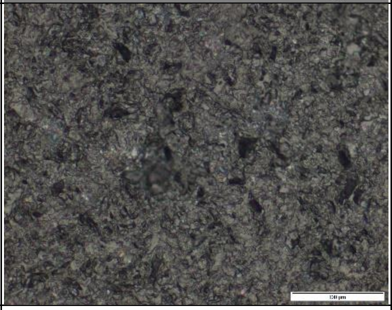	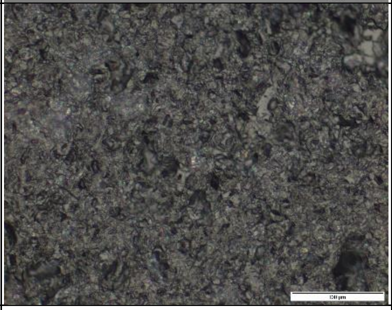	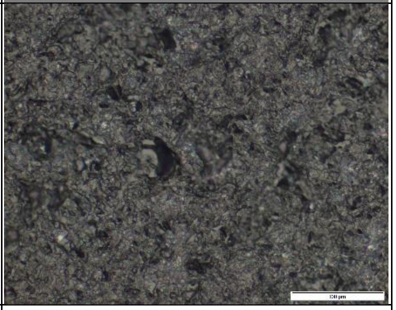
Sidewall *Row 3*	No cleavage	No cleavage	No cleavage

6.4.4 Comparison between 27 foci and 9 foci irradiation on samples

Table 6.18 summarizes the results for samples irradiated with the 27 foci MF lens and a focusing lens of 7.5 mm EFL. Table 6.19 summarizes the results for samples irradiated with the 9 foci MF lens and a 12 mm EFL focusing lens. There were differences in the results obtained by the 27 foci and the 9 foci setups and will be discussed.

Table 6.18 Summary for 27 foci irradiation of Sample C with focusing lens of 7.5 mm EFL

		Scanning speed (m/s)		
		0.1	1	10
Pulse repetition rate (kHz)	50	T: △◇ B: ■△ C: ●	T: △◇ B: ■ C: ●	T: △ B: ■ C: ○
	500	T: × B: ■ C: ○	T: × B: ■ C: ○	T: × B: ■ C: ○
	5120	T: × B: × C: ○	T: × B: × C: ○	T: × B: × C: ○

Legend: T *Top surface,* B *Bottom surface,* C *Mechanical cleavage*
■ *Ablation dominated scribe,* □ *Crack dominated scribe,* △ *Cracks,* ◇ *Subsurface damage,* × *No modification*
● *Sample cleaved,* ○ *Sample not cleaved*

Table 6.19 Summary for 9 foci irradiation of Sample C with focusing lens of 12 mm EFL

		Scanning speed (m/s)		
		0.1	1	10
Pulse repetition rate (kHz)	50	T: □△ B: ■ C: ●	T: □ B: ■ C: ○	T: ■ B: ■ C: ○
	500	T: × B: ■ C: ○	T: × B: ■ C: ○	T: × B: × C: ○
	5120	T: × B: × C: ○	T: × B: × C: ○	T: × B: × C: ○

Legend: T *Top surface,* B *Bottom surface,* C *Mechanical cleavage*
■ *Ablation dominated scribe,* □ *Crack dominated scribe,* △ *Cracks,* ◇ *Subsurface damage,* × *No modification*
● *Sample cleaved,* ○ *Sample not cleaved*

When a 50 kHz pulse repetition rate was employed, scribes were observed at all scanning speeds on the top polished surface of the samples irradiated with the 9 foci setup, whereas scribes were absent in the experiments with the 27 foci setup. The total foci separation was shorter for the 9 foci setup than the 27 foci set up, i.e. 348.9 μm and 399.5 μm respectively. As such, the distance between the foci nearest to the laser source and the top surface of the sample would be larger for the 9 foci setup and visible scribes should not be expected intuitively on the top surface. An explanation for the presence of these scribes could be attributed to the higher energy deposited for the 9 foci setup compared to the 27 foci setup, i.e. 39.9 mJ and 24.9 mJ respectively, see Table 6.11. The higher energy deposition of the 9 foci setup was more effective in inducing nonlinear absorption over a larger volume in the sample, thereby forming visible scribes on the top surface of the sample.

The widths of the ablation dominated scribes formed on the bottom rough surface differed between the 27 foci and the 9 foci setup when a 50 kHz pulse repetition rate was utilized, see Row 2 of Table 6.12 and Table 6.15 respectively. The former formed scribes with similar widths regardless of the scanning speed, while the latter formed scribes with decreasing widths as the scanning speed was increased. This illustrated that the widths of the ablation scribes formed on the bottom surface depended more on the proximity of the last diffractive order to the surface than the amount of energy deposition in the sample. The focus furthest from the laser source of the 9 foci setup was further away from the bottom surface compared to that of the 27 foci setup. The greater the distance the light had to travel to the bottom surface meant that more energy would be lost through linear absorption by the sample. The extent of energy loss through linear absorption by the sample was even greater than the loss in energy deposition by increasing the scanning speed. For the 9 foci setup, the accumulation of energy from internal reflection at the bottom surface was insufficient to compensate for the energy loss due to linear absorption by the bulk thickness. Therefore, the width of the scribes decreased with increasing scanning speed for the 9 foci setup.

A peculiar observation was that for samples scanned by a 1 mm/s scanning speed and a 50 kHz pulse repetition rate, the 9 foci setup had a larger energy deposition to the samples compared to that of the 27 foci setup. Yet, mechanical cleavage was possible for the latter but not for the former, see Row 3 Column B of Table 6.15 and Table 6.12 respectively. This could mean that the role of energy distribution and foci separation are important factors to consider. It was more important to split the laser energy over more foci, as with the 27 foci setup, such that each focus had less energy allocation and the foci were spaced closer to each other. In this case, the sample was more effectively weakened by laser irradiation for subsequent mechanical cleavage. This conclusion was made under the assumption that each focus had a sufficiently high intensity for nonlinear absorption to occur. In contrast, splitting the laser energy over fewer foci, each with more energy but spaced further apart, was less effective in weakening the sample for cleavage.

When the pulse repetition rate was increased to 500 kHz, no cracks, scribes or subsurface damage were observed on the top surface of the samples irradiated by either the 27 foci setup or the 9 foci setup for all scanning speeds, see Row 1 of Table 6.13 and Table 6.16 respectively. The higher pulse repetition rate of 500 kHz was unable to produce a sufficiently high pulse energy to induce large scale nonlinear absorption such that no modifications could be observed on the top surface of the samples.

For samples irradiated with a 500 kHz pulse repetition rate, the scribes observed on the bottom surface of the samples were thinner for the 9 foci setup than that of the 27 foci setup regardless of the scanning speed employed, see Row 2 of Table 6.16 and Table 6.13 respectively. This could be attributed to the large distance between the last diffractive order of the 9 foci setup and the bottom surface of the sample that caused a significant loss in energy through linear absorption by the bulk thickness. The effect of energy loss through linear absorption outweighed the effect of the increased energy deposition of a slow scanning speed. Even with internal reflection at the bottom surface for the accumulation of energy, there was still insufficient energy to form a continuous ablation scribe. It should be noted that the effect of energy loss through linear absorption was substantial in the 9 foci setup, such that no scribes were observed on the bottom surface of the sample irradiated with a 10 mm/s scanning speed and a 500 kHz pulse repetition rate, see Row 2 Column C of Table 6.16.

Regardless of the number of foci employed for irradiation and the scanning speed of the laser, samples scanned with the highest pulse repetition rate of 5.12 MHz did not exhibit any form of modification on their surfaces, see Rows 1 and 2 of Table 6.14 and Table 6.17. The low pulse energy generated by the highest pulse repetition rate could not induce nonlinear absorption in the samples and thus no modifications were observed on the surfaces of the samples.

Samples irradiated with the higher pulse repetition rates of 500 kHz and 5.12 MHz could not be mechanically cleaved for all scanning speeds, see Row 3 of Tables 6.13, 6.14, 6.16 and 6.17. The pulse energy of the laser was simply insufficient for inducing nonlinear absorption within the samples. Therefore, the samples could not be weakened for mechanical cleavage.

6.5 Conclusion

This study highlights the importance of having an appropriate focusing optic and EFL combination. The laser power was more effective when all the foci could be focused within the sample’s thickness. The close proximity of the foci maintained a region of high intensity over the length occupied by the multiple foci. As such, the high intensity of each focus could induce nonlinear absorption within the sample that was essential for machining sapphire.

An investigation was conducted to scan a section of the sample to understand the effects of having a short foci separation. The foci were spread over one-third of the sample's thickness which concentrated the laser power within the section. Section 5.4 concluded that a lack of energy for ablation resulted in crack formation. However, with this setup, by concentrating the laser power over a small section, an excess of energy could result in cracks and crack deviation from the scanning direction. It should also be highlighted that the further a focus or section was from the laser source, the harder it was to induce nonlinear absorption within the sample due to a loss in energy by linear absorption in the bulk thickness.

The effects of pulse repetition rate and scanning speed on the irradiation of samples were examined. High pulse energy and high peak power were required for nonlinear absorption. A low pulse repetition rate was employed to achieve such conditions. A reduction in scanning speed resulted in a greater accumulation of energy within the samples thereby increasing the energy deposited to form internal modifications. To have nonlinear absorption to produce a cleavable sample, a high pulse energy was more critical than depositing a large amount of energy.

7 Multizone scanning of sapphire with multiple foci technology

In Section 6.3, only a single section of the sample’s thickness was scanned. Even though mechanical cleavage was achieved for some samples, the sidewall profile was not ideal. Only a small section of the thickness produced a roughened sidewall desirable for LED application. The immediate surrounding areas contained large uncontrolled cracks that propagated away from the laser modified section. Multizone scanning of a few sections on the same scanning line could well minimize the formation of large cracks and encourage the formation of a roughened sidewall. Multizone scanning here refers to the multiple foci laser irradiation of the samples for more than one scan, with each consecutive scan in a different section of the sample’s thickness along the same scanning line.

Multizone scanning was examined here to gain an understanding if the laser power could be better utilized when certain targeted sections of the sample were scanned as opposed to scanning the entire sample’s thickness. For mechanical cleavage of the samples when an external pressure was applied, by weakening targeted sections of the sample via nonlinear modification, these sections would well promote the propagation of an initial separation crack throughout the sample’s thickness and along the scanned line. Indeed, it may be expected that this proposal might not be able to produce a fully roughened sidewall due to the lack of modifications in sections that were not scanned by the laser. However, it could provide a better understanding of which sections of the sample’s thickness was critical and should be scanned such that mechanical cleavage could be achieved successfully.

Another benefit of multizone scanning was that it enabled heat dissipation within the samples between each successive scan. Without heat dissipation, subsequent scans at other sections on the same scanning line might cause asymmetrical thermal and mechanical stresses to form within the sample. As a result, it could cause internal cracks to deviate away from the intended scanning direction. Subsequent attempts for mechanical cleavage could lead to sample separation deviated from the intended location of the laser scanned line. As such, the benefits of heat dissipation between consecutive multizone scans on the same scanning line were investigated.

7.1 Laser power adjustment for multizone scanning

The laser power had to be adjusted for multizone scanning for a fair comparison to the single zone scanning experiments. While experiments conducted with just two scanning zones, one-half of the maximum power was employed for each scan on the same scanning line, i.e. laser power was set at 0.57 W, see Figure 7.1. A 9 foci MF lens was paired with a focusing lens with a 7.5 EFL for the multizone experiments, while the single zone scanning experiments employed a 27 foci MF lens paired with the same focusing lens with a 7.5 mm EFL. The focused spot diameter at the focal length for both setups was 2.20 μm as the same EFL was employed. Since the same focusing lens was employed and the attenuation of the MF lenses were similar, the power transmission graphs for both setups overlapped each other.

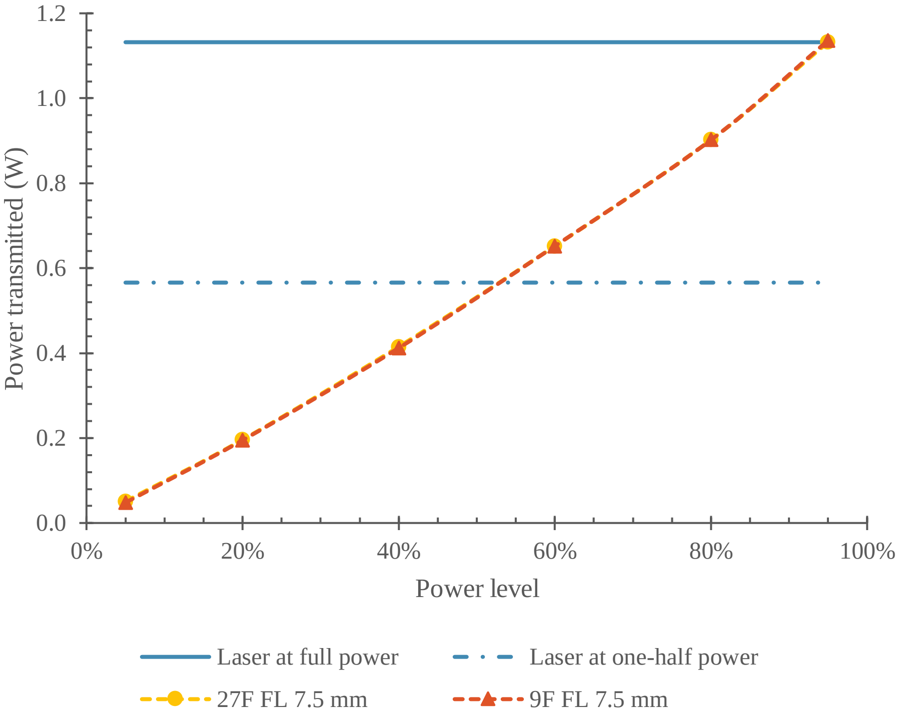

Figure 7.1 Power transmitted for combination of MF and FL optics and laser power settings for multizone scanning without any samples
The standard deviation ranges from 0.000 W to 0.004 W

7.2 Effect of scanning order for multizone scanning

Since multizone scanning required two scans to be conducted consecutively on the same scanning line, it was necessary to determine the order of scans to be made. Sample *C*, with a top polished surface and a bottom rough surface, was used in the experiments. A 9 foci MF lens and a focusing lens with a 7.5 mm EFL were employed for the experiments. The focused spot diameter at the focal length was 2.20 μm. This optic combination provided a total foci separation of 136.3 µm that was slightly smaller than one-third of the 430 µm thick sample. The experiments were conducted with Multizone *F*, with upper and lower scanning sections, such that the sections were sufficiently far apart, see Figure 4.11 of Section 4.2.3.6. Laser-material interaction in one section would not interact with another section to ensure that the results obtained would be clear and distinct. There should be no ambiguity regarding the results obtained due to interaction between sections with close proximity.

A 50 kHz pulse repetition rate was selected to provide high peak power and pulse energy to the samples, as the study in Section 6.4 has suggested. Samples were irradiated with the highest laser power possible of 1.14 W and at a 1 mm/s scanning speed to ensure that laser-material interaction was in the nonlinear regime and that there was sufficient energy deposited to encourage internal modification within the samples. A moderate scanning speed was chosen to minimize the possibility of internal crack formation and to reduce the chances of crack propagation and deviation. This allowed the sidewall profile of the samples after cleavage, if possible, to be studied without ambiguity between the laser modified areas and areas with internal cracks.

Two samples were irradiated at sections defined in Multizone *F*. One sample had its upper section irradiated first while the other sample had its lower section irradiated first. After multizone irradiation, mechanical cleavage of the samples was attempted.

Both samples had thicker scribes observed on their surfaces as a result of the higher laser power employed for irradiation. This meant that more of the laser power delivered was above the threshold for nonlinear absorption and more of the energy could be utilized for the formation of ablation dominated scribes. Hence, thicker scribes were observed.

7.2.1 Scanning of the upper section first

The sample with its upper section scanned first was observed to have a thick ablation scribe on the top polished surface and had a width of 14.6 μm, with a standard deviation of 0.2 μm. The ablation scribe was surrounded by cracks of different lengths. The larger cracks were observed to have deviated from the scanning direction and away from the ablation scribe, see Row 1 Column A of Table 7.1. Excess energy of the first scan on the upper section led to the formation of internal cracks which were propagated to form the small cracks observed on the top surface of the sample. The growth and propagation of the small cracks into longer deviated cracks could have been the result of the second scan. The second scan was meant to be focused at the lower section of the sample's thickness. However, internal modification at the upper section by the first scan hindered the propagation of light and some of the light could well be reflected off the laser modified areas and cracks. Consequently, some of the laser energy was trapped within this region which allowed the accumulation of energy. The energy accumulated was then channeled to further propagate and extend the small cracks into longer ones that deviated from the scanning direction.

The bottom rough surface of the sample was observed to have a discontinuous ablation scribe. In fact, upon closer inspection, there appeared to be three separate scribes adjacent to one another, see Row 2 Column A of Table 7.1. The average width of the scribes was 2.9 μm, with a standard deviation of 0.3 μm. As aforementioned, the modifications in the upper section by the first scan hindered the direct propagation of light from the second scan to the lower section. Light from the second scan was refracted by the laser modified areas and cracks before arrival at the lower section. This might have caused the laser beam to be focused away from their intended focal positions along the optical axis. Light that could be eventually focused might not even have the sufficient high intensity required for nonlinear interaction with the sample. However, with the phenomenon of internal reflection at the bottom surface to accumulate energy within the rough surface, some scribes were formed. Since the light incident on the bottom surface was not a single beam but a few non-concentric beams, separated ablation scribes were formed when sufficient energy was accumulated. This further supports the hypothesis that the beam could not be focused along the optical axis.

Even with the thick ablation scribes observed on both surfaces and the presence of cracks on the top surface, the sample could not be mechanically cleaved, see Row 3 Column A of Table 7.1. The high laser power employed for irradiation was not completely channeled to solely induce internal modification for the purpose of weakening the sample for subsequent mechanical cleavage. Hence, the sample was insufficiently weakened and cleavage could not be conducted.

7.2.2 Scanning of the lower section first

The second sample had its lower section scanned first and its upper section scanned next. The top polished surface was observed to have a thick ablation scribe that was surrounded by small cracks, while longer deviated cracks were not observed, see Row 1 Column B of Table 7.1. The ablation scribe had a width of about 15.3 μm, with a standard deviation of 0.5 μm. Since the first scan was at the lower section, the second scan at the upper section could be conducted without any obstructions. The excess energy of the second scan formed internal cracks which were then propagated to the top surface of the sample to form the small cracks observed. The longer deviated cracks could not be formed as there was insufficient energy to further propagate the cracks.

A thick continuous ablation scribe was observed on the bottom rough surface of the sample with a width of 16.0 μm and a standard deviation of 1.4 μm, see Row 2 Column B of Table 7.1. Without any interference, light from the first pass could be focused at the intended focal positions along the optical axis at the lower section. As the light interacted with the bottom surface, internal reflection could occur and the energy accumulated formed the single thick ablation scribe observed.

By scanning the lower section first, mechanical cleavage of the sample was successful. The sidewall profile was observed to have two distinctly separate laser modified areas, see Row 3 Column B of Table 7.1. However, the length of the lower zone was much shorter than the length of the upper zone, with lengths of approximately 18 μm and 132 μm respectively. The standard deviations were 1 μm and 3 μm for the respective regions. The modification of the lower zone, by the first scan, appeared to be formed by foci closer to the laser source. Judging by the length of the lower zone modification, it appeared that only diffractive orders +4 and +3 were responsible for the modification. This gave an indication that the majority of light had lost most of its energy due to linear absorption by the bulk thickness before the various multiple foci could be focused at the intended focal positions. Since the diffractive orders +4 and +3 were closer to the laser source, light would have travelled a shorter distance before being focused. This meant that less energy was lost through linear absorption within the sample and the energy at focus was high enough for nonlinear absorption to take place and internal modifications ensued. The converse was true, whereby diffractive orders further from the light source had to travel a longer distance before reaching their focus position. More energy would have been lost to the bulk thickness through linear absorption. As such, only linear absorption was possible at the focal positions of diffractive orders –4 to +2 and no laser modification areas were observed.

The results from this experiment could further substantiate the results obtained in Section 6.3. Previously, when a 27 foci MF lens was paired with an OB40× lens with the light focused at the lower section, there was no visible scribe formed on the bottom rough surface. The laser beam had to travel a long distance before focusing at the lower section, and thus a large portion of the energy would have been linearly absorbed by the sample. Further compounding the problem, a lower overall power was employed which meant that the energy allocated to each focus was even lower.

Even with internal reflection at the bottom surface, there was still not enough energy accumulation. It was unsurprising that no visible scribe could be observed on the bottom surface and the sample could not be cleaved.

Table 7.1 Optical images of samples' surfaces and sidewall profiles after multizone scanning to determine scanning order

Scanning order	*Column A*	*Column B*
First scan	Upper section	Lower section
Second scan	Lower section	Upper section
Top surface *Row 1*	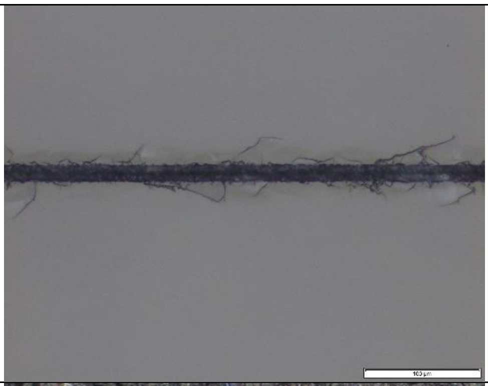	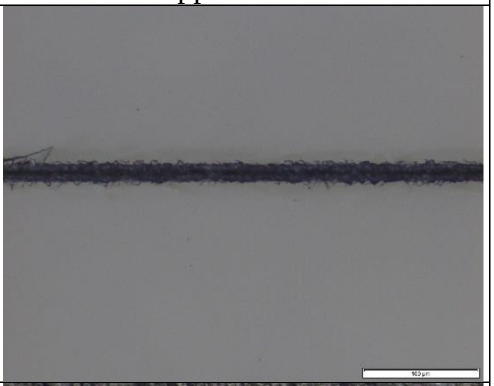
Bottom surface *Row 2*	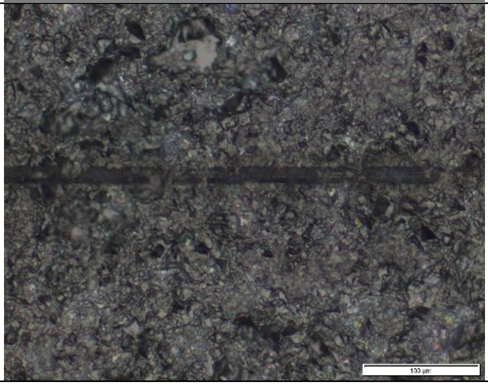	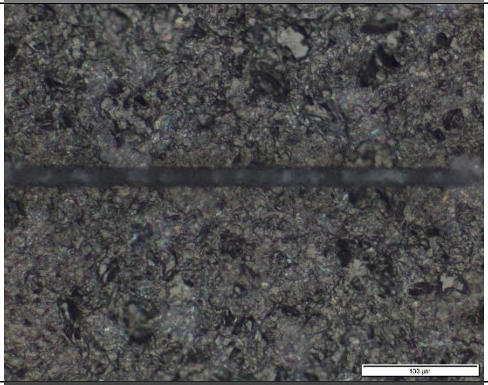
Sidewall *Row 3*	No cleavage	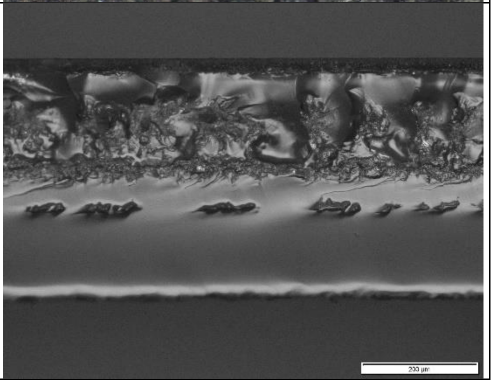

7.3 Effect of two-zone laser scanning

The aim of this study was to investigate if it was necessary to deploy all 27 foci for multiple foci laser irradiation or if it was better to employ fewer foci for irradiation by reallocating and concentrating the laser energy at certain sections within the sample's thickness. In particular, this study would explore two-zone scanning to determine if scanning a portion of the sample, with the same amount of energy, would be sufficient to weaken the sample for mechanical cleavage.

A 9 foci MF lens was paired with a focusing lens with a 7.5 EFL for the two-zone scanning experiments. The focused spot diameter at the focal length was 2.20 μm. The optic combination provided a total foci separation of 136.3 μm that was slightly smaller than one-third of the 430 μm thick sample. A 50 kHz repetition rate was selected as it provided the highest peak power; it thus had the highest probability of nonlinear absorption within the sample for internal modification and subsequent mechanical cleavage as stated in Section 6.4. The effects of energy deposition within the sample for two-zone scanning was studied by employing three scanning speeds of 0.1 mm/s, 1 mm/s and 10 mm/s. Each scan was conducted with a laser power of 0.57 W. The energy deposited for each scan at the various scanning speeds is tabulated in Table 7.2. Since two scans were conducted on the same scanning line, the total energy deposited for each scanning line was double the amount presented in Table 7.2, or simply the energy deposited for the 27 foci setup in Table 6.11. Sample *C*, with a top polished surface and a bottom rough surface, was used in the experiments.

Table 7.2 Relationship between scanning speed and energy deposition for laser power of 0.57 W

Scanning speed (mm/s)		0.1	1	10
Energy deposition (mJ)	**9 foci (EFL = 7.5 mm)**	12.5	1.25	0.12

Three two-zone combinations were employed in the experiments as defined in Figure 4.11 of Section 4.2.3.6. Multizone *D* comprised of scans in the middle and upper sections of the sample; Multizone *E* comprised of scans in the lower and middle sections of the sample; and Multizone *F* comprised of scans in the lower and upper sections of the sample. As established in Section 7.2, it was concluded that the first scan should be completed for the section closer to the bottom surface. This was to allow the laser to be properly focused within the sample along the optical axis for each scan without interference from the previous scans.

7.3.1 Scanning with Multizone *D*

7.3.1.1 Observations of samples' surfaces scanned with Multizone *D*

For samples scanned with Multizone *D* configuration, i.e. scans were focused in the middle and upper sections of the sample, scribes were observed on both surfaces of the samples for all scanning speeds, see Rows 1 and 2 of Table 7.3. There was no surprise that scribes were observed on the top polished surface due to the proximity of the upper section scan to the top surface of the sample. Intuitively, no scribes should be observed on the bottom rough surface since the middle section of the sample was scanned. Yet, scribes were observed on the bottom surface for all scanning speeds. A plausible explanation would be presented later in this section.

Samples scanned with the slower scanning speeds of 0.1 mm/s and 1 mm/s formed crack dominated scribes on the top surface of the sample that had an average width of 10.2 μm, with the standard deviation ranging from 0.9 μm to 2.0 μm; the sample scanned with the fastest scanning speed of 10 mm/s formed ablation dominated scribe on the top surface with a width of 3.2 μm, with a standard deviation of 0.9 μm. The width of the ablation dominated scribes on the bottom surfaces decreased from 7.2 μm to 5.0 μm with increasing scanning speed, with the standard deviation ranging from 0.4 μm to 1.7 μm.

When a sample was scanned by Multizone *D* at the slowest scanning speed of 0.1 mm/s, a crack dominated scribe was observed on the top polished surface of the sample that was surrounded by long deviated cracks, see Row 1 Column A of Table 7.3. This observation was caused by the second scan at the upper section since it had the closest proximity to the top surface. The large energy deposition from the second scan to the sample resulted in the formation of internal modifications and cracks. The excess energy was utilized to propagate the internal cracks to the top surface of the sample, and further propagation led to the additional lengthening of the surface cracks.

The ablation dominated scribe on the bottom rough surface was formed as a result of the first scan at the middle section when a scanning speed of 0.1 mm/s was employed, see Row 2 Column A of Table 7.3. As the scanning speed was the slowest, there was a large amount of energy deposited into the sample. Even though the middle section was far from the bottom surface, internal reflection of light managed to accumulate sufficient energy within this region such that an ablation scribe could be formed. Additionally, an offset crack was observed adjacent to the scribe. This was an indication that the amount of energy deposited in the sample was indeed in excess, such that the internal cracks formed could be propagated to the bottom surface, thus forming the offset crack observed.

At a moderate scanning speed of 1 mm/s, a crack dominated scribe surrounded by small cracks was observed on the top polished surface of the sample, see Row 1 Column B of Table 7.3. With the faster scanning speed, less energy was deposited into the sample. As such, the extent of interaction between the laser beam of the second scan and the internal modification made by the first scan was greatly reduced. Even with less energy accumulation within the section, there was still sufficient amount of energy for internal modifications and crack formation. The remaining energy was channeled to form and propagate internal cracks to the top surface of the sample. Since the amount of energy accumulated was not as large as that of the slower scanning speed, the cracks on the top surface were much shorter and had less deviation from the scanning direction.

Similar to the slower scanning speed, a scanning speed of 1 mm/s formed an ablation scribe on the bottom rough surface of the sample, see Row 2 Column B of Table 7.3. Internal reflection at the bottom surface enabled sufficient accumulation of energy within the region such that the ablation scribe could be formed.

At the fastest scanning speed of 10 mm/s, the top polished surface of the sample was observed to have an ablation dominated scribe surrounded by a HAZ, see Row 1 Column C of Table 7.3. The energy deposited in the sample had been reduced as a result of the faster scanning speed. With less energy deposited, most of the energy was channeled to internal modifications in the sample. The minimal excess of energy was insufficient to form cracks, but the energy was still high enough to form a visible HAZ around the ablation scribe.

Since the energy deposited was low, the sample irradiated with a scanning speed of 10 mm/s formed a thinner ablation scribe on the bottom rough surface of the sample, see Row 2 Column C of Table 7.3. The ablation scribe was formed in a similar method to those of the slower scanning speeds.

7.3.1.2 Mechanical cleavage of samples scanned with Multizone *D*

Generally, the samples scanned with Multizone *D* appeared to have resulted in the formation of a periodic roughened sidewall, see Row 3 of Table 7.3. As the scanning speed increased, it appeared that the uniformity of the structures on the sidewall was increased.

There were two main laser modified areas, one area located at the upper section and the other modified area included the middle and lower sections (despite that the lower section was not scanned). The top laser modified area in the upper section was dwarfed in comparison to the middle-bottom laser modified area in the middle and lower sections, with lengths averaging of about 77 μm and 213 μm respectively. The standard deviation ranges from 3 μm to 6 μm for the top modified area and 2 μm to 6 μm for the middle-bottom modified area.

There were three main gaps without visible laser modification observed on the sidewall. The first gap was between the top surface of the sample and the top laser modified area, the second gap was between the top and the middle-bottom laser modified areas and the third gap was between the middle-bottom laser modified area and the bottom surface of the sample. These gaps consisted of either wave-like cracks, due to an excess of energy deposition, or were smooth, as a result of mechanical cleavage. There appeared to be smaller laser modified areas at both surfaces of the samples for all scanning speeds. This verified the formation of the scribes observed on the surfaces of the samples.

As a first approximation, the length of laser modified area is assumed to be the length of total foci separation between the first and the last foci in the multiple foci setup, i.e. the focus closest to the laser source and the focus furthest from the laser source respectively. This was under the assumption that the intensity of each focus was high enough for nonlinear absorption and all foci were responsible for the formation of the modified area. Hence, the total foci separation was an estimation of the length of the laser modified area.

The observed length of the top laser modified area was approximately 77 μm for all scanning speeds. This is shorter than the 136.3 μm from the first approximation. The laser modified areas were dominantly formed by nonlinear absorption in the sample due to the high intensity laser beam. The nonlinear absorption within the sample caused the alteration of the internal structure; this eventually led to the formation of a roughened sidewall. When an excess of energy was deposited in the sample, internal cracks were formed within the section. The remaining energy would then be channeled to propagating the cracks away from the section. Although the top modified zone's main characteristic feature of a roughened sidewall was directly formed through nonlinear absorption, it could have contained some small internal cracks. The measurement for the length of the top modified zone did not include areas that were dominantly comprised of the larger wave-like internal cracks, and this could have underestimated the true length of the top modified zone.

A more perplexing observation was that the length of the middle-bottom modified zone for all scanning speeds was consistently and greatly exceeded the expected length of modification by first approximation, which were approximately 213 μm and 136.3 μm respectively. The middle-bottom modified zone seemed to have included both the middle and lower scanning sections, when only the middle section was scanned by the laser.

Internal reflection at the bottom rough surface of the sample could have been a possible explanation that the modification area was larger than expected. The majority of the energy from the laser was channeled to the formation of the modification areas; a portion of the energy was channeled to the formation and propagation of internal cracks. As the laser beam propagated downwards along the optical axis, it still contained a small amount of energy. When the incident angle of light on the bottom rough surface of the sample exceeded the critical angle, internal reflection of light would occur. The interaction between the incoming laser beam and the internally reflected laser beam could have refocused the light forming secondary multiple foci at the lower section of the sample, as seen in [11], where concave mirrors were employed instead. This allowed for the accumulation of energy for nonlinear absorption to occur within the sample. As a result, internal modification in the lower section was possible, and hence the length of the middle-bottom laser modified area appeared to be longer than expected.

Taking a closer look at the individual sidewall profiles of the samples scanned with Multizone *D* when different scanning speeds were employed, it appears that the scanning speed had an impact on the uniformity and the periodicity of the roughened modified areas.

At the slowest scanning speed of 0.1 mm/s, the laser interacted with the sample over a longer period of time and thus a large amount of energy was deposited to the sample. Nonlinear absorption within the sample led to the formation of larger distortions in the modification areas, see Row 3 Column A of Table 7.3. Additionally, the gaps were observed to contain larger and more wave-like patterns. These wave-like patterns were internal cracks formed by the excess energy. The amount of excess energy dictated the size and quantity of the internal cracks formed. The cracks appeared to have extended to both the top and bottom surfaces of the sample. This further verified the presence of the larger cracks and an offset crack observed on the respective surfaces of the sample.

At the moderate scanning speed of 1 mm/s, less energy was deposited in the sample and there was less time for the laser beam to interact with the sample. As a result, less distortions were observed in the laser modified areas with an increase in the uniformity and periodicity of these distortions, see Row 3 Column B of Table 7.3. This could mean that there was less formation of cracks in the laser modified areas. With a reduction in energy deposition, smaller wave-like patterns were observed in the gaps near the top surface of the samples thus verifying the presence of small cracks observed on the top surface.

At the fastest scanning speed of 10 mm/s, the least amount of energy was deposited in the sample as there was an even shorter period for light to interact with the sample. The laser beam had a sufficiently high intensity for nonlinear absorption within the sample and the majority of the energy deposited would be channeled to internal modification of the sample. As a result, a laser modified area with the least amount of distortion was observed, see Row 3 Column C of Table 7.3. These distortions were smaller and a more uniform sidewall profile was produced. There were virtually no wave-like patterns in the gaps; this meant that there was probably little or no visible internal crack formation in the sample to propagate to the sample's surfaces. As such, there was no cracks observed on either surface of the sample.

Table 7.3 Optical images of samples after irradiation with Multizone D at various scanning speeds

	Scanning speed		
	0.1 mm/s *Column A*	**1 mm/s** *Column B*	**10 mm/s** *Column C*
	Multizone D Middle and upper sections		
Top *Row 1*	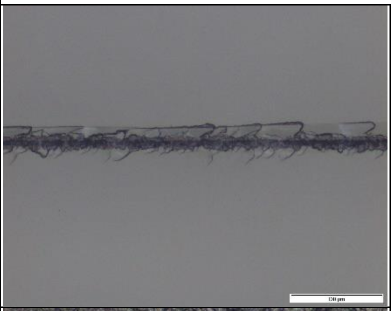	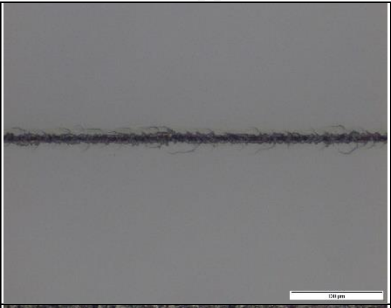	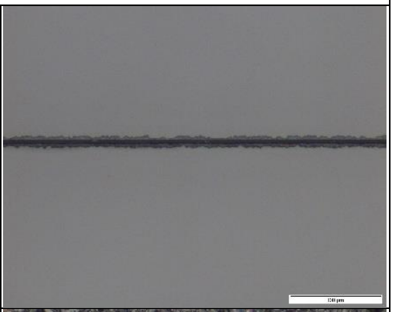
Bottom *Row 2*	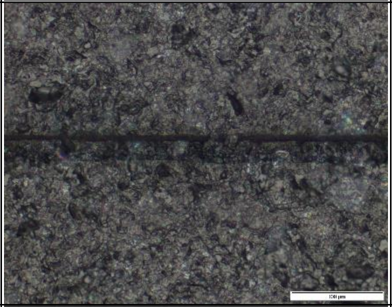	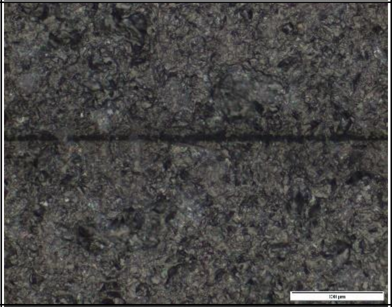	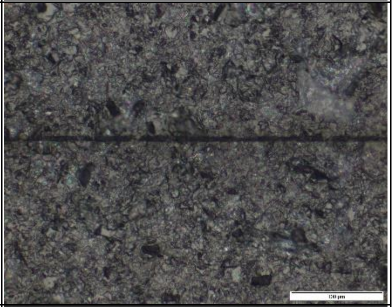
Sidewall *Row 3*	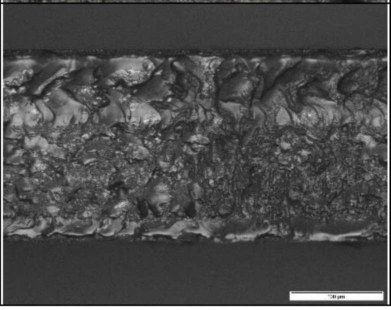	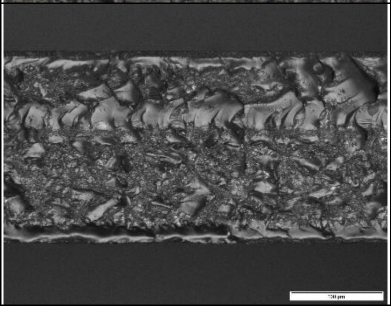	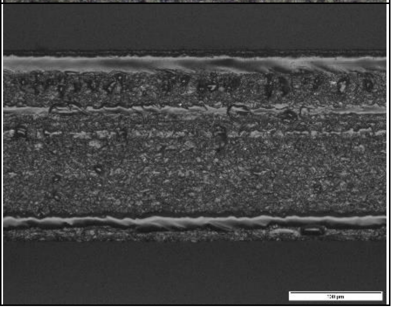

7.3.2 Scanning with Multizone *E*

For samples scanned with Multizone *E* configuration, i.e. scans were focused in the lower and middle sections of the sample, subsurface damage only was observed on the top polished surface for all scanning speeds, see Row 1 of Table 7.4. This was attributed to the lack of proximity of the middle section to the top surface. Any internal modifications or cracks formed by the laser was mainly confined within the lower and middle sections or the immediate surrounding areas. Even if there was an excess of energy deposited in the sample, the extent of crack propagation was small. There might have been some extension of cracks to the surrounding areas, but the energy deposited was insufficient to propagate the internal cracks to the top surface of the sample. Therefore, only subsurface damaged could be observed from the top surface of the samples for the scanning speeds employed.

As expected, since the lower section was scanned first, ablation dominated scribes were observed on the bottom rough surface of the samples for all scanning speeds, see Row 2 of Table 7.4. The close proximity between the lower section and the bottom surface reduced the laser beam energy loss through linear absorption by the bulk thickness between the focal position and the bottom surface. Consequently, it enhanced the amount of energy accumulated within this region as a result of internal reflection at the bottom surface. When the accumulated energy exceeded the threshold for ablation, an ablation scribe was formed. As the scanning speed was increased, the width of the ablation scribes decreased from 10.8 μm to 5.5 μm. The standard deviation ranges from 0.4 μm to 1.6 μm.

At the slowest scanning speed of 0.1 mm/s, an ablation dominated scribe with an offset crack was observed on the bottom rough surface of the sample, see Row 2 Column A of Table 7.4. The ablation scribe was routinely formed due to the accumulation of energy by internal reflection at the bottom surface as a result of the first scan at the lower section. The formation of the offset crack will be explained in Section 7.3.4.

When the samples were scanned at the faster scanning speeds of 1 mm/s and 10 mm/s, an ablation scribe was only observed on the bottom rough surface of the samples without any presence of cracks, see Row 2 Columns B and C of Table 7.4 respectively. Increasing the scanning speed reduced the amount of energy deposited into the samples. Even with a reduction in energy deposition, internal reflection at the bottom surface of the sample encouraged energy to accumulate within this region. An ablation scribe was formed on the bottom surface when there was sufficient energy accumulated. When the scanning speed was increased, the decrease in energy deposition resulted in the formation of thinner ablation scribes. As such, there was little excess energy to form and to propagate internal cracks to the bottom surface of the sample. Hence, no cracks were observed on the bottom surface.

Mechanical cleavage could not be conducted on the samples scanned with Multizone *E* for all scanning speeds, see Row 3 of Table 7.4. This was due to the ineffective modifications of the samples through nonlinear absorption. Hence, the samples were insufficiently weakened and could not undergo mechanical cleavage.

Table 7.4 Optical images of samples after irradiation with Multizone E at various scanning speeds

	Scanning speed		
	0.1 mm/s *Column A*	**1 mm/s** *Column B*	**10 mm/s** *Column C*
	Multizone E Lower and middle sections		
Top *Row 1*			
Bottom *Row 2*	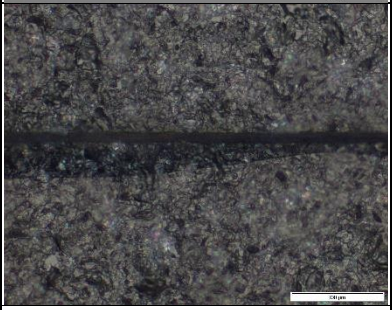	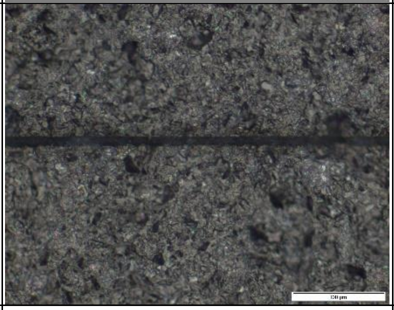	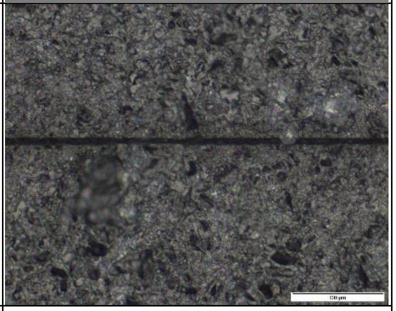
Sidewall *Row 3*	No cleavage	No cleavage	No cleavage

7.3.3 Scanning with Multizone *F*

Scans were focused in the lower and upper sections of the sample for samples scanned with Multizone *F* configuration. Owing to the close proximity of the scanning sections to a sample's surfaces, it was no surprise that scribes were observed on both the top polished surface and the bottom rough surface of a sample for all scanning speeds, see Rows 1 and 2 of Table 7.5. As the scanning speed was increased, the width of the scribes found on both surfaces decreased. For the top surface, the scribe width decreased from 10.4 μm to 3.3 μm, with standard deviation ranging from 0.4 μm to 1.0 μm; for the bottom surface, the scribe width decreased from 11.9 μm to 2.4 μm, with standard deviation ranging from 0.6 μm to 2.3 μm.

The sample scanned at the slowest scanning speed of 0.1 mm/s formed a crack dominated scribe surrounded by small cracks on the top polished surface of the sample, see Row 1 Column A of Table 7.5. The formation of the crack dominated scribe was mainly due to the second scan at the upper section. The large laser energy deposition induced the formation of internal cracks and subsequently propagated these cracks to the top surface of the sample.

At a scanning speed of 0.1 mm/s, an ablation scribe was formed on the bottom rough surface due to the first scan at the lower section, see Row 2 Column A of Table 7.5. Internal reflection at the bottom surface allowed for the accumulation of energy within this region. When the energy accumulated was above the threshold for ablation, an ablation scribe was formed.

At the moderate scanning speed of 1 mm/s, a crack dominated scribe surrounded by small cracks was observed on the top polished surface of the sample, see Row 1 Column B of Table 7.5. Since a lower amount of energy was deposited in the sample, the cracks appeared to be more uniform and periodic compared to the non-uniform cracks observed when more energy was deposited at the slowest scanning speed. With internal reflection at the bottom rough surface of the sample, there was sufficient accumulation of energy to form an ablation scribe, see Row 2 Column B of Table 7.5.

At the fastest scanning speed of 10 mm/s, an ablation dominated scribe surrounded by a HAZ was observed on the top polished surface of the sample, see Row 1 Column C of Table 7.5. With a faster scanning speed, less energy from the second scan was deposited to the sample. The majority of the energy was utilized to form internal modifications in the upper section of the sample. Excess energy was minimal and was insufficient to form and propagate cracks. Instead, the excess energy resulted in the formation of a visible HAZ around the ablation scribe. Internal reflection at the bottom rough surface encouraged the accumulation of energy to form the thin ablation scribe observed, see Row 2 Column C of Table 7.5.

Mechanical cleavage could not be carried out on samples scanned with Multizone *F* at any scanning speed, see Row 3 of Table 7.5. This was due to the lack of internal modifications within the samples through nonlinear absorption. Hence, the samples were insufficiently weakened and mechanical cleavage could not be successfully performed.

Table 7.5 Optical images of samples after irradiation with Multizone F at various scanning speeds

	Scanning speed		
	0.1 mm/s *Column A*	**1 mm/s** *Column B*	**10 mm/s** *Column C*
	Multizone F Upper and lower sections		
Top *Row 1*	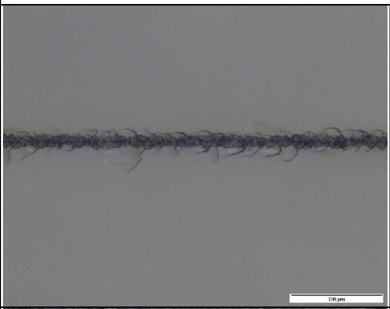	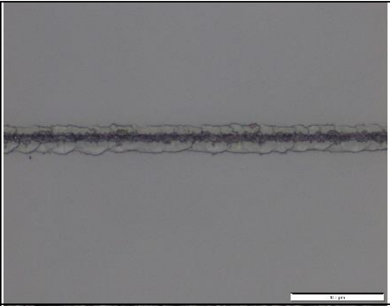	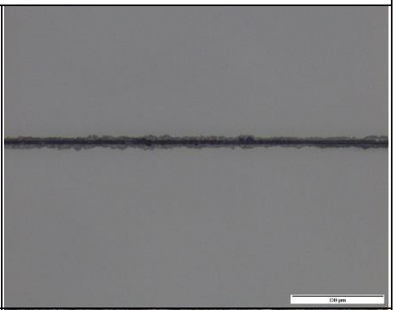
Bottom *Row 2*	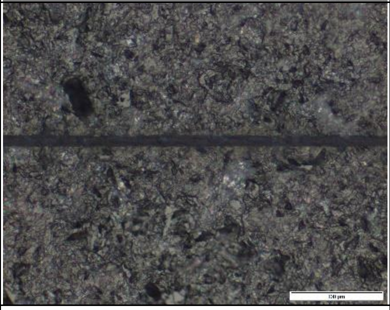	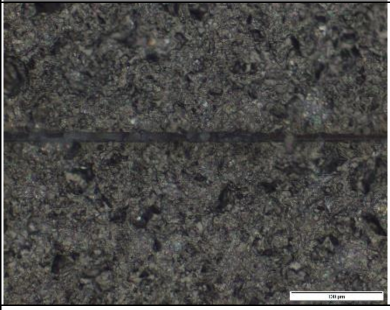	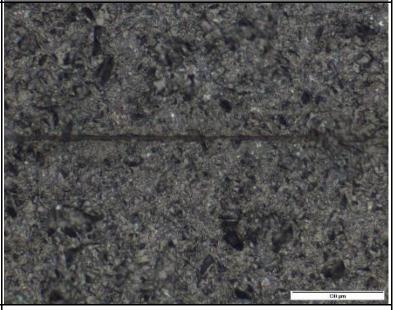
Sidewall *Row 3*	No cleavage	No cleavage	No cleavage

7.3.4 Comparison between different configurations in two-zone laser scanning

A summary of the results obtained from two-zone laser scanning is presented in Table 7.6. The difference between the results obtained from the various multizone scans are discussed. The scanning order of the sections were determined in Section 7.2, i.e. the section that was furthest from the laser source was scanned first and the section closer to the laser source was scanned last.

Table 7.6 Summary for two-zone laser scanning of Sample C

		Scanning speed (m/s)		
		0.1	1	10
Multizone (order of scanning sections)	*D* Middle & upper	T: □△ B: ■△ C: ●	T: □△ B: ■ C: ●	T: ■ B: ■ C: ●
	E Lower & middle	T: ◇ B: ■△ C: ○	T: ◇ B: ■ C: ○	T: ◇ B: ■ C: ○
	F Lower & upper	T: □△ B: ■ C: ○	T: □△ B: ■ C: ○	T: ■ B: ■ C: ○

Legend: T *Top surface,* B *Bottom surface,* C *Mechanical cleavage*
■ *Ablation dominated scribe,* □ *Crack dominated scribe,* △ *Cracks,* ◇ *Subsurface damage,* ✕ *No modification*
● *Sample cleaved,* ○ *Sample not cleaved*

Comparing the scribe observed on the top surface of the sample scanned with Multizone *D* to that of Multizone *F* at a 0.1 mm/s scanning speed, the cracks of the former appeared to be longer and had a larger deviation from the scanning direction, see Row 1 Column A of Table 7.3 and Table 7.5 respectively. Both samples had been scanned in the upper section, yet two different results were obtained. The difference lies in the proximity of the other scanning section.

The other scanning section for Multizone *D* was the middle section, while it was the lower section for Multizone *F*. Since the first scan conducted was for the section closer to the bottom surface, the middle section was scanned first for Multizone *D* and the lower section was scanned first for Multizone *F*. If the energy deposited at the section was sufficient, assuming that the laser beam was of sufficiently high intensity, nonlinear absorption would occur and internal modifications would be formed at the respective sections. Bearing in mind that the further the section was from the laser source, the greater the energy loss due to linear absorption by the bulk thickness. The second scan conducted would be at the upper section for both Multizone *D* and *F*.

The lower and upper scanning sections for Multizone *F* were far apart and thus there was minimal interaction of light between the sections. As the energy deposited for a single scan was large, a portion of the energy of the second scan in the upper section was channeled into forming internal modification in that section. The excess energy deposited caused cracks to form which were then propagated to the top surface of the sample. The cracks acted as micro-surfaces that allowed light to be reflected within this region. However, the energy accumulated was only sufficient to form a thicker crack dominated scribe but could not further propagate the top surface cracks. The absence of longer deviated cracks was attributed to the lack of proximity between the lower and upper scanning sections.

For Multizone *D*, both scanning sections were adjacent to one another, i.e. the middle and upper sections. Light from the second scan interacted with the internal modifications formed by the first scan. The modifications acted as micro-surfaces which allowed light from the second scan to be reflected back up towards the top surface, further intensifying the energy within the upper section. This allowed for an even larger amount of energy accumulation at the upper section. In addition to forming internal modification and cracks that propagated to the top surface, there was still energy in excess to form a thick crack dominated scribe and to further elongate the cracks with greater deviation away from the scanning direction. Therefore, the longer deviated cracks were observed on the top surface for the sample scanned with Multizone *D* but not for Multizone *F*.

Samples scanned by either Multizone *D* or Multizone *F* resulted in scribes forming on both surfaces, see Rows 1 and 2 of Table 7.3 and Table 7.5 respectively. Yet, only samples scanned by Multizone *D* could be cleaved for all scanning speeds tested, see Row 3 of Table 7.3 and Table 7.5 respectively.

Intuitively, one might expect that a sample scanned with Multizone *F* would have given the best probability of mechanical cleavage since the lower and upper sections were scanned. The weakened lower and upper sections should have been more susceptible to cleavage. Any initial crack separations formed within the lower and upper sections would extend through the sample’s thickness during attempted cleavage and facilitated the complete separation of the sample. However, Section 7.2 highlighted that scans at the lower section could not provide complete internal modification of the section due to energy loss through linear absorption by the bulk thickness of the sample.

In contrast, samples scanned with Multizone *D* could be cleaved. For Multizone *D*, the first scan had to be at the middle section of the sample. Intuitively, internal modifications would be formed at the middle section accordingly. In addition to light-material interaction in the middle section, the interaction between the incoming laser beam and the internally reflected light at the bottom rough surface of the sample accumulated sufficient energy such that nonlinear absorption at the lower section was possible. Consequently, internal modification across both the middle and lower sections was formed. When the upper section was scanned next, internal modification at the upper section occurred. As a result of the two scans, a plane of laser modification along the optical axis that spanned the majority of the sample's thickness was produced, thereby effectively weakening the sample for cleavage. Therefore, samples scanned with Multizone *D* could be successfully cleaved.

Comparing the optical images of the bottom surface of the samples scanned with either Multizone *E* or Multizone *F* at a 0.1 mm/s scanning speed, a peculiar observation was the formation of an offset crack next to the ablation scribe for the former but not the latter, see Row 2 Column A of Table 7.4 and Table 7.5. Both samples had been scanned in the lower section, yet different results were observed. Likewise, the difference lies in the proximity of the other scanning section. The other scanning section for Multizone *E* was the middle section, while it was the upper section for Multizone *F*. Even though the first scanning section was at the lower section for both samples, there could be interaction between the first and second scanning sections and thus different results were achieved.

For the sample scanned with Multizone *F*, the proximity between the first and second scans, i.e. the lower and upper sections respectively, were rather far apart. This reduced the extent of interaction between the two scans such that the scribe observed on the bottom surface was the result of scanning the lower section only.

In contrast, the first and second scans were in close proximity for the sample scanned with Multizone *E*, i.e. the lower and middle sections respectively. For the first scan at the lower section, internal modifications were formed if there was sufficient energy accumulated through direct energy deposited by incoming laser beam to the section and internal reflection at the bottom rough surface. These modifications acted as micro-surfaces that disrupt the propagation of light along the optical axis through reflection or refraction. Since the second scan at the middle section was just above the lower section, light from the second scan could interact with the modifications formed by the first scan. As a result of the interaction, a portion of the light was reflected back up towards the top surface and continued to interact with the incoming laser beam. This interaction between the reflected and the incoming laser beam further intensified the energy within the middle section, thereby increasing the energy accumulated. When sufficient energy was accumulated, internal modification within the middle section was formed. The excess energy resulted in the formation of internal cracks. As more energy was accumulated, the energy was channeled towards propagation of these internal cracks. Internal modifications formed in the lower section effectively weakened the material within this section. Since the propagation of cracks favored a path of lowest resistance, the cracks from the middle section extended into the modified areas in the lower section and eventually propagated to the bottom surface of the sample. The crack at the bottom surface was observed to be offset to the ablation scribe as the propagation of the cracks could not be controlled.

At a 10 mm/s scanning speed, the widths of the ablation scribes on the bottom surface of the samples were thicker for Multizone E than for Multizone F, i.e. 5.5 μm and 2.4 μm respectively, see Row 2 Column C of Table 7.4 and Table 7.5 respectively. A possible explanation could be due to the proximity of the scanning sections, as aforementioned. The close proximity of the lower and middle scanning sections of Multizone E encouraged interaction between scans. It was hypothesized that a portion of laser beam from the second scan would be reflected upwards as a result of interaction with the modified areas formed by the first scan. Since light could either be reflected or refracted by the micro-surfaces of the modified area, the remaining portion of laser beam would have been refracted into the modified area. Through the interaction with the modified area, light would be trapped and its energy was accumulated within this region. Internal reflection at the bottom surface further enhanced the amount of energy accumulated at the lower section.

There was more energy available in the region and as a result, a thicker ablation scribe was observed on the bottom rough surface of the sample scanned with Multizone *E*.

In contrast, the lower and upper scanning sections of Multizone *F* were far apart. There was a substantial energy loss after forming internal modifications in the upper section. The energy was further depleted through linear absorption by the bulk thickness as light propagated towards the lower section. When light arrived at the lower section, the energy would have been low to interact with the modified areas in a significant manner. Energy could have been accumulated in the lower section through the trapping of light within the modified areas in the lower section, if any, and through internal reflection at the bottom rough surface. However, the extent of energy accumulation in the lower section was insignificant and could not further thicken the ablation scribe. Therefore, a thin ablation scribe was observed on the bottom surface of the sample scanned with Multizone *F*. Furthermore, an offset crack from the scanning direction was not observed due to the lack of interaction between the lower and upper scanning sections.

7.4 Conclusion

In this chapter, an investigation was conducted on multizone scanning of sapphire samples on their cleavability and the sidewall profiles of cleaved samples. For scanning purpose, a sample's thickness was divided into three equal sections along the optical axis; mainly the upper, middle and lower sections.

Increasing the cleavability of a sample could be achieved by conducting the first scan for a section that was furthest from the laser source, with subsequent scans at sections closer to the laser source. This avoided interference by internal modifications formed by the previous scan with the transmission of light by the current scan. As a result, the laser energy delivered to the sample could be effectively utilized for nonlinear absorption and modifications.

As the name suggests, two-zone scanning of samples required two out of the three sections to be scanned successively. Scribes were observed on both sample's surfaces when the samples were scanned with Multizone *D* (scans in the middle and upper sections) and Multizone *F* (scans in the lower and upper sections). Samples scanned with Multizone *E* (scans in the lower and middle sections) had scribes only on the bottom surface. However, only Multizone *D* samples could be cleaved. The cleaved samples revealed that a uniformly roughened sidewall that spanned across the entire sample's thickness could be achieved with multiple foci irradiation even though only the top two sections were scanned. For effective nonlinear absorption and modification, these observations indicated that the appropriate redistribution of the laser power at targeted sections would be a more effective use of laser power than simply reducing the scanning speed to increase the energy deposition to the sample.

8 Conclusions and future work

8.1 Conclusions

The effects of surface morphology on the optical properties of sapphire have not been properly studied previously. Current studies on multiple foci laser cutting have been mostly focused on transparent glass cutting. The foci spots were spread over the glass thickness employing highly specialized focusing optics [11], [12].

This thesis examined the interaction between the laser beam and sapphire with different surface morphology, with emphasis on surface roughness of the samples. Multiple foci technology has been successfully adapted for singulation of 430 μm thick sapphire samples with a 1064 nm picosecond laser.

The following studies have been conducted to address the current research gaps:

1. The effect of surface roughness on the linear optical properties of sapphire – A rough surface will improve light extraction of light emitting diodes (LEDs), such as in patterned sapphire substrates [15], [16]. However, hitherto the interaction between light and surface roughness during laser scanning has not been investigated in depth. A hypothesis, with the associated computation, was formulated that a sample with a single rough surface would exhibit higher levels of absorbance compared to a sample with two polished surfaces. This is predominantly a result of internal reflection at the exit surface. As such, internal reflection can be enhanced by orientating the sample such that the rough surface was facing away from the laser. Optical spectrometry results verified the hypothesis. The sample with its rough surface facing away from the laser exhibited the highest absorbance, in particular at the operational wavelength of the laser (i.e. 1064 nm).

Understanding the effect of surface roughness on the linear optical properties of sapphire allows for better decision making to exploit or avoid the phenomena of internal reflection at the exit surface of the samples. For applications that require the nonlinear absorption of laser energy within a sample, internal reflection is to be encouraged and a roughened exit surface is recommended. For applications that require the transmission of laser energy through a transparent sample (e.g. in LIPAA applications [18]), with minimal absorption, internal reflection should be avoided and it is advised to employ a smooth polished exit surface.

2. The effects of surface roughness on the nonlinear absorptivity of sapphire – Machining sapphire samples requires nonlinear absorption to occur within the transparent material. Consistent with the linear optical properties study, the investigation of the nonlinear characteristics of sapphire also discovered that the sample with its rough surface facing away from the laser beam source displayed the highest nonlinear absorptivity as expected. The presence of the rough surface induced additional nonlinear absorption within the sample. Dominant nonlinear absorption was observed in the sample with its rough surface facing away from the laser. After picosecond laser irradiation on the top surface of the samples with a focused spot size of 27.1 μm at 1.7 W, ablation scribes were observed on both surfaces of a sample. This meant that nonlinear absorption was present over the sample's thickness. Therefore, not only can laser ablation be performed on sapphire with a rough surface, but the presence of the bottom rough surface improves the nonlinear interaction between the laser beam and the sample. The bottom rough surface enhances the nonlinear interaction between the laser beam and the sample and thus increases the effectiveness of machining sapphire samples.

3. Multiple foci laser technology for sapphire singulation – A roughened sidewall profile has been established to improve the light extraction of LEDs [13], [14]. Such a profile could be achieved with multiple foci laser irradiation of samples. This thesis successfully adapted the multiple foci laser technology from glass cutting to transparent sapphire singulation. Commercially available multifocal lenses and focusing optics were employed to scan the entire sample thickness in a single pass. This meant that highly specialized optics were unnecessary; this will improve the accessibility of the multiple foci technology. The effective focal length employed dictated the focused spot diameters. Diffractive order 0 (i.e. at the focal length of the focusing optic) was focused at the midplane of the sample's thickness. This study highlighted the importance of a low pulse repetition rate (i.e. high pulse energy and high peak power) over a low scanning speed (i.e. more energy deposition) in producing a cleavable sample. Increasing the energy deposition alone was ineffective if high laser intensity was absent to induce nonlinear absorption within the sample. When a 1.13 W laser power was utilized in the experiments, it was recommended to employ a pulse repetition rate of around 50 kHz and scanning speeds of 1 mm/s or below. Cleaved samples revealed a non-uniform roughened sidewall profile as a result of nonlinear modification at the various foci spots. This non-uniform roughened sidewall profile is desirable for LED light transmission.
4. Multizone scanning for multiple foci irradiation – With multiple foci technology successfully adapted for sapphire singulation, an innovative proposal for a more effective use of laser energy was explored with multizone scanning. The proposed method entails scanning selected sections of the sample's thickness successively, allowing for heat dissipation between scans. For two-zone scanning of samples, two out of three sections of

equal thickness were irradiated at 0.57 W for each scan. Each section was irradiated with 9 foci, each having a focused spot diameter of 2.20 μm. Diffractive order 0 (i.e. at the focal length of the focusing optic) was located at the midpoint of each section. With a 50 kHz pulse repetition rate and 10 mm/s scanning speed, a cleavable sample was achieved when the top two-thirds of the sample's thickness was scanned; with the middle section scanned first and the upper section scanned next. Although only a portion of the thickness was scanned, the cleaved sample revealed a uniformly roughened sidewall profile over the entire sample's thickness. Therefore, not only did two-zone scanning produced a cleavable sample with a roughened sidewall profile, this innovative method achieved more desirable results with less energy deposition.

In summary, the consequence of a sample's surface morphology on its interaction with a laser beam was first highlighted in this investigation. The sample with a single rough bottom surface orientated away from the laser beam resulted in the highest level of absorptivity in the sample due to internal reflection at the bottom surface. An adaptation of multiple foci laser technology for transparent sapphire singulation was first introduced in this study. Cleavable samples revealed a non-uniform roughened sidewall profile, as a result of nonlinear modification at the various foci spots. The two-zone scanning of sapphire samples, employing multiple foci technology, was proposed to improve the efficiency and effectiveness of the process. Cleavable samples with uniform roughened sidewall profile throughout the sample's thickness were produced through two-zone scanning of the top two-thirds of the sample only. This in an innovative technique for an effective and efficient cleavage of the sapphire samples.

8.2 Recommendations for future work

This investigation has examined the order of magnitude of the various laser parameters for facilitating a successful cleavage of multiple foci picosecond laser irradiated sapphire samples. A limited number of foci was explored (i.e. with either 9 foci or 27 foci multiple focal lens) for the singulation of a 430 μm thin sapphire sample. An innovative multizone scanning method was adopted to scan the top two-thirds of a sample's thickness that resulted in a cleavable sample. Further investigations are recommendations to include the following:

1. Precise optimization of laser parameters for multiple foci laser irradiation of sapphire samples – The current study only determined the order of magnitudes for the laser parameters for sample cleavage. Future investigations can focus on the optimization of laser parameters (e.g. pulse repetition rate and scanning speed) for better effectiveness and efficiency.
2. Adaptation of the multizone setup for the singulation of thicker sapphire samples – Substantial energy loss through linear absorption within the bulk thickness was observed in the current experiments even with 430 μm thin sapphire samples. However, two-zone scanning at targeted sections of the samples demonstrates that it was a viable method to overcome the energy loss while simultaneously improving the efficiency of the process. This method can be further explored and adapted to cleave thicker samples by scanning specific sections near the top sample surface.

   For example, two-zone scanning can be adapted to machine thicker sapphire samples, see Figure 8.1. A two-zone scanning of the top two-thirds of a thick sample (Future Investigation A in Figure 8.1), with the first scan in the middle one-third section and the next scan in the upper one-third section, can be conducted in a similar manner as discussed in this thesis.

To embrace the essence of multizone scanning for thicker samples, a thicker sample can be split into more scanning zones (Future Investigation B in Figure 8.1). As such, the minimum number of scanning zones required for sample separation can be determined by increasing the number of zones scanned from 1 till N until sample separation is achieved. Noting that zones further from the laser source are to be scanned first (i.e. in descending order from Zone N to Zone 1). Therefore, this investigation can better identify the minimum irradiation thickness of a sample required to separate the sample, and it may be less than two-thirds of the sample thickness. The efficiency of machining thicker sapphire samples can be improved. However, the uniformly roughened sidewall profile of cleaved samples may not be guaranteed for multizone scanning.

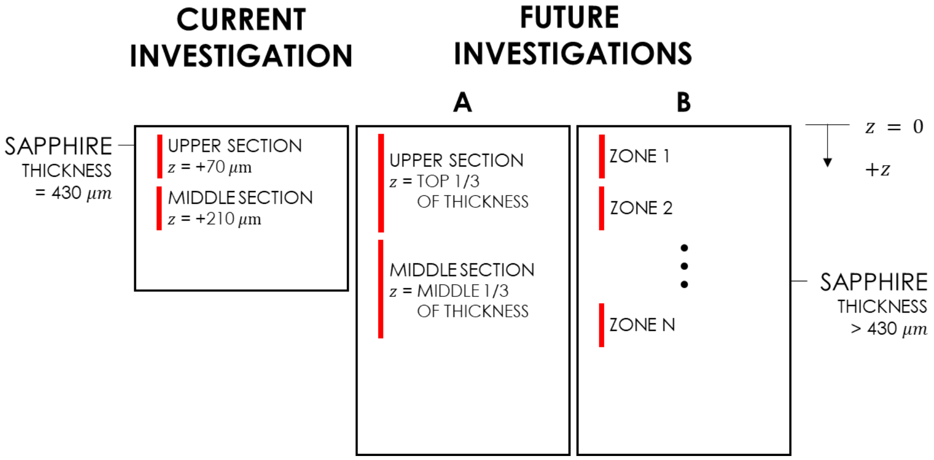

Figure 8.1 Schematic for multizone scanning of thicker sapphire samples

3. Investigation of three-zone multiple foci irradiation of sapphire samples – A better insight can be gained by investigating the effects of heat dissipation between successive scans,

especially its impact on cleavability and sidewall profiles of the samples. The effects of heat dissipation can be evaluated by a comparison between irradiation of the entire sample's thickness with a long effective focal length (EFL) in a single scan and irradiation of the sample with a shorter EFL in consecutive sections with several scans, see Figure 8.2. The time interval between consecutive scans will have significant heat dissipation as compared to a single scan.

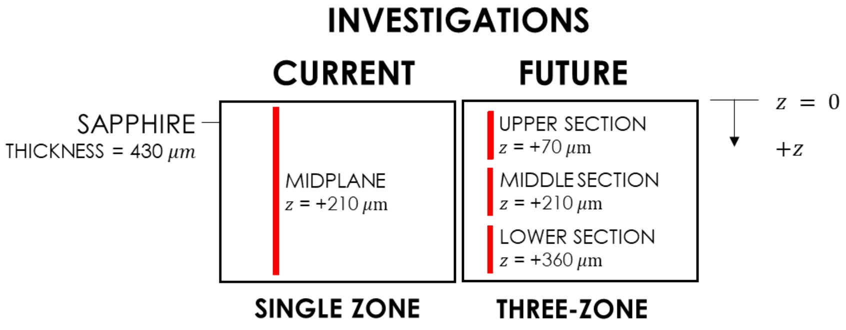

Figure 8.2 Schematic for three-zone scanning experiments comparison to single zone scanning experiments

4. Exploration of multiple foci irradiation of sapphire with femtosecond laser – Rapp et al. employed a Bessel beam for the irradiation and separation of sapphire [21]. Their results concluded that the transverse morphology of the top surface was vastly different when irradiated by a picosecond laser and a femtosecond laser. Irradiation by the picosecond laser resulted in the formation of three-fold cracks, while the irradiation by the femtosecond laser resulted in the fast separation of sapphire without tapering or chipping. As such, for the current multiple foci technique, it will be interesting to examine if the outcomes are significantly different between the picosecond laser employed in this investigation and a femtosecond laser.

9 References

[1] D. M. Allen and R. Redondo, "Fabrication methods for the manufacture of sapphire microparts," *Microsyst Technol,* vol. 18, no. 11, pp. 1835-1841, 2012.

[2] SJC Advanced Ceramics, "Physical properties of Aluminia, Zirconia and Sapphire," SJC Advanced Ceramics, n.d.. [Online]. Available: http://www.swiss-jewel.com/property.htm. [Accessed 22 November 2018].

[3] Kyocera, "Single Crystal Sapphire," 2018. [Online]. Available: https://global.kyocera.com/prdct/fc/product/pdf/s_c_sapphire.pdf. [Accessed 22 November 2018].

[4] S. Dub, P. Lytvyn, V. Strelchuk, A. Nikolenko, Y. Stubrov, I. Petrusha, T. Taniguchi and S. Ivakhenko, "Vickers Hardness of Diamond and cBN Single Crystals: AFM Approach," *Crystals,* vol. 7, no. 369, pp. 1-13, 2017.

[5] C. Rüttimann, "Sapphire cutting with pulsed fiber lasers," *Laser Technik Journal,* vol. 11, no. 3, pp. 48-50, 2014.

[6] W. A. Baylies and C. J. Moore, "The use of sapphire in mobile device and LED industries," November 2015. [Online]. Available: https://electroiq.com/2015/11/the-use-of-sapphire-in-mobile-device-and-led-industries/. [Accessed 3 October 2018].

[7] S. N. Dahal, J. A. LeBeau, S. Bowden and C. Honsberg, "Sub-Surface laser damage in Sapphire and Silicon: A path towards Laser Wafering," in *2016 IEEE 43rd Photovoltaic Specialists Conference*, Portland, 2016.

[8] G. Savriama, V. Jarry, L. Barreau, C. Boulmer-Leborgne and N. Semmar, "Laser micro-cutting of wide band gap materials," *AIP*, vol. 1464, no. 1, pp. 169-178, 2012.

[9] R. Mayerhofer, A. Hosseini and C. Rüttimann, "Laser cutting, drilling, and structuring of brittle materials," *Industrial Laser Solutions*, pp. 27-30, July 2015.

[10] A. Yadav, H. Kbashi, S. Kolpakov, N. Gordon, K. Zhou and E. U. Rafailov, "Stealth dicing of sapphire wafers with near infra-red femtosecond pulses," *Applied Physics A: Materials Science & Processing*, vol. 123, no. 5, pp. 1-7, 2017.

[11] P. Liu, L. Deng, J. Duan, B. Wu, X. Zeng, S. Ying and X. Wang, "A study on laser multi-focus separation technology of thick KDP crystal," *International Journal of Machine Tools & Manufacture*, Vols. 118-119, pp. 26-36, 2017.

[12] P. Liu, J. Duan, B. Wu, L. Deng, S. Ying, X. Zeng and X. Wang, "A flexible multi-focus laser separation technology for thick glass," *International Journal of Machine Tools and Manufacture*, vol. 135, pp. 12-23, 2018.

[13] S.-J. Chang, L. M. Chang, J. Y. Chen, C. S. Hsu, D. S. Kuo, C. F. Shen, W.-S. Chen and T. K. Ko, "GaN-Based Light-Emitting Diodes Prepared With Shifted Laser Stealth Dicing," *Journal of Display Technology*, vol. 12, no. 2, pp. 195-199, 2016.

[14] Y. Zhang, H. Xie, H. Zheng, T. Wei, H. Yang, J. Li, X. Yi, X. Song, G. Wang and J. Li, "Light extraction efficiency improvement by multiple laser stealth dicing in InGaN-based blue light-emitting diodes," *Optics Express,* vol. 20, no. 6, pp. 6808-6815, 2012.

[15] M. Yamada, Mitani, Narukawa, Yukio, S. Shioji, I. Niki, S. Sonobe, K. Deguchi, M. Sano and T. Mukai, "InGaN-Based Near-Ultraviolet and Blue-Light-Emitting Diodes with High External Quantum Efficiency Using a Patterned Sapphire Substrate and a Mesh Electrode," *Japanese Journal of Applied Physics,* vol. 41, pp. 1431-1433, 2002.

[16] D. S. Wuu, W. K. Wang, W. C. Shih, R. H. Horng, C. E. Lee, W. Y. Lin and J. S. Fang, "Enhanced output power of near-ultraviolet InGaN-GaN LEDs grown on patterned sapphire substrates," *IEEE Photonics Techonology Letters*, vol. 17, no. 2, pp. 288-290, 2005.

[17] G. Yang, J. Chang, J. Zhao, Y. Tong, F. Xie, J. Wang, Q. Zhang, H. Huang and D. Yan, "Investigation of light output performance for gallium nitride-based light-emitting diodes grown on different shapes of patterned sapphire substrate," *Materials Science in Semiconductor Processing,* vol. 33, pp. 149-153, 2015.

[18] J.-M. Lee, J.-H. Jang and T.-K. Yoo, "Scribing and cutting a blue LED wafer using a Q-switched Nd:YAG laser," *Applied Physics A: Materials Science & Processing,* vol. 70, no. 5, pp. 561-564, 2000.

[19] T.-C. Chen and R. B. Darling, "Parametric studies on pulsed near ultraviolet frequency tripled Nd:YAG laser micromachining of sapphire and silicon," *Journal of Materials Processing Technology,* vol. 169, pp. 214-218, 2005.

[20] A. Shamir and A. Ishaaya, "Large volume ablation of Sapphire with ultra-short laser pulses," *Applied Surface Science,* vol. 270, pp. 763-766, 2013.

[21] L. Rapp, R. Meyer, L. Furfaro, C. Billet, R. Giust and F. Courvoisier, "Crack formation and cleaving of sapphire with ultrafast Bessel beams," in *2017 Conference on Lasers and Electro-Optics Europe & European Quantum Electronics Conference*, Munich, 2017.

[22] L. Lytvynov, "Aluminum oxide," in *Single Crystals of Electronic Materials: Growth and Properties*, Cambridge, Woodhead Publishing, 2019, pp. 447-485.

[23] V. Kurlov, "Sapphire: Properties, Growth, and Applications," in *Reference Module in Materials Science and Materials Engineering*, Pergamon, Elsevier Ltd., 2001, pp. 8259-8264.

[24] E. R. Dobrovinskaya, L. A. Lytvynov and V. Pishchik, Sapphire: Material, Manufacturing, Applications, New York: Springer Science+Business Media, LLC, 2009.

[25] D. Kim, H. Kim, S. Lee and H. Jeong, "Effect of initial deflection of diamond wire on thickness variation of sapphire wafer in multi-wire saw," *International Journal of Precision Engineering and Manufacturing-Green Technology,* vol. 2, no. 2, pp. 117-121, 2015.

[26] A. Tamhankar and R. Patel, "Optimization of UV laser scribing process for light emitting diode sapphire wafers," *Journal of Laser Applications,* vol. 23, no. 3, 2011.

[27] J. Xu, H. Hu, C. Zhuang, G. Ma, J. Han and Y. Lei, "Controllable laser thermal cleavage of sapphire wafers," *Optics and Lasers in Engineering,* vol. 102, pp. 26-33, 2018.

[28] W.-J. Tsai, C.-J. Gu, C.-W. Cheng and J.-B. Horng, "Internal modification for cutting transparent glass using femtosecond Bessel beams," *Optical Engineering*, vol. 53, no. 3, 2014.

[29] A. K. Ghatak, Optics, New Delhi: McGraw Hill, 2010.

[30] D. W. Ball, Field Guide to Spectroscopy, Bellingham: SPIE - The International Society for Optical Engineering, 2006.

[31] W. M. Steen and J. Mazumder, Laser Material Processing: Fourth Edition, London: Springer, 2010.

[32] P. A. Karam and B. P. Stein, Light and Sound, New York: Infobase Publishing, 2010.

[33] J. D. Majumdar and I. Manna, "Laser processing of materials," *Sadhana,* vol. 28, no. 3-4, pp. 495-562, 2003.

[34] M. Gedvilas, J. Mikšys, J. Berzinš, V. Stankevič and G. Račiukaitis, "Multi-photon absorption enhancement by dual-wavelength double-pulse laser irradiation for efficient dicing of sapphire wafers," *Scientific Reports,* vol. 7, no. 5218, pp. 1-10, 2017.

[35] Latech Scientific Supply Pte. Ltd., "Sapphire (Al2O3) Wafer," Latech Scientific Supply Pte. Ltd., [Online]. Available: http://www.latech.com.sg/product/1425782275-Sapphire+%28Al2O3%29+Wafer.html. [Accessed 20 October 2018].

[36] HOLO/OR Ltd., "MultiFocal DOEs," HOLO/OR Ltd., 2018. [Online]. Available: https://www.holoor.co.il/product/multifocal/. [Accessed 17 October 2018].

[37] HOLO/OR Ltd., "Bifocal/Trifocal/Multifocal Application Notes," HOLO/OR Ltd., 2018. [Online]. Available: https://www.holoor.co.il/application/bifocal-trifocal-multifocal-application-notes/. [Accessed 17 October 2018].

[38] S. Sun and M. Brandt, "Laser Beam Machining," in *Nontraditional Machining Processes*, London, Springer, 2013, pp. 35-96.

[39] Z. K. Wang, H. Y. Zheng, W. J. Seow and X. C. Wang, "Investigation on material removal efficiency in debris-free laser ablation of brittle substrates," *Journal of Materials Processing Technology,* vol. 219, pp. 133-142, 2015.

[40] R. Geremia, D. Karnakis and D. P. Hand, "The role of laser pulse overlap in ultrafast thin film structuring applications," *Applied Physics A,* vol. 124, no. 9, pp. 1-8, 2018.

[41] R. Paschotta, Field Guide to Laser Pulse Generation, Bellingham: SPIE Press, 2008.

[42] E. Kannatey-Asibu, Principles of Laser Materials Processing, Hoboken: John Wiley & Sons, Inc., 2009.

[43] Y. Li, L. F. Feng, Q. Y. Xing and X. L. Wang, "Electrical Characteristics of GaN-Based Light-Emitting Diodes on Patterned Sapphire Substrates," *Journal of Electronic Materials,* vol. 44, no. 3, p. 999–1002, 2015.

[44] J. Fantl, *Private communication,* HOLO/OR Ltd., 2019.

[45] X. Lu, *Private communication*, Latech Scientific Supply Pte. Ltd., 2019.

Appendix I – Foci separation for multifocal lens and focusing optics

The actual foci separation for each MF lens and focusing optics combination [36] are tabulated in Table I.1 and Table I.2.

Table I.1 Actual foci separation for 9 foci MF lens with various focusing optics

MF lens	**9 foci**	
EFL of focusing optic (mm)	**12 (Focusing lens)**	**7.5 (Focusing lens)**
Foci separation of diffractive orders from +4 to –4	43.0	16.9
	43.2	16.9
	43.3	17.0
	43.5	17.0
	43.7	17.1
	43.9	17.1
	44.1	17.1
	44.2	17.2
Total foci separation	348.9	136.3
Average foci separation	43.6	17.0

Table I.2 Actual foci separation for 27 foci MF lens with various focusing optics

MF lens	**27 foci**			
EFL of focusing optic (mm)	**20 (OB10×)**	**10 (OB20×)**	**4.38 (OB40×)**	**7.5 (Focusing lens)**
Foci separation of diffractive orders from +13 to –13	101.3	26.3	5.2	14.9
	101.9	26.4	5.2	15.0
	102.5	26.4	5.2	15.0
	103.1	26.5	5.2	15.0
	103.7	26.6	5.2	15.1
	104.3	26.7	5.2	15.1
	105.0	26.8	5.2	15.1
	105.6	26.8	5.2	15.2
	106.3	26.9	5.2	15.2
	106.9	27.0	5.2	15.2
	107.6	27.1	5.2	15.3
	108.2	27.2	5.2	15.3
	108.9	27.3	5.2	15.3
	109.6	27.4	5.2	15.4
	110.3	27.4	5.2	15.4
	110.9	27.5	5.3	15.5
	111.6	27.6	5.3	15.5
	112.3	27.7	5.3	15.5
	113.0	27.8	5.3	15.6
	113.8	27.9	5.3	15.6
	114.5	28.0	5.3	15.6
	115.2	28.0	5.3	15.7
	115.9	28.1	5.3	15.7
	116.7	28.2	5.3	15.7
	117.4	28.3	5.3	15.8
	118.2	28.4	5.3	15.8
Total foci separation	2844.7	710.3	136.3	399.5
Average foci separation	109.4	27.3	5.2	15.4

Appendix II – Picosecond laser irradiation of sapphire

Tables II.1, II.2 and II.3 contain optical images from the picosecond laser irradiation experiments for the samples with various surface morphologies in Section 5.4 at 5× magnification. Tables II.4, II.5 and II.6 contain optical images from the picosecond laser irradiation experiments in Section 5.4 at 10× magnification.

Table II.1 Optical images at 5× magnification of sapphire samples after laser irradiation at different power output for Sample A (double side polished)

	Power		
	0.5 W 25% power level	**1.1 W** 50% power level	**1.7 W** 75% power level
Top (polished)		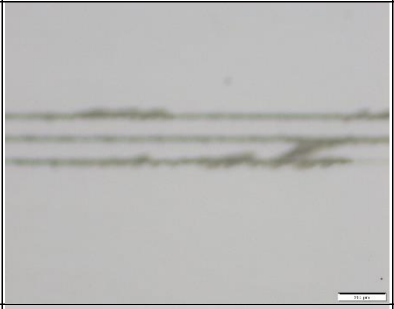	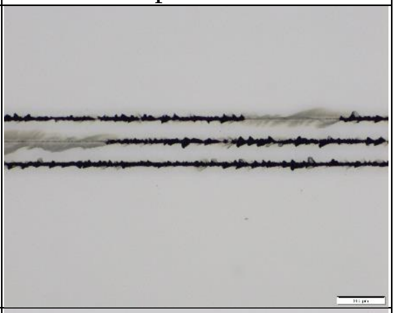
Bottom (polished)		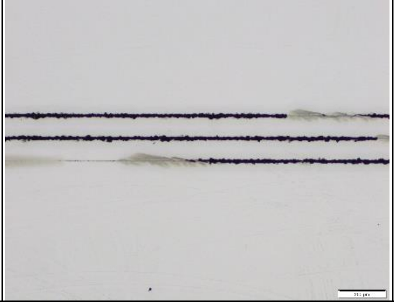	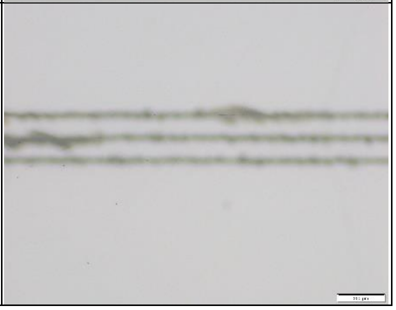

Table II.2 Optical images at 5× magnification of sapphire samples after laser irradiation at different power output for Sample B (single side polished – light incident on unpolished surface)

	Power		
	0.5 W 25% power level	**1.1 W** 50% power level	**1.7 W** 75% power level
Top (unpolished)	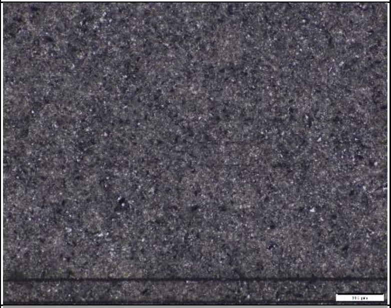	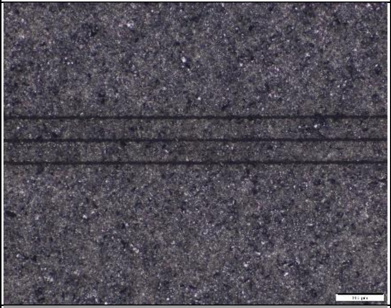	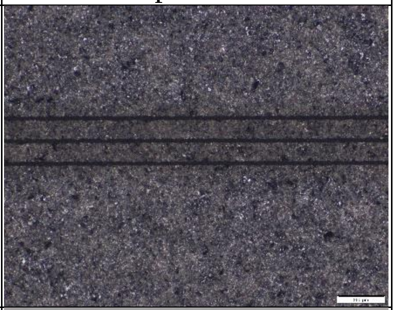
Bottom (polished)	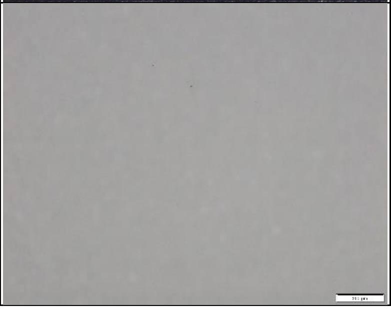		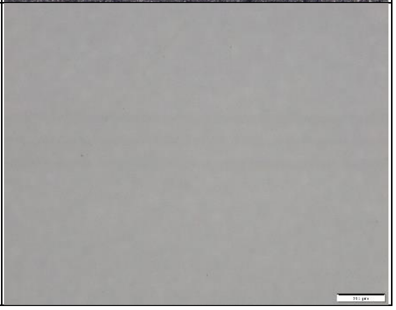

Table II.3 Optical images at 5× magnification of sapphire samples after laser irradiation at different power output for Sample C (single side polished – light incident on polished surface)

	Power		
	0.5 W 25% power level	**1.1 W** 50% power level	**1.7 W** 75% power level
Top (polished)	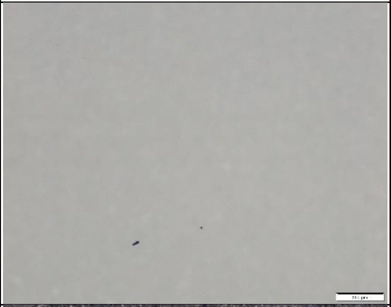		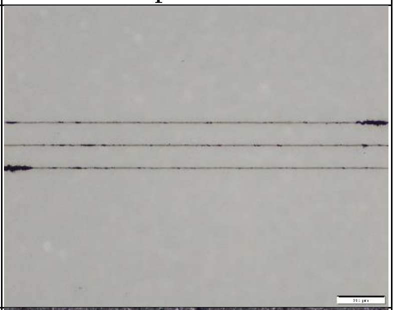
Bottom (unpolished)	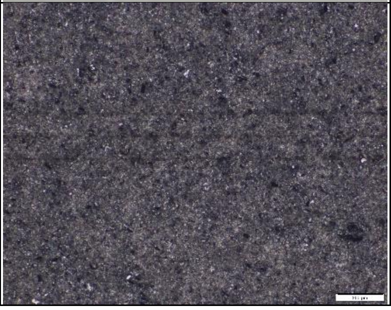	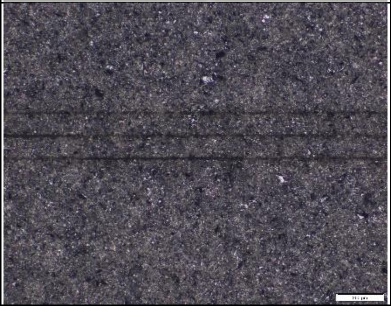	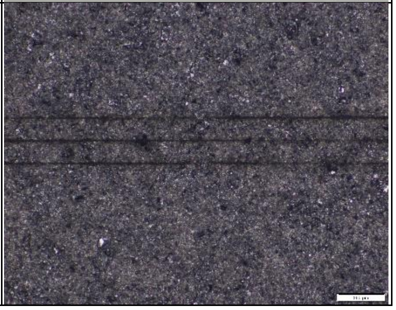

Table II.4 Optical images at 10× magnification of sapphire samples after laser irradiation at different power output for Sample A (double side polished)

	Power		
	0.5 W 25% power level	**1.1 W** 50% power level	**1.7 W** 75% power level
Top (polished)			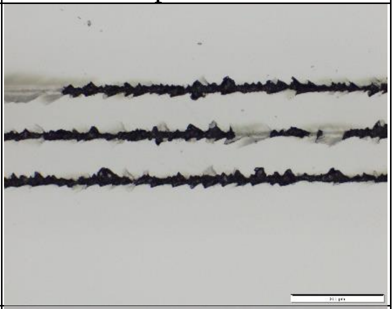
Bottom (polished)	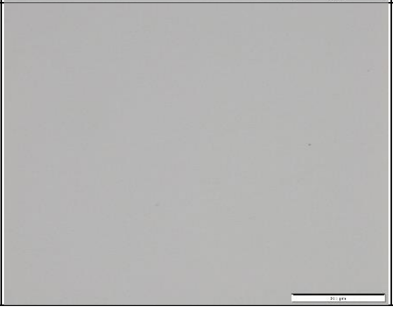	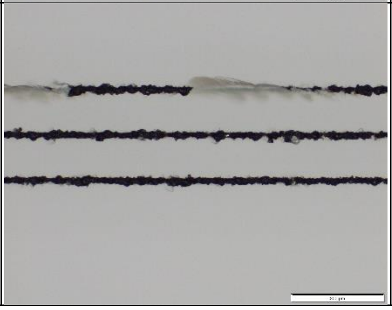	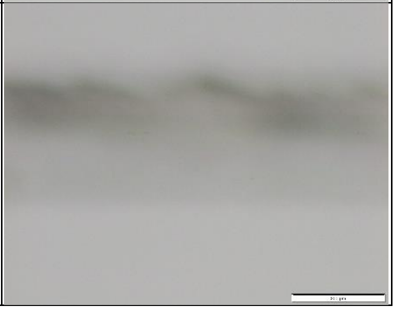

Table II.5 Optical images at 10× magnification of sapphire samples after laser irradiation at different power output for Sample B (single side polished – light incident on unpolished surface)

	Power		
	0.5 W 25% power level	**1.1 W** 50% power level	**1.7 W** 75% power level
Top (unpolished) *Row 1*	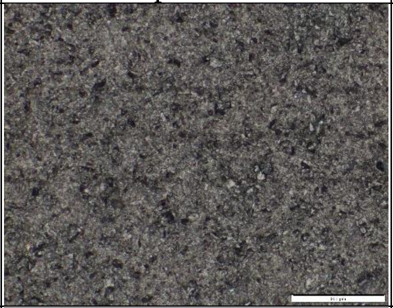	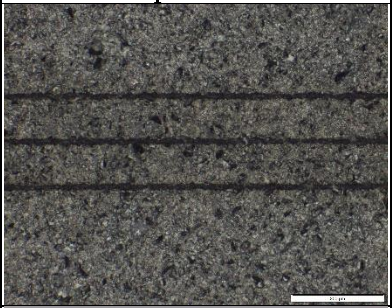	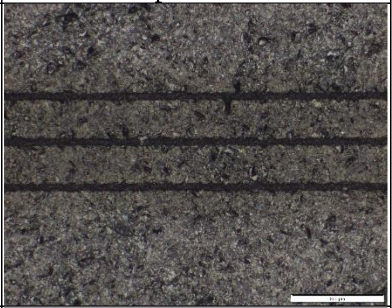
Bottom (polished) *Row 2*			

Table II.6 Optical images at 10× magnification of sapphire samples after laser irradiation at different power output for Sample C (single side polished – light incident on polished surface)

	Power		
	0.5 W 25% power level	**1.1 W** 50% power level	**1.7 W** 75% power level
Top (polished)			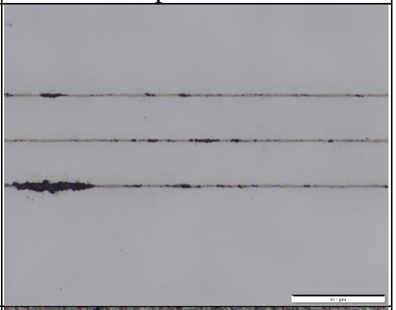
Bottom (unpolished)